Detailed chemical composition analysis of the Soi crater region on Titan

A. Solomonidou, M.J. Malaska, R.M.C. Lopes, A. Coustenis, A.M. Schoenfeld, B. Schmitt, S.P.D. Birch, Alice Le Gall, K. Lawrence, C. Matsoukas, et al.

Icarus

Detailed chemical composition analysis of the Soi crater region on Titan.

--Manuscript Draft--

Manuscript Number:	ICARUS-D-23-00021R5
Article Type:	Research paper
Keywords:	Titan; Surface composition; Radiative transfer; Ocean Worlds; icy satellites
Corresponding Author:	Anezina Solomonidou, Ph.D. Hellenic Space Center Athens, GREECE
First Author:	Anezina Solomonidou, Ph.D.
Order of Authors:	Anezina Solomonidou, Ph.D.
	Michael Malaska
	Rosaly Lopes
	Athena Coustenis
	Ashley Schoenfeld
	Bernard Schmitt
	Samual Birch
	Alice Le Gall
	Kenneth Lawrence
	Christos Matsoukas
	Stephen Wall
	Charles Elachi
Abstract:	The Soi crater region (0º to 60ºN, 180ºW to -110ºW), which includes the well-preserved Soi crater in its center, spans a region from Titan's aeolian-dominated equatorial regions to fluvially-dominated high northern latitudes. This provides a rich diversity of landscapes, one that is also representative of the diversity encountered across Titan. Schoenfeld et al. (2023) mapped this region at 1:800,000 scale and produced a geomorphological map showing that the area consists of 22 types of geomorphological units. The Visual and Infrared Mapping Spectrometer (VIMS) coverage of the region enabled the detailed analysis of spectra of 261 different locations using a radiative transfer technique and a mixing model, yielding compositional constraints on Titan's optical surface layer. Additional constraints on composition on the near-surface substrate were obtained from microwave emissivity. We have derived combinations of top surface materials between dark materials, tholins, water-ice, and methane suggesting that dark mobile organic material at equatorial and high latitudes indicates "young" terrains and compositions, while tholin/water-ice mixtures that dominate areas around latitude 35ºN show a material that is older plains deposits that we interpret to be the end stage of aeolian and fluvial transport and deposition. We found no spectral evidence of CO2, HC3N, and NH3 ice. We use the stratigraphic relations between the various mapping units and the relation between the geomorphology and the composition of the surface layers to build hypotheses on the origin and evolution of the regional geology. We suggest that sedimentary deposits, likely aeolian, are dominant in the region with fluvial activity and leaching changing the nature of the top surfaces of the midlatitude areas of the Soi crater region.
Suggested Reviewers:	Jani Radebaugh jani.radebaugh@byu.edu
	Conor Nixon conor.a.nixon@nasa.gov
	Stéphane Le Mouélic

	stephane.lemouelic@univ-nantes.fr
	Thomas Cornet Thomas.Cornet@ext.esa.int
	Katrin Stephan katrin.stephan@dlr.de
Opposed Reviewers:	
Response to Reviewers:	

Manuscript Number: ICARUS-D-23-00021R4
Detailed chemical composition analysis of the Soi crater region on Titan.
Icarus

Responses to the Editor and the reviewers

Dear Dr Solomonidou,

Thank you for submitting your manuscript to Icarus. I have received comments from a reviewer on your revised manuscript. The reviewer makes two final recommendations for minor updates to the manuscript, and I agree with these. I invite you to resubmit your manuscript after addressing the comments below. Please resubmit your revised manuscript by ***Jul 21, 2024****.*

Kind regards,

Amanda Hendrix
Editor
Icarus

Response: Dear Dr Hendrix,

We have carefully considered the reviewer's two comments and have made the necessary revisions to comply with the recommendations. We believe that the revisions satisfactorily address all the reviewers' concerns.

Once again, we appreciate the constructive feedback from the reviewers and the editorial team. Thank you for your time and consideration.

Sincerely,
Anezina Solomonidou

Reviewer #4:

I have read the version 4 of this paper. The authors have taken my comments on version 3 into account. Most of my concerns have been addressed. However, I still disagree on two points:

1- the quality of the fits - I still think that it is problematic. It may be the VIMS calibration, the RT model, the lack of a component in the spectral library, ... Anyway, I think that this observation (misfit at low wavelength) should be discussed. The conclusion is that further work is needed to understand the misfit. There is nothing else that the present study can do about it.

Response: Yes, we agree with you and we had already placed cautionary comments in our article. Following your suggestion we have now added the following text: (page 15) 'The mismatch, especially at the shorter wavelengths, is indicative of the limitations set by the VIMS data, the modeling, and the variability of the material library compared to the expected complexity of Titan's surface.' and 'Further work on the Cassini data, along with the advanced development of tools for their processing and additional data from future missions (e.g., Dragonfly) and observations (e.g., JWST), will help us better understand the reasons behind these mismatches and provide solutions for improved fits between the albedos and the simulated surface mixtures.'

2- H2O. As mentioned in previous reviews, the emissivity data are not consistent with the interpretation of the VIMS data. The comparison between figures 7 and 8 illustrates the difference. In Figure 8 (emissivity), low emissivity (water ice) is found in the southeast corner. In Figure 7 (spectral mixing from VIMS data), H2O is found at the northeast (20-60 N; 110 W)

of the domain and not in the southeast corner (0-10 N, 120 -110 W). This is disturbing. I think that the paper does not address this simple observation very well.

Response: You are right, we have added text to address this observation. (page 20): 'However, a notable difference between the emissivity and VIMS albedo results is the inconsistency in the major constituent of the mixtures at the southeast 'corner' of the Soi crater region of interest. Here, the emissivity data indicate a major water ice constituent (Fig. 8), while VIMS data suggest an organic one, specifically tholin-like material (Figs. 7a and 7b).'

Otherwise, the paper reads well.

Response: We would like to thank the reviewer for the time and effort in reviewing our work. We have carefully addressed both comments

Highlights:

- Titan’s compositional evolution cycle includes aeolian transport and leaching.
- Areas around latitude 35ºN are dominated by tholin and ice-like spectral signatures
- The midlatitudes are composed of end-stage materials that were subjected to rainfall.
- Empty lakes at the midlatitudes have same composition as the northern empty lakes.

Declaration of interests

☒ The authors declare that they have no known competing financial interests or personal relationships that could have appeared to influence the work reported in this paper.

☐The authors declare the following financial interests/personal relationships which may be considered as potential competing interests:

Detailed chemical composition analysis of the Soi crater region on Titan

A. Solomonidou[1,2], M. J. Malaska[3], R. M. C. Lopes[3], A. Coustenis[2], A. M. Schoenfeld[4], B. Schmitt[5], S. P. D. Birch[6], A. Le Gall[7, 8], K. Lawrence[3], C. Matsoukas[9], S. D. Wall[10], C. Elachi[10]

[1]Hellenic Space Center, Athens, Greece.

[2]LESIA–Observatoire de Paris, CNRS, UPMC Univ. Paris 06, Univ. Paris-Diderot, Meudon, France.

[3]Jet Propulsion Laboratory, California Institute of Technology, Pasadena, CA, USA.

[4]Department of Earth, Planetary, and Space Sciences, University of California Los Angeles, Los Angeles, CA, USA.

[5]Institut de Planétologie et d'Astrophysique de Grenoble, Université Grenoble Alpes, CNRS, Grenoble, France.

[6]Department of Earth, Atmospheric, and Planetary Science, Massachusetts Institute of Technology, Cambridge, MA, USA.

[7]Institut LATMOS/IPSL, UVSQ Université Paris-Saclay, Sorbonne Université, CNRS, France.

[8]Institut Universitaire de France, Paris, France.

[9]KTH-Royal Institute of Technology, Stockholm, Sweden.

[10]California Institute of Technology, Pasadena, CA, USA.

Corresponding author: Anezina Solomonidou (anezina.solomonidou@hsc.gov.gr), 178 Kifissias Avenue, Athens 15231, Greece

Highlights:

- Titan's compositional evolution cycle includes aeolian transport and leaching.
- Areas around latitude 35ºN are dominated by tholin and ice-like spectral signatures
- The midlatitudes are composed of end-stage materials that were subjected to rainfall.
- Empty lakes at the midlatitudes have same composition as the northern empty lakes.

Abstract

The Soi crater region (0º to 60ºN, 180ºW to -110ºW), which includes the well-preserved Soi crater in its center, spans a region from Titan's aeolian-dominated equatorial regions to fluvially-dominated high northern latitudes. This provides a rich diversity of landscapes, one that is also representative of the diversity encountered across Titan. Schoenfeld et al. (2023) mapped this region at 1:800,000 scale and produced a geomorphological map showing that the area consists of 22 types of geomorphological units. The Visual and Infrared Mapping Spectrometer (VIMS) coverage of the region enabled the detailed analysis of spectra of 261 different locations using a radiative transfer technique and a mixing model, yielding compositional constraints on Titan's optical surface layer. Additional constraints on composition on the near-surface substrate were obtained from microwave emissivity. We have derived combinations of top surface materials between dark materials, tholins, water-ice, and methane suggesting that dark mobile organic material at equatorial and high latitudes indicates "young" terrains and compositions, while tholin/water-ice mixtures that dominate areas around latitude 35ºN show a material that is older plains deposits that we interpret to be the end stage of aeolian and fluvial transport and deposition. We found no spectral evidence of CO_2, HC_3N, and NH_3 ice. We use the stratigraphic relations between the various mapping units and the relation between the geomorphology and the composition of the surface layers to build hypotheses on the origin and evolution of the regional geology. We suggest that sedimentary deposits, likely aeolian, are dominant in the region with fluvial activity and leaching changing the nature of the top surfaces of the midlatitude areas of the Soi crater region.

1 Introduction

The surface of Saturn's moon Titan has been revealed by the Cassini-Huygens spacecraft to be geologically complex with both exogenic and putative endogenic processes modifying its appearance. Titan's dense atmosphere and active methane cycle has enabled aeolian, fluvial, pluvial, and lacustrial processes, causing erosion and deposition. Few impact craters are seen, attesting that the surface is geologically young (e.g., Wood et al., 2010; Hedgepeth et al., 2020). Tectonism and possibly cryovolcanism have also contributed to surface modification (Jaumann et al., 2009; Mitri et al., 2008, 2010; Radebaugh et al., 2007; Lopes et al., 2013; 2019; Wall et al., 2009; Nelson et al., 2009; Solomonidou et al., 2013; 2016; Sohl et al., 2014; Wood and Radebaugh, 2020). The rich variety of geologic features on Titan and how the processes have dominated different latitudes have been discussed in previous works. For example, lakes and seas are present at high latitudes (e.g., Stofan et al., 2007; Bratsolis et al., 2012; Birch et al., 2016), while dunes of organic materials are concentrated at low latitudes (Lorenz et al., 2006; Radebaugh et al., 2008; Lopes et al., 2010; Rodriguez et al., 2014). Fluvial channel networks are present across large areas of the surface (Jaumann et al., 2008; Malaska et al., 2011; Langhans et al., 2012; Burr et al., 2013; Radebaugh et al., 2016; Miller et al., 2021), with a rich diversity in morphology (Burr et al., 2013; Miller et al., 2021), and are both liquid-filled (Poggiali et al., 2016) and dry. The mountainous and hummocky units represent remnants of an older crust, making them the oldest exposed unit on Titan, and they mostly appear in the equatorial zones and small areas all over the globe (Williams et al., 2011; Lopes et al., 2020a; Malaska et al., 2016a; 2020; Schoenfeld et al., 2021). Organic materials, produced by high-altitude photochemistry of methane and nitrogen in Titan's atmosphere, cover much of Titan's surface (Wilson and Atreya, 2004; Lavvas et al., 2008; Krasnopolsky, 2009; Clark et al., 2010; Solomonidou et al., 2018; 2020a). The buildup of these organic materials is evidenced by large standing dissected plateaux elevated by hundreds of meters

(Malaska et al., 2020). The midlatitudes of Titan are dominated by undifferentiated plains (Lopes et al., 2016; 2019; 2020) which are interpreted as being sedimentary in nature and likely formed by aeolian processes (Malaska et al., 2016b). Titan's latitudinal dependence for composition of the upper surface layer (Solomonidou et al., 2018), as well as patterns of wind deposition (Malaska et al., 2016b), show that, for both hemispheres, winds may transport material from both equatorial regions and high latitudes towards a zone at ~35º. That zone, at the midlatitudes may represent a 'sink', where materials are deposited as undifferentiated plains (Lopes et al., 2016; Malaska et al., 2016b; Solomonidou et al., 2020a).

The Soi crater region is scientifically valuable as it straddles the equatorial, midlatitude, and northern regions of Titan. The present study on the composition complements the geomorphological study of Schoenfeld et al. (2023). Our compositional map for this region is created using a radiative transfer code with Visual and Infrared Mapping Spectrometer (VIMS) data that help estimate the haze contribution to the data and extract surface information that are later matched to surface component mixture simulations (Hirtzig et al., 2013; Bonnefoy et al., 2016; Solomonidou et al., 2014; 2018; 2020a;b). The goal of this paper is to bring constraints on the formation and evolution of the selected area through the combination of the geomorphological and compositional maps of the Soi crater region. The maps will help reveal the types and extent of the geomorphologic units and the differences in nature of the top layers of the surface, and to infer the geological processes responsible for their formation and evolution. Our compositional mapping follows the methods described in Solomonidou et al. (2014; 2018; 2020a;b). Our efforts here are part of a global compositional mapping project that is currently in progress (Solomonidou et al., 2022), attempting to improve our knowledge of Titan's complex systems.

2 Geologic Setting

The Soi crater region was defined in Schoenfeld et al. (2023) as the area spanning from longitude 180º W to 110º W and from latitude 0 to 60ºN and the area contained in this region amounts to ~8×10^6 km^2 (~9.7% of Titan's surface). This region is geomorphologically mapped in detail and presented in the same article. For the production of the map by Schoenfeld et al. (2023) ~5.6% of the total surface area was mapped by using high resolution Synthetic Aperture Radar (SAR) data and the rest of the area was covered by non-SAR data (microwave emissivity, Imaging Science Subsystem -ISS, and VIMS), and mapped at lower resolution. For VIMS and the compositional mapping efforts, the area that was covered with data compatible and adequate to our radiative transfer modeling (detailed in section 3) spanned approximately 5.4×10^6 km^2, which corresponds to ~6.5% of Titan's total surface. The Soi crater region contains 22 distinct geomorphological units many of which were found in the Afekan (Malaska et al., 2016a) and South Belet regions (Schoenfeld et al., 2021).

The geomorphological map presented in Schoenfeld et al. (2023) used SAR and non-SAR datasets including altimetry, Radiometry-Emissivity, ISS, and VIMS (Fig. 1). All the different Cassini data used to create the geomorphological map of the Soi crater region (SAR, HiSAR, SARTopo and Digital Terrain Model, emissivity, VIMS, and ISS data) can be seen in Figure 2 of Schenfeld et al. (2023). The 22 geomorphological units identified include features of empty lakes, mountains, dunes, craters, labyrinth, and vast plains (Table 1). The Soi crater region is dominated by plains, matching the general trend around Titan's globe (see Lopes et al., 2020), followed by dunes, mountainous terrains, and finally very few craters and empty sharp-edged depressions

(SEDs) (Table 1). As for most of Titan, impacts have been erased by more recent geological processes, likely those that form dunes and plains.

Table 1. Terrain class, terrain units, terrain unit code found in the Soi crater region. Details, locations, and descriptions of the units are in Table 1 of Schoenfeld et al. (2023). The letter codes followed here are based on mapping efforts that have followed the general principles of previous Titan mapping and other planetary mapping efforts (Greeley and Batson, 1990; Greeley et al., 2000; Patterson et al., 2010; Williams et al., 2014; Lopes et al., 2016; 2020; Malaska et al., 2016; 2020; Schoenfeld et al., 2021; 2023).

Terrain class/ % of total area	**Terrain unit name and code**
Plains (73%)	Undifferentiated plains (*pul*)
	Variable plains (*pfv*)
	Scalloped plains (*psv*)
	Dark irregular plains (*pil*)
	Streak-like plains (*psh*)
	Bright gradational plains (*pgh*)
	Undivided plains (*pu*)
	Undivided dark plains (*pdu*)
Dunes (14%)	Featureless sand sheets (*ds*)
	Linear dunes (*dl*)
	Undivided dunes (*du*)
Mountains / Hummocky / Labyrinth (12%)	Mountain (*hm*)
	Hummocky (*hh*)
	Degraded hummocky (*hdm*)
	Pitted hummocky (*hph*)
	Finely dissected labyrinth (*lbf*)
	Undivided mountain chains/hummocky areas (*hu*)
Craters (<1%)	Crater rim (*crh*)
	Crater ejecta (*ceh*)
	Crater fill 3 (*cf3*)
Lakes (<1%)	Sharp-edged depression (*bse*)
	Ramparts (*brh*)

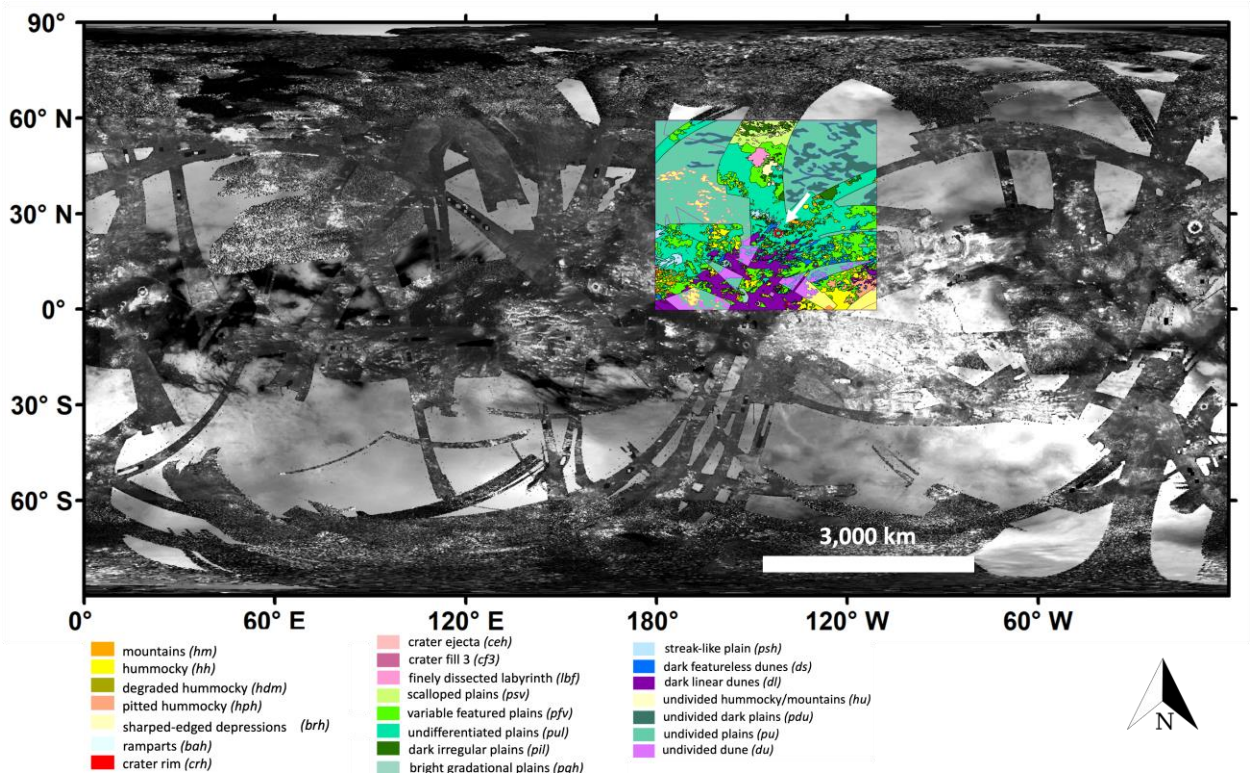

Figure 1. Geomorphological map of the Soi crater region (adapted from Schoenfeld et al., 2023) in global context. Geomorphological map for all SAR and non-SAR data at zero transparency (map layer fully opaque), same color scheme as the global geomorphological map of Titan in Lopes et al. (2020). The arrow points to the Soi crater. The background map is a global mosaic of Titan created from Imaging Science Subsystem (ISS) data (USGS Astrogeology Science Center).

3 Compositional mapping

Titan's surface composition remains, to this day, largely a mystery. Due to both atmospheric effects and spectral degeneracies, we have so far been prevented from making quantitative and accurate estimates of material concentrations within the numerous and varied geologic units on Titan's surface. This is a complex situation that can only be improved in a step-by-step approach in which every new constraint brings useful additional information, while waiting for new observations from ground-based facilities or *in situ* data from space missions like Dragonfly (e.g., Tobie et al., 2014; Lorenz et al., 2021; Barnes et al., 2021; Sulaiman et al., 2021; Rodriguez et al., 2022). There are, however, select windows through Titan's atmosphere in the near-infrared where the methane absorption is reduced (e.g., Barnes et al., 2005; Corlies et al., 2021). Due to Titan's complex atmosphere and processes therein, we apply a radiative transfer code to Cassini VIMS data in order to tackle as well as possible the issue of lingering methane absorption and scattering of atmospheric components.

For the chemical compositional mapping, we used methods that have been successfully used in the past on VIMS data (Bonnefoy et al., 2016; Lopes et al., 2016; Malaska et al., 2016a; Brossier et al., 2018; Solomonidou et al., 2014; 2016; 2018; 2020a;b), to account for the atmospheric contribution to the data and extract the actual surface information in the form of

albedo values and spectral responses. Further, similar to Solomonidou et al. (2018), where the first attempt of constraining the chemical composition of all major Titan geomorphological units was made, in addition to the compositional analysis of one specific unit, the impact craters (Solomonidou et al., 2020a), here we provide a compositional analysis of the entire Soi crater region in greater detail than in the previous efforts and for a significantly larger number of units and locations. Efforts to spectrally analyze Titan's vast areas and constrain their composition can be found in Nelson et al. (2006), McCord et al. (2006; 2008), Barnes et al. (2008), Brown et al. (2008), Clark et al. (2010), Soderblom et al. (2010), MacKenzie et al. (2014), Rodriguez et al. (2014), Brossier et al. (2018), Griffith et al. (2019), Coutelier et al. (2021) and others. All of these studies have analyzed VIMS data. Some of them have utilized radiative transfer codes (e.g., Coutelier et al., 2021) for their data analyses, while others have employed geophysical and remote sensing tools and methods such as Principal Component Analysis (PCA) (e.g., Griffith et al., 2019) and spectral ratios (e.g., Barnes et al., 2008). These methods are often employed to highlight differences between features and to reduce the effect of varying light reflectance intensities. In Coutelier et al. (2021), the radiative transfer code is utilized to factor in atmosphere scattering and absorption, thereby eliminating atmospheric effects and discrepancies caused by observational geometries. The ultimate outcome is the retrieval of atmospheric albedos across all atmospheric windows. Their findings underscore a significant observation, which is compatible to findings of this present work: the relationship between water ice and VIMS 'dark blue' and 'bright blue' areas is not as straightforward as previously believed (Barnes et al., 2007a, 2007b).

Our chemical composition map was created using the measurements of VIMS through our radiative transfer code (RT) and spectral deconvolution analysis. We recognize that the spectral analysis is only of the very thin optical layer (tens of microns) that covers the surface of Titan. To take into account the material below the optical covering, in our interpretations of the geological history of the area we also use the microwave emissivity measurements that probe the surface to greater depths (tens of centimeters). Microwave emissivity can be used to constrain the composition in depths that IR is unable to reach. Indeed, the radiometry provides a measure of the averaged emissivity of the near subsurface down to a depth that can be approximately defined as the electrical skin depth (Janseen et al., 2016). The sounding depth has been estimated based on the seasonal thermal signature in Janssen et al. (2009; 2016) and it is of the order of 40 cm - 1 m in the radar dark terrains, and to 200 m in liquid methane. This largely depends on the microwave transparency of the material, while the presence of high dielectric constant materials and/or volume scattering due to the presence of structures in the subsurface, are considered factors that decrease the emissivity values (Janssen et al., 2016).

3.1 Radiative Transfer Technique and Mixing Model

The compositional results are extracted through a series of analyses of VIMS data. We have analyzed 261 different locations from within the Soi crater region using 14 VIMS datacubes from 8 different Cassini flybys (Table 2; Figure 2). The selection of our 261 regions of interest (RoIs) was made after carefully examining the available VIMS datacubes compatible to our RT approximation and was based on the identification of pixels that thoroughly include different geomorphological units as described in Schoenfeld et al. (2013) in good resolution. We then used our RT code to extract surface albedos from the VIMS data (Hirtzig et al., 2013; Solomonidou et al., 2014;2016; 2018; 2020a;b).

Table 2. Selected Cassini/VIMS datacube observations including flybys, dates of acquisition, product IDs, and cube properties (angles of incidence *i*, emergence *e*, and phase α; spatial resolution res).

Flyby	Date	Selected pixels with numbers as shown in Fig. 2 and product IDs	Datacube Properties Geometry-Spatial Resolution (*i*,*e*,*α*,res/pxl)
Tb	12/2004	79-80: 1481629409	*i:* 52-53º, *e:* 15-17º, *α:* 36-37º, res: 03 km
T08	10/2005	A7-A31, A33, 98: 1509148649 50-58, 107-110: 1509149009 59-62, 72-75, 89-93: 1559085140	*i:* 30-57º, *e:* 09-46º, *α:* 23-24º, res: 46 km *i:* 34-60º, *e:* 26-42º, *α:* 22-23º, res: 45 km *i:* 49-60º, *e:* 26-42º, *α:* 25-26º, res: 39 km
T10	01/2006	1-6: 1516007480	*i:* 36-49º, *e:* 01-12º, *α:* 37-38º, res: 14 km
T12	03/2006	15-22: 1521407900 23-29, 111-112: 1521405451 A1-A6, A32, A34-A55: 1521402363	*i:* 29-37º, *e:* 34-55º, *α:* 65-66º, res: 15 km *i*: 45-57º, *e:* 19-38º, *α:* 64-65º, res: 38 km *i:* 54-59º, *e:* 11-41º, *α:* 63-64º, res: 23 km
T31	05/2007	63-66, 76, 99-106: 1559081653	*i:* 48-59º, *e:* 37-51º, *α:* 26-27º, res: 29 km
T77	06/2011	7-12, 14, 77-78b: 1687307753	*i*: 10-38º, *e*: 27-58º, *α:* 21-22º, res: 25 km
T97	01/2014	30-36, 96-97, 113-116: 1767303982 33b, 37-42: 1767303262 43-49, 81-88, 94-95: 1767301842	*i:* 33-49º, *e:* 10-28º, *α:* 51-54º, res: 10 km *i:* 43-60º, *e*: 08-30º, *α:* 52-53º, res: 12 km *i:* 32-44º, *e:* 11-22º, *α:* 55-56º, res: 16 km
T113	09/2015	13, 67-71: 1822165321	*i:* 37-59º, e: 02-09º, *α:* 57-58º, res: 14 km

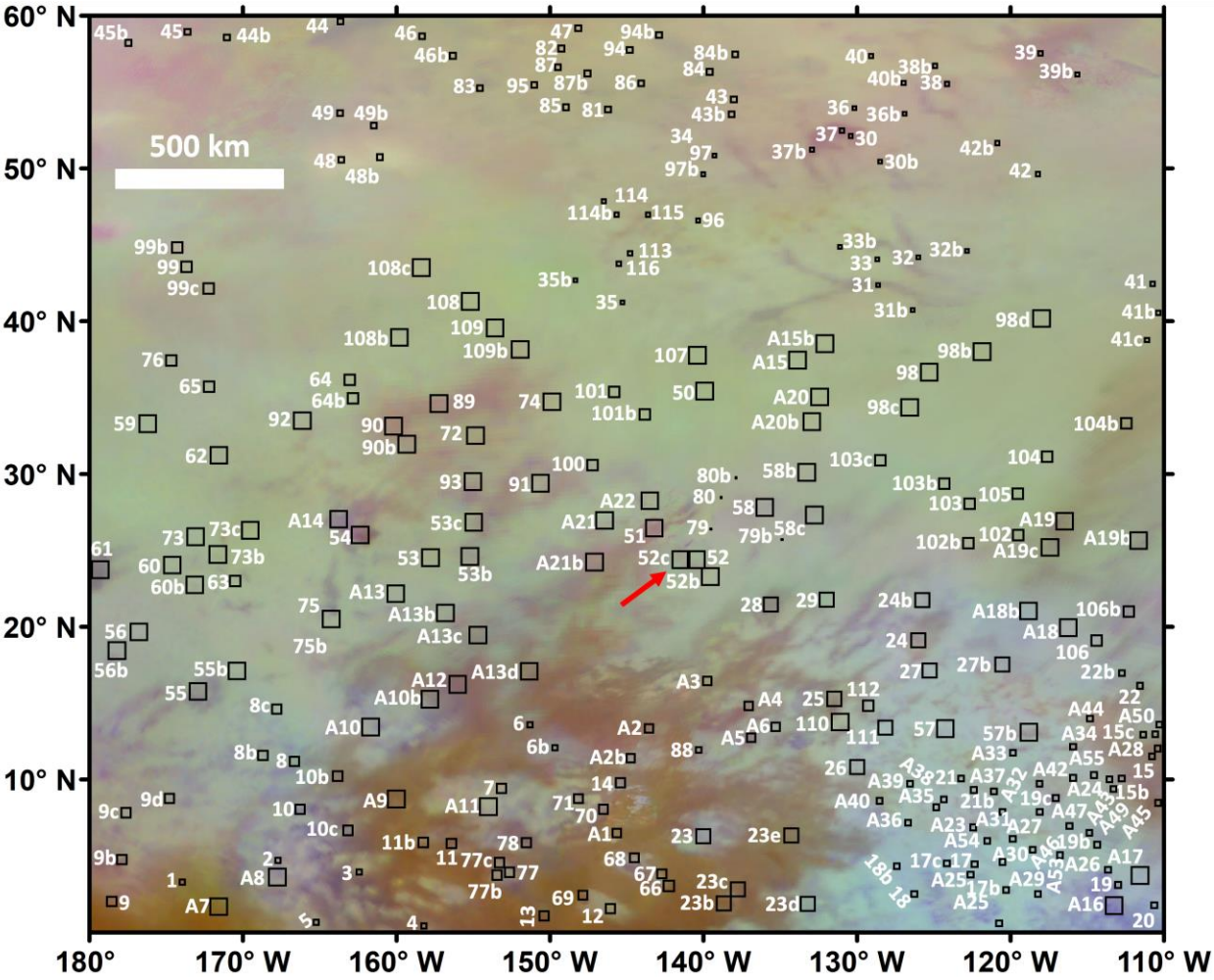

Figure 2. Regions of interest within the Soi crater region and pixel selections on VIMS for RT analysis from 261 different locations. The black squares correspond to the region of interest (RoI)

selected at each location based on their spatial resolution (see Table 2). The red arrow indicates the location of the Soi crater. North is at the top.

Our RT code (Hirtzig et al., 2013) is a plane-parallel code based on a Spherical Harmonic Discrete Ordinate Method solver (SHDOMPP) (Evans, 2007) that incorporates: (a) the vertical profiles of temperature and pressure provided by the Huygens Atmospheric Structure Instrument (HASI) (Fulchignoni et al., 2005); (b) the methane vertical mixing ratio from the Gas Chromatograph Mass Spectrometer (GCMS) (Niemann et al., 2010); (c) a uniform CO mole fraction equal to 4.5 x 10^{-5} based on Cassini/CIRS measurements (de Kok et al., 2007); (d) atmospheric opacity sources from aerosols and gases: Rayleigh scattering from N_2 and CH_4 (Peck and Khanna, 1966; Weber, 2003); collision-induced absorption by nitrogen (N_2) and hydrogen (H_2) (McKellar et al. (1989); Lafferty et al. (1996); lines for methane (Campargue et al., 2015; TheoReTS - Rey et al., 2018) and its isotopologues (e.g., $^{12}CH_4$, $^{13}CH_4$, $^{12}CH_3D$) (HITRAN2020 - Rothman et al., 2013; Gordon et al., 2022); lines for CO and C_2H_2 isotopologues (GEISA2009 - Jacquinet-Husson et al., 2011) with the use of correlated-*k* absorption coefficients as described in Hirtzig et al. (2013). Considering all components (a-d), the code analyses the VIMS data and produces simulations of the surface albedo with various haze opacities.

The results are then calibrated with respect to the albedo measurements derived by the Descent Imager Spectral Radiometer (DISR) at the Huygens landing site (HLS), which we use as a reference area and a calibration tool. Given that the haze extinction profile reference is adjusted to the measurements from DISR, the haze contribution to the VIMS data at the landing site of Huygens is defined as 100%. By iteration for the best possible fit, the code derives the haze contributions with an absolute accuracy of ±5% (Hirtzig et al., 2013). After estimating the haze population at all window wavelengths, the surface albedos are extracted at full spectral resolution and in weighted averages over each window's wavelength range (Tomasko et al., 2008; Hirtzig et al., 2013). In a weighted average, each data point value from within each of the 8 atmospheric windows is multiplied by an assigned weight, which is then summed and divided by the number of data points. For this reason, a weighted average can improve the data's accuracy. In this current analysis, we calculated single points of weighted averages of the surface albedo within the windows, with larger weights for channels with higher transmittance around the center. The spectral resolution (Full Width at Half Maximum, FWHM) is about 13 nm below 2.0 μm, increases up to 22 nm at 4.2 μm, and decreases to 18 nm at 4.8 μm (Brown et al., 2004). An example of weighted averages of the surface albedos in the atmospheric windows compared to the full resolution surface albedo spectrum in the 0.89–5.2 μm of the Visual and Infrared Mapping Spectrometer range can be found in Figure 5 of Solomonidou et al. (2018).

In our RT code and the extraction of surface albedos, we consider several uncertainties calculated and summed at the 3σ level including random errors due to noise in the data and due to propagation of haze retrieval errors, as well as systematic errors due to model, resulting from uncertainties due to the CH_4 far-wings opacity, the CH_4 linelist, the CH_4 vertical concentration profile, the aerosol phase function, the aerosol vertical distribution, and the aerosol forced single scattering albedo. All the details on the error estimation can be found in Section 3.3. in Hirtzig et al. (2013). In this current analysis we also take into account errors in the existing spectral line profiles, the haze extinction fit, the data intrinsic noise, which unlike random noise, is not random but arises from specific characteristics or imperfections in the sensor (McCord et al., 2004) and the phase function uncertainty. The surface albedos are then inverted with relative errors of 35%, 35%, 26%, 21%, 26%, 50%, 50%, and 43% for the 0.94, 1.08, 1.28, 1.58, 2.03, 2.69, 2.79, 5.00 μm windows, respectively. At the longer wavelengths of 2.69-5 μm, the uncertainties are larger

due to the lower signal to noise ratio (S/N). In any case, the error bars on the best fit of surface albedos take into account not only S/N limitations, but also errors due to uncertainties on the haze model (typical error on the extinction is 5%). Since the RT code adopts a plane-parallel and a Lambertian approximation and for the accuracy of the results, only VIMS data with geometry observations of both incidence and emergence angles <60º are selected, with only 15% of the data selected having incidence or emergence angles >50º (Table 2). We followed the approach used previously and in the recent study by Es-Sayeh et. al. (2023) where the authors use the RT code with the plane-parallel approximation used in this current analysis as well, and recommend the use of VIMS datacubes with incidence angles up to 50° incidence angle. The phase angle of all selected datacubes are higher than 10-15º and up to 70º and hence the surface behaves almost as Lambertian (Karkoschka et al., 2012). The effects of the phase angle on the I/F value are included in the error bars on our results (Karkoschka et al., 2012; Solomonidou et al., 2014). The spatial resolution of our selected datacubes ranges from 3 to 46 km/pixel (Table 2).

Finally, we use a linear mixing model, as in previous work (Solomonidou et al., 2018; 2020a), to place semi-quantitative constraints on the relative composition of Titan's surface. The model includes a selected spectral library of molecules, used as proxies for Titan candidate materials convoluted to VIMS spectral resolution, in order to examine the compositional properties of the various regions within the Soi crater region. While some of the specific molecules and complex carbonaceous materials included in our mixing model library are not expected to be found on Titan, we have used them to represent complex organic materials. Many of these materials are biogenic in origin, and through terrestrial diagenetic processes have become chemically aromatized and converted into complex refractory materials. The purpose of this exercise is not to imply exact chemical composition, but to constrain the relative types of molecular classes that could be present.

The Titan candidate materials include ices of ammonia (NH_3), carbon dioxide (CO_2), water (H_2O), cyanoacetylene (HC_3N), methane (CH_4), tholins, kerite, asphaltite, three different types of anthraxolites, and amorphous carbon (Quirico and Schmitt 1997; Grundy and Schmitt 1998; Grundy et al., 2002; Bernard et al., 2006; Brasse et al., 2015; GhoSST @ SSHADE database).

Tholins are laboratory-produced materials which may differ from the complex aerosols produced in Titan's atmosphere and later processed at the surface by fluvial/pluvial/aeolian activity. However, their spectral properties have been used in Titan's spectral analyses to simulate the atmospheric haze content.

We use 'methane' as a representative for any aliphatic hydrocarbon solid including alkanes, alkynes, and alkenes (e.g., Lora and Ádámkovics, 2017; Malaska et al., 2017; Faulk et al., 2017; 2020). These other solid aliphatic materials may be part of the compositional mix, however, these larger aliphatic materials will not be liquid since at Titan temperatures only methane, ethane, propane, and 1-butene are liquid. As a proxy for solid materials, methane does not have measurable significant position shifts (i.e., any shifts are much smaller than VIMS resolution). In addition, the optical constants of methane remain virtually unchanged between liquid and solid at 93 K (Grundy et al., 2002). Thus, we use methane as a general proxy for materials (simple organics) although the spectral and optical constant properties of the actual materials could be much more complicated.

The data of the icy components have been calculated with the 'SPECTRIMAG' radiative transfer code for granular surfaces (Douté and Schmitt, 1998), in sets of 15 different pathlengths spanning 2 orders of magnitude. All components in the constituent library are in the VIMS spectrum and hence simulations with the extracted RT albedos are possible. The mixing model fits the RT extracted albedos with the most compatible mixture of the proxy constituents and linear mixtures thereof, inferring at least 4 constituents (Solomonidou et al., 2018; 2020a). The model provides compositional constraints using the limited number of available atmospheric windows

and that entails that there is no unique solution for the mixtures. A perfect fit cannot be achieved between the simulations and the observations because all radiative transfer codes are incapable of totally reproducing the complexity of Titan's system (atmosphere, surface, and interactions among these convoluted elements) and no simple mixture of components can reproduce what exists on the surface of Titan. Our method tests to what extent the available observations (absolute values and spectral shape) can be match with these basic constituents. The code output includes estimated errors of the derived abundances of the different components of the mixture.

Bitumens are used as proxies to lower the total surface albedo (Moroz et al., 1998; Lellouch et al., 2004; Court et al., 2006; Combe et al., 2007; Hirtzig et al., 2012) as it is expected to be low for Titan. Bitumen on Earth is a very complex intractable mixture containing many hydrocarbon and functionalized hydrocarbon components. It derives from coal and petroleum residues which in turn derived from diagenetically processed humic acids, steroids, and wax lignins from buried (usually vegetative) biologically produced organic matter. It is not likely that bitumen as produced on Earth would be exactly present on Titan. However, in the absence of another good analogue for dark materials we have applied this component as a proxy in our simulations. In particular, bitumen contains a large amount of naphthene aromatics (naphthalene), consisting of partially hydrogenated polycyclic aromatic compounds. We use these as a proxy for complex mixtures of Titan aromatic molecules that fused and linked such as (for fused) phenylacetylene, naphthalene, and phenanthrene (Abplanalp et al., 2019) and linked aromatics such as biphenyl, terphenyl and higher homologs. All solid small-molecule organics included in the spectral library are in 15 grain sizes (10, 20, 30, 40, 50, 75, 100, 150, 200, 250, 300, 400, 500, 750, and 1,000 μm), the laboratory tholins in 6 grain sizes (1, 2, 5, 10, 30, and 100 μm), and the amorphous carbon in 3 grain sizes (10, 200, and 500 μm) (Quirico and Schmitt, 1997; Grundy and Schmitt 1998; Grundy et al., 2002; Bernard et al., 2006; GhoSST @ SSHADE solid spectroscopic database). Hence, in total we examined 90 different spectral possibilities. The spectra data used in this study in the VIMS range can be seen in Figure 3.

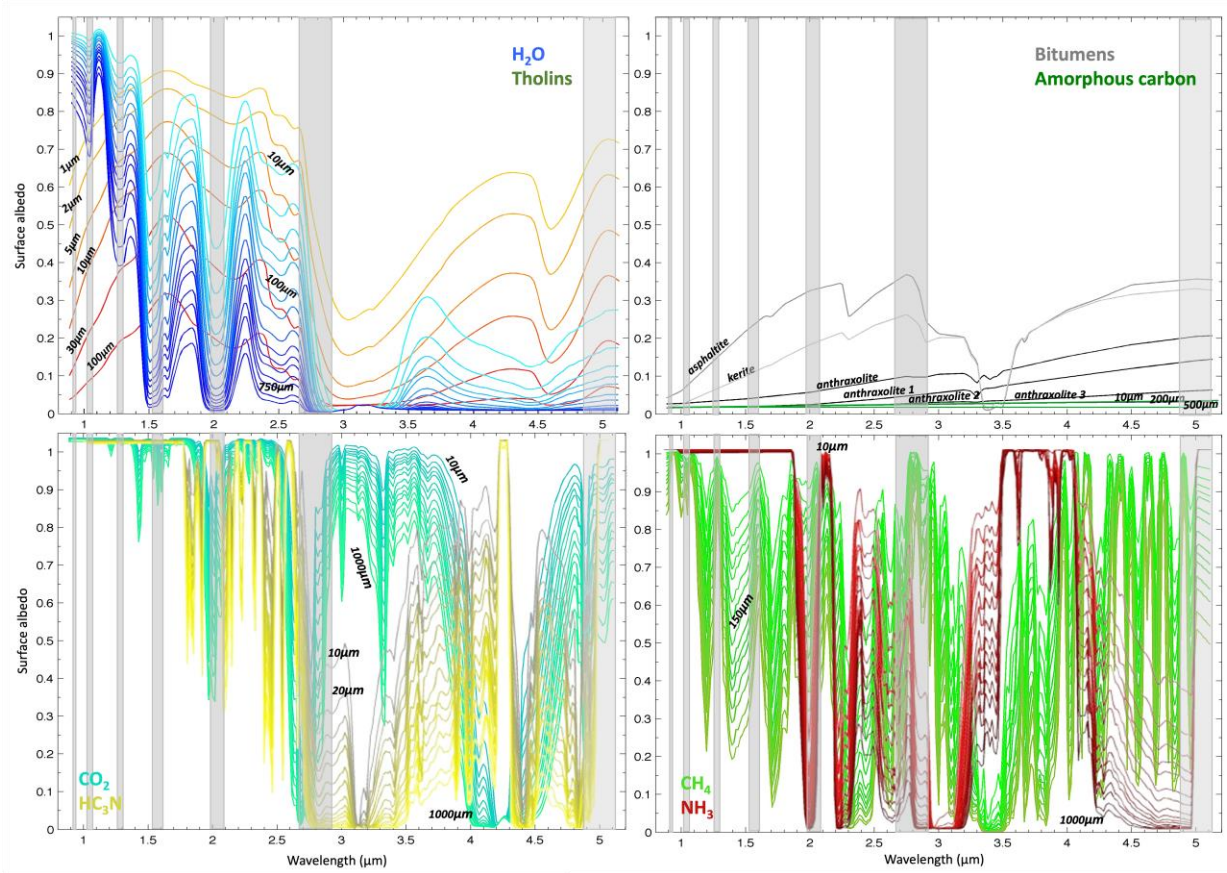

Figure 3. Spectra data of candidate components used in this work adapted from Solomonidou et al. (2020a). H_2O in shades of blue; laboratory tholins in shades of orange; bitumens in gray, and amorphous carbon in dark green; CO_2 in shades of turquoise, and HC_3N in shades of yellow; CH_4 in shades of light green, and NH_3 in shades of red. These spectra are plotted in the spectral range of VIMS at different grain sizes (Bernard et al. 2006; Brassé et al. 2015; GhoSST database, http://ghosst.osug.fr). The light gray columns correspond to Titan's atmospheric windows.

3.2 Haze Estimations and Surface Albedos

The VIMS datacubes shown in Table 2 were acquired at different observational properties and at different times during the Cassini mission (Tb – T113: 2004-2015). The analyzed VIMS pixels from the 261 different locations are expected to include different atmospheric effects, which is something that has been found to occur even at adjacent pixels from within the same VIMS datacube (Solomonidou et al., 2016; 2018). Indeed, the analyses of the VIMS data from the various locations within the Soi crater region showed that the haze contributions to the VIMS data ranges from 70-130% (±5%) with respect to the Huygens Landing Site DISR measurements used a calibration point (Karkoschka & Tomasko, 2010). In particular, the haze contribution to the data seems to present a relative dependance with latitude. Datacubes from flybys Tb, T08, T10, T12, and T77 that cover mostly low to mid latitudes when treated with RT the haze estimation ranges between 70-110%, while from T31 and T97 that cover mostly higher latitudes range from 100-130%.

The examples of extracted surface albedos in the form of weighted averages are shown in Figure 4, including one example for each geomorphological unit and their various types. There are four groups based on their geomorphological characterization: (a) dunes; (b) highlands such as mountainous/hummocky and labyrinth terrains; (c) crater units and SEDs; and (d) plains. In Figure 4 the extracted albedo from HLS is also present for comparative purposes.

The overall albedo values of the dunes (Fig. 4a) at all wavelengths are among the lowest compared to the rest of the units, as demonstrated in previous studies (e.g., Soderblom et al., 2007; Barnes et al., 2008; Rodriguez et al., 2014; Bonnefoy et al., 2016; Solomonidou et al., 2016; 2018; Brossier et al., 2018). The featureless sand sheets (*ds*) present much brighter albedos than the other types of dunes, which we find correlated with their locations, as they appear mostly over 15ºN and are completely absent from the equator. The dark linear dunes (*dl*) and the undivided dunes (*du*) have similar spectral behavior and albedo values within error bars at all wavelengths, except for the 2 μm window where the dark linear dunes have particularly low albedo, suggesting the presence of a constituent very absorbent at this wavelength. The lower albedo at all wavelengths for units closer to the equator is attributed to the transport and incorporation of dark material from the dunes due to aeolian transport processes (Malaska et al., 2016b; Lopes et al., 2016; Solomonidou et al., 2018; 2020a).

The highland terrains (Fig. 4b) present differences in their surface albedos, with the hummocky terrains (*hh*) having low albedo values, agreeing with the results in Solomonidou et al. (2018), and the mountainous terrains (*hm*) presenting significantly high albedo values, especially at the short wavelengths (0.94-2 μm). Interestingly, the undivided hummocky/mountainous terrains (*hu*) have albedo values in between the values of hummocky and mountainous terrains as shown in Fig. (4b). The labyrinth terrains (*lbf*) present relatively high surface albedos, with spectral similarities with the undifferentiated plains (*pul*) (Fig. 4d)

The albedos extracted from crater subunits (Fig. 4c) show that the crater fill 3 (*cf3*) is filled with the same material that is present in the dunes. The crater rim and crater ejecta show very similar spectral behavior and albedo values within error bars, something that was also shown for the Soi crater subunits in Solomonidou et al. (2020a). The albedos of the sharp-edged depressions (*bse*) and of their ramparts (*brh*) are intermediately bright with high values at the double window (2.69-2.79 μm) and the 5 μm window, similarly to the albedos extracted from VIMS data of three empty lake floors at 69ºN-134ºW in Solomonidou et al. (2020b). This study found that the material of the high-latitude empty lake floors is the same as the material of the raised ramparts that appear surrounding less than 10 SEDs of the north pole, suggesting that the ramparts are spectrally distinct from the surrounding plains.

Finally, the plains (Fig. 4d) present a great variety of different albedo values, with the new unit of gradational plains (*pgh*) having the lowest albedo of the plains units, marginally close to that of the dark linear dunes, following the dark linear dunes' drop in albedo from 1.59 to the 2 μm window; a decrease that is not frequently observed in Titan's albedos. The dark irregular (*pil*), the undifferentiated (*pul*), the undivided dark (*pdu*), and the variable (*pfv*) plains present intermediate albedo values at the short wavelengths. The *pfv* is particularly bright at long wavelengths and the *pil* are very bright at the 2.69-2.79 μm double window. This brightness of Soi's *pfv* units at the 2.69-5 μm range was not observed in other locations of variable plains analyzed in Solomonidou et al. (2018) and seems compatible with the high latitude location of the Soi region variables that reach 50º N. The scalloped plains (*psv*) present intermediate to high albedo values at most wavelengths. The streak-like (*psh*) plains are very bright at all wavelengths, agreeing with the results in Solomonidou et al. (2018) and Lopes et al. (2016), while the newly

introduced undivided plains present high albedos at shorter wavelengths (0.94 – 2 μm), as well as at 5 μm.

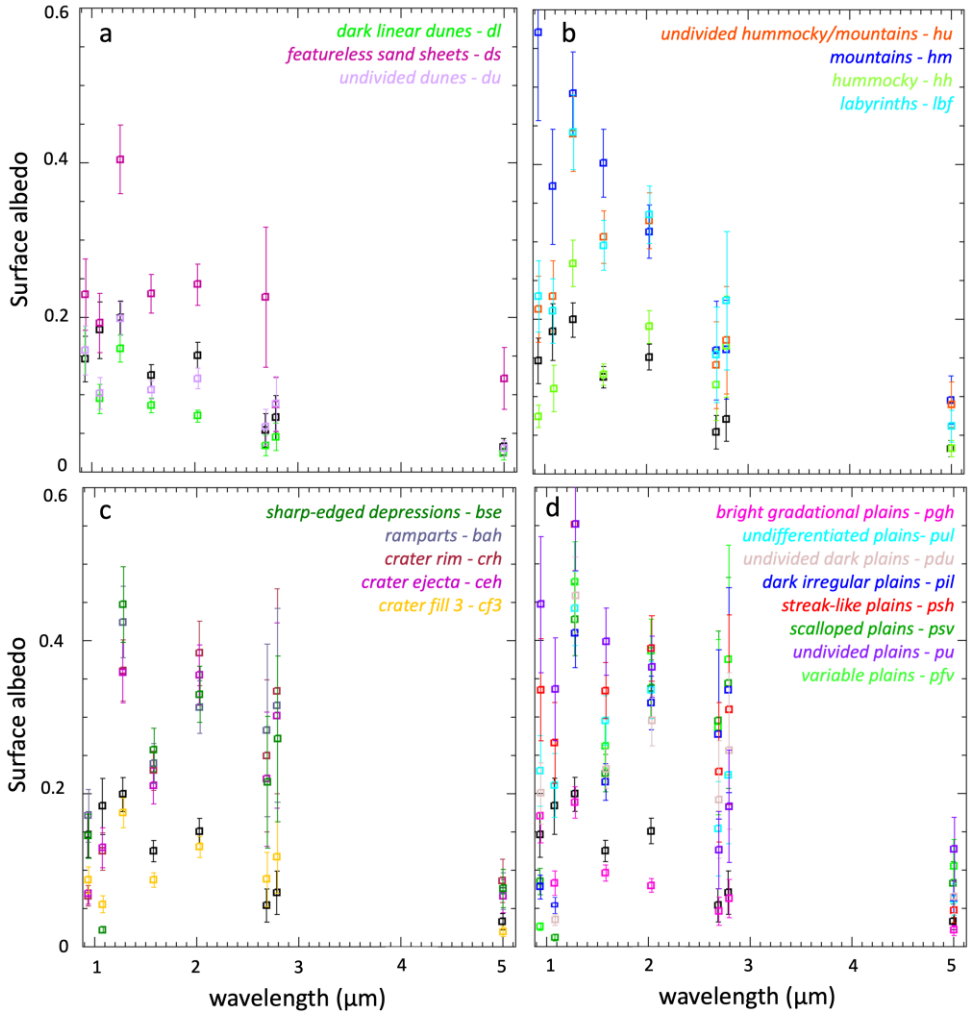

Figure 4. Examples of surface albedo weighted averages in the atmospheric windows as extracted from VIMS data with RT for four different groups of units: (a) dunes; (b) hummocky/mountainous and labyrinth; (c) impact crater units and sharped-edged depressions; and (d) plains. The Huygens Landing Site (HLS) albedos (in black) are used as reference.

3.3 Surface Mixtures

The extracted albedos presented in the previous section are used in the mixing model to provide linear mixture simulations that would fit the albedo data in the most optimal way, given the available albedo points and the candidate Titan materials in the spectral database, and from the perspective of what can be done in such a complex situation with limited available *in situ* observations. Even if the fits between the mixture simulations and the albedo data are not perfect, they provide insights into the surface composition of Titan's top surface layer, which is still unknown even after 13 years of Cassini exploration (e.g., Nixon et al., 2018; MacKenzie et al., 2021). Table 3 includes the results from all 261 locations and Figure 5 presents ternary diagrams for the composition of plains (a), dunes (b), hummocky terrains and labyrinths (c), and craters and

lakes (d). Examples of the mixture simulation results from representative units within the Soi crater region can be found in Figure 6. The χ^2 values from the analyzed areas range from 0.24 to 3.48, suggesting high correlation between the mixture simulations and the albedo data. From first read of Figure 5 it seems that the majority of plains (5a) and hummocky and labyrinth terrains (5c) are lacking the contribution of the dark organic material in their mixtures, something that as expected the dunes (5b) have in abundance. The empty sharp-edged depressions, their surrounding ramparts, and craters on the other hand seem to have a combination of all three constituents in their mixtures.

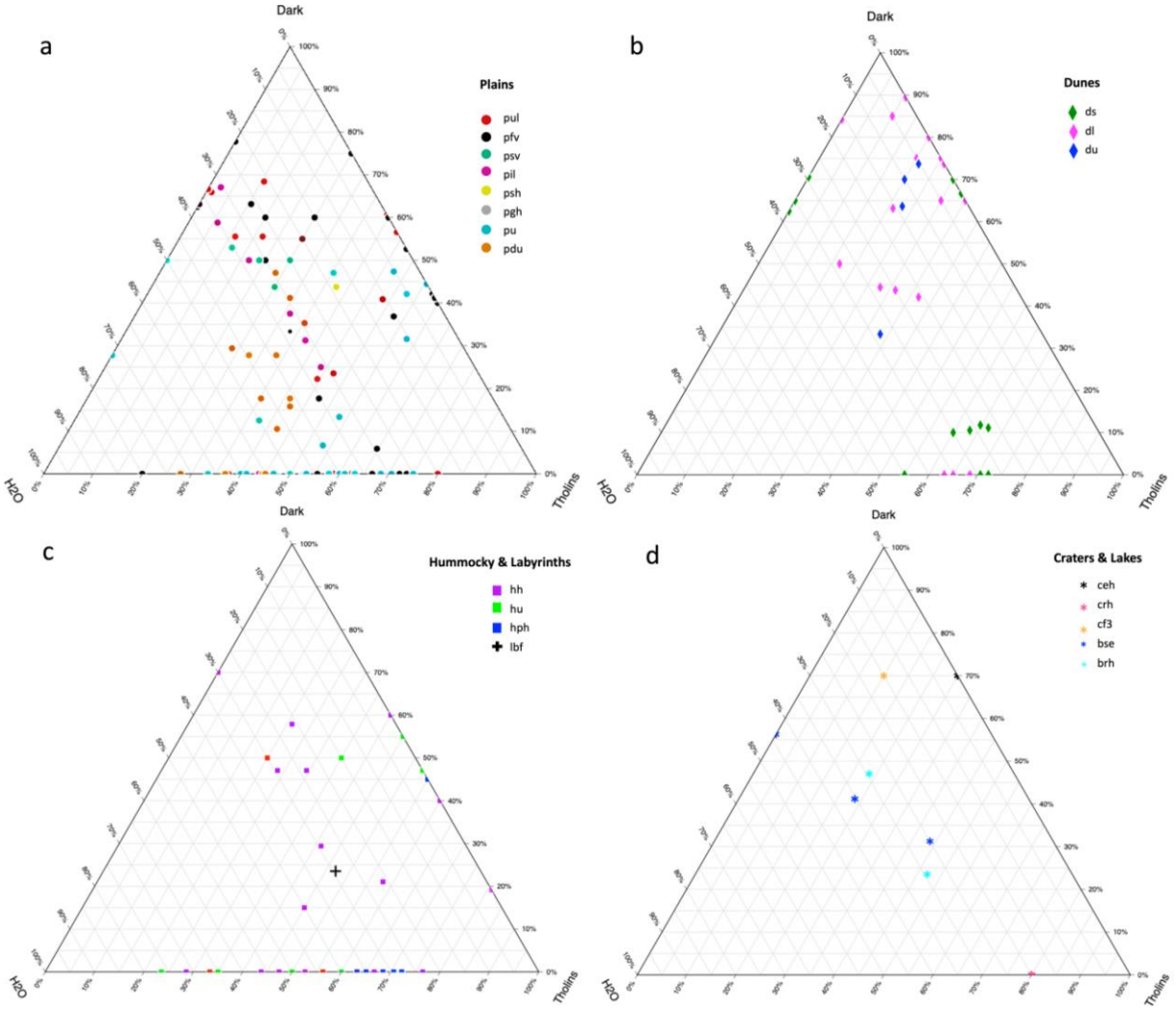

Figure 5. Ternary diagrams representing a composition from the three major constituents: H_2O, tholin-like constituent, and unknown dark constituent. (a) various types of plains; (b) various types of dunes; (c) various types of hummocky terrains and labyrinths; (d) different parts of craters and lake features. Detailed compositional constraints for each unit and their various locations can be found in Table 3.

In our attempts to understand the chemical composition of Titan's surface as well as possible, the code provides simulations of mixtures including at least four major constituents, based on which we built our compositional map for the Soi crater region (see following section). It was particularly difficult to reproduce in some cases the 0.94 and 1.08 μm albedo values,

something that was previously found in Solomonidou et al. (2020a), when studying the composition of Titan's major impact craters. Furthermore, in Solomonidou et al. (2018) in a similar attempt to characterize the composition of the surface, fewer compounds were added from the library, which led to a worse fit especially for 0.94, 2.03, and 2.79μm. In this present study we have added more components in our simulation, increasing the number of component spectra available for potential matches in our library from 75 to 90, when taking into account the grain sizes. For the latter, the best fits are obtained using spectra from specific grain sizes for the different components since the albedo can be very dependent on the grain size, as shown in Figure 3. For the areas where their mixture includes tholins, the best fits are obtained using 30μm and 100μm tholins. For CH_4 ice, the optimal grain size is 1000μm, while for H_2O ice, it ranges from 10μm to 50μm. Finally, among the various bitumens, the ones that provide the best fit with the extracted albedos are amorphous carbon at 200μm and 500μm, along with asphaltite.

In all 261 cases, we obtained matches within error bars in at least four out of the eight wavelengths. Such challenges in spectroscopic analyses for Titan have been faced by previous studies for both ground-based and Cassini-Huygens observations and measurements (VIMS, DISR) (Coustenis et al., 1995; Smith et al., 2005; Tomasko et al., 2005; Brown et al., 2006; Clark et al., 2010; Soderblom et al., 2007). Here, the matches that are more difficult to achieve are at the very short wavelengths, and for some cases the double window (2.69-2.79 μm), and the 5 μm window. The mismatch, especially at the shorter wavelengths, is indicative of the limitations set by the VIMS data, the modeling, and the variability of the material library compared to the expected complexity of Titan's surface. In contrast to previous surface composition simulation studies (Solomonidou et al., 2018; 2020a), here we are better able to match the 2 μm and the 2.79 μm albedo data with mixtures of components. Furthermore, we have a match at 1.59 μm in almost all 261 regions. In addition, some units present very low albedo values at short wavelengths and there is conspicuous absence of fit at 1.08μm compared to other units. Particularly intriguing are the SEDs, ramparts, and labyrinths, which exhibit markedly low albedos at short wavelengths and comparatively higher values at 2.03 and double-window wavelengths (Fig. 6b). This characteristic poses challenges for fitting all atmospheric windows, as the code uses materials within the current databases exhibiting absorption at short wavelengths while strongly reflecting light within the 2.03-2.79μm range. Further work on the Cassini data, along with the advanced development of tools for their processing and additional data from future missions (e.g., Dragonfly) and observations (e.g., JWST), will help us better understand the reasons behind these mismatches and provide solutions for improved fits between the albedos and the simulated surface mixtures.

In the next section we discuss in detail the compositional behavior of each unit. In the next section we discuss in detail the compositional behavior of each unit.

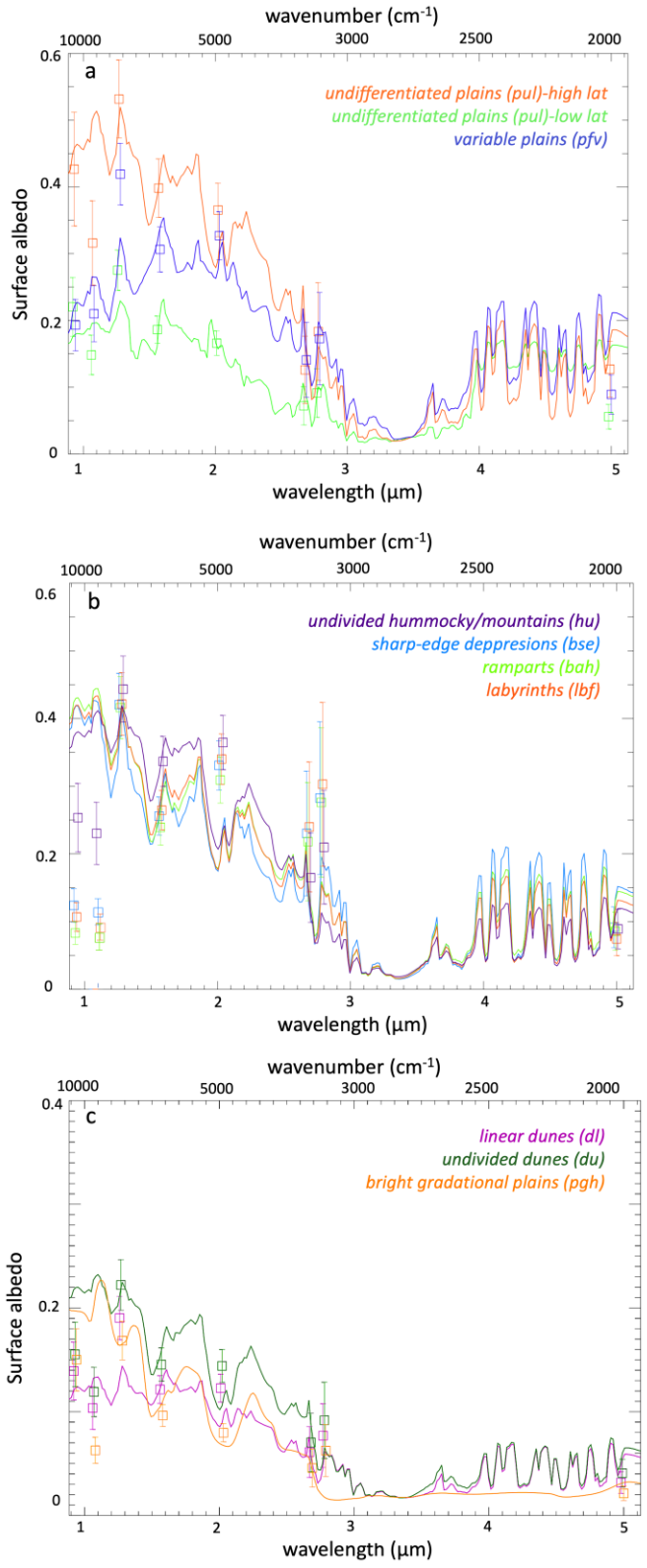

Figure 6. Examples of inferred spectra based on modelled constituent mixtures of different units in the Soi crater region. (a) Examples of an undifferentiated plain from over 30ºN (*pul* -high lat), from close to the equator (*pul* -low lat), and a variable plain (*pfv*). (b) Examples of a sharp-edged

depression (*bse*), of its surrounding rampart (*brh*), a labyrinth terrain (*lbf*), and an undivided hummocky terrain (*hu*). (c) Examples of a linear dune (*dl*), an undivided dune (*du*), and a gradational plain (*pgh*). The point symbols correspond to extracted surface albedos from locations shown in Figure 2 and others, and the full lines to the compositional simulations, which are produced by the code using the best fit attained between the simulated spectra and the albedos. The 3σ error bars are shown on the simulations and are inferred by the code during the extraction of the surface albedos (detailed description of the 3σ error bars can be found in section 3.1).

3.4. Spectral Class Compositional Map

The 261 locations (Figure 2) we analyzed with VIMS from the Soi crater region showed that it is a diverse region in terms of compositional variety for the visible surface (Figure 7; Table 3). Figure 7a shows the extrapolated compositional results of the selected regions of interest as shown in Figure 2 with contact lines distinguishing the boundaries of the various geomorphological units of which we discuss their composition in detail in this section. In Figure 7b, we classified the extrapolated composition from Fig. 7a into ice and organic material; the latter includes the dark material and tholins. Figure 7c shows the results from mapping of the Soi crater region as presented in Schoenfeld et al. (2023). Here, we do not attempt to provide exact molecular composition, given the limitations of the VIMS data described earlier, rather we treat each material as a representative for possible compositions of the upper layer of the surface. Our radiative transfer code takes into account a large number of uncertainties and translates them into error bars as described in section 3.1 and shown in Figures 4 and 6. Given those caveats, we provide constraints on the chemical composition of the surface though the classification of spectral types of materials, focusing on the major constituent of the mixture and up to the 4th constituent in abundance (Table 3). As a reminder, these maps represent compositional constraints of mixtures that possibly make up the very thin veil (few microns) that cover the surface. The deeper layers (few cms) of the surface and their composition are being discussed later in this section (subsection 3.5).

We will examine each unit separately, however one result that is common for all analyzed locations in the Soi crater region is that we found no indication for the presence of significant amounts of carbon dioxide (CO_2), cyanoacetylene (HC_3N), or ammonia (NH_3) ices in the mixtures, to within our aforementioned uncertainties.

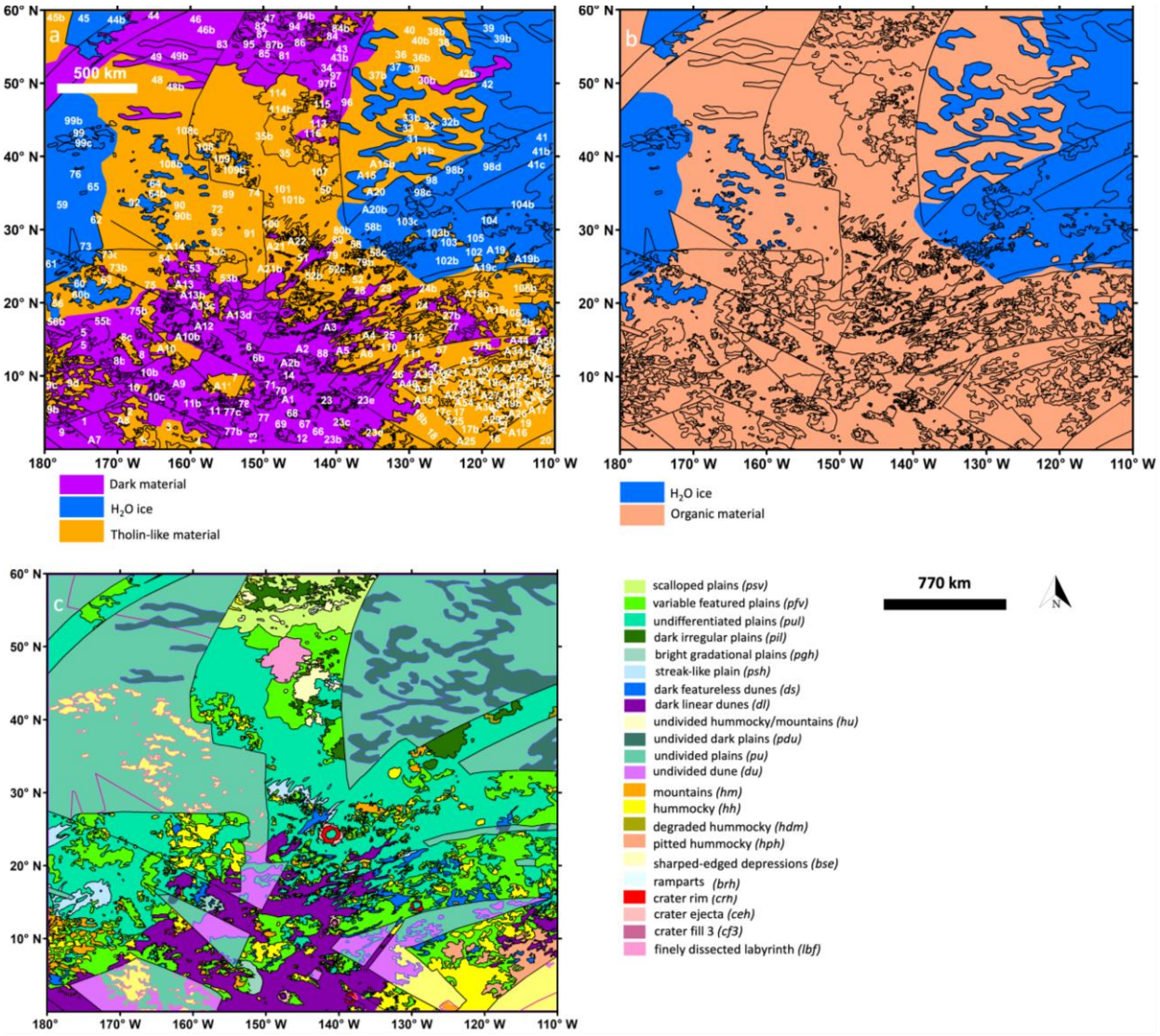

Figure 7. (a) Extrapolated composition map of the Soi crater region for the major constituents from VIMS RT analysis and mixing model simulations with contact lines distinguishing the boundaries of the various geomorphological units based on the boundaries drawn for the geomorpohological map in (c). The numbers represent the selections of regions of interest as shown in Figure 2. The colored pixels are based on their compositional results for the major constituent (blue for water-ice, magenta for dark organic material -a combination of bitumens and amorphous carbon, orange for tholins). (b) Same as (a) with classification between ice (blue) and organic (pink). (c) Geomorphological map for all SAR and non-SAR data (Schoenfeld et al., 2023) at zero transparency (the map layer is fully opaque), same color scheme as the global geomorphological map of Titan in Lopes et al. (2020).

All dune terrain units (*dl*, *du*, *ds*) have a primarily organic nature, but the different units present differences in their secondary materials. The highland terrains (*hh*, *hm*, *hu*, *lbf*) lack a characteristic major constituent among all their different units (Fig. 5c) and their nature depends on their location. One common characteristic of all highland terrains is that they all appear to have tholins in their mixtures (not as a major constituent) in significant amounts and that the presence

of CH_4, as a tertiary or quaternary constituent, in their composition is stronger than in the dunes. The three crater units (*crh*, *ceh*, *cf3*) are primarily organic with the presence of water-ice only in the mixtures when the crater is located in regions dominated by plains (around the 30ºN latitudinal zone), as shown in Solomonidou et al., (2020a). One such example is Soi crater. Furthermore, the composition of the empty sharp-edged depressions (*bse*) and their surrounding ramparts (*brh*) (Fig. 5d) was found to be the same or very similar to those of the north polar empty lakes around 70ºN discussed in Solomonidou et al. (2020b), which is a mixture of organics, water-ice, and simple organics. In Solomonidou et al. (2020b), it is noted that the emissivity of the northern raised ramparts points to a moderate-to-high contamination by organics. This emissivity is comparable to that of the northern empty basins. Combined with the VIMS results, this observation suggests that the ramparts and the empty lake floors, both located at the north pole, may share the same or similar composition. Here, as illustrated in Table 3 and discussed later in section 3.5, and similarly to the northern SEDs, the midlatitide empty SEDs are enriched in organic components.

The plains, in the same way as they present variable morphologies, present complex mixtures in their visible composition. The eight different units of plains are covered by different mixtures of materials. The recently introduced plain type (Schoenfled et al., 2023), the gradational plains (*pgh*), is located close to the equator and below 20ºN and is primarily organic in nature (dark material) and as shown in Fig. (4c) completely covered by dune materials. In contrast, the streak-like plains (*psh*) over 20ºN do not include any dark material in their mixture and appear almost equally rich in water-ice and tholins. Similarly, the undivided dark plains (*pdu*), even though they were expected to be mostly abundant in the organic dark material due to their dark signature in VIMS, are instead relatively richer in water-ice, presenting some of the highest abundances in water-ice within the Soi crater region, along with the highland terrains. The undivided plains (*pu*) and the variable plains (*pfv*) are also covered by a mixture of organics and water-ice. The dark irregular plains (*pil*) and the scalloped plains (*psv*) are spectrally very similar, varying primarily in the amount of dark material present. Counterintuitively, the dark (in SAR) irregular plains, on average, have lower amounts of the dark material component than the scalloped plains. Previous analysis from a couple of scalloped plains (*psv*) from the region, which were analysed in Solomonidou et al. (2018) from older flybys (T25 and T94) than T97 (Table 2) and were found to be mainly abundant in water-ice, here are instead found to be abundant in the dark material (major) and water-ice (secondary). While our model uncertainties are significant, this may represent a change in the surface composition, which we hypothesize to be related to fluvial activity depositing a fresh overlying layer of dark material. Moreover, the dark irregular plains (*pil*) are mainly concentrated in latitudes higher than 30ºN within the Soi crater region and were expected to be primarily rich in water-ice; however, even though water-ice is present in their mixtures, organic material seems to be the most abundant. Lastly, the undifferentiated plains (*pul*) seem to present a similar latitudinal dependence as shown in Solomonidou et al. (2018), with those in the 0-20ºN zone being abundant in the dark material, while those in the higher latitudes being richer in water-ice (see Figure 7a;c). However, a large number of undifferentiated plains sample locations have tholins as the most abundant constituent, making these locations having the highest abundances in tholins. There is a significant amount of CH_4 in some cases reaching even 25% of the total mixture in some samples.

Detailed compositional constraints for each unit and their various locations can be found in Table 3. These are all suggestive compositional constrains and we acknowledge that they can be satisfied by other compositional solutions as well.

3.5 Emissivity results

As explained in Janssen et al. (2016) the presence of water-ice in the near subsurface is strongly indicated by the higher degree of volume scattering observed in radar-bright and low emissivity regions. Indeed, water-ice is highly transparent to microwaves, and therefore allows longer pathlengths which results in a higher probability for microwaves to encounter scatterers embedded in the subsurface. This in turn causes volume scattering, thus enhancing the radar cross-section and lowering the emissivity (Paillou et al., 2008; Janssen et al., 2016). A characteristic range of emissivity values for the different geomorphological units within the Soi crater region can be found in Table 1 in Schoenfeld et al. (2023) and the map of Figure 8. Though somewhat arbitrary, we interpret the units with values lower than 0.90 to be enriched in water-ice in their near subsurface (top decimeter of the regolith), and we interpret units with emissivity (E) values larger than 0.95 to be enriched in organic materials, and all values in between (E=0.90-0.95) to be consistent with a mixture of the two (Werynski et al., 2019; Malaska et al., 2020; Solomonidou et al., 2020a). The units that are more enriched in water-ice in their near subsurface (40 cm to 1 m) according to the emissivity values are the mountains, the hummocky terrains, and the undivided mountains/hummocky. The VIMS analysis agrees with the strong presence of water-ice in these units, which is always present in the mixtures of the top layer surface of these units; at few locations as major constituent (e.g., items 231-234 of Table 3) and except a very few regions of interest (e.g., items 192, 228 of Table 3) located near the equator which are completed coated with organic material (Table 3, items 191-249). However, a notable difference between the emissivity and VIMS/albedo results is the inconsistency in the major constituent of the mixtures at the southeast 'corner' of the Soi crater region of interest. Here, the emissivity data indicate a major water ice constituent (Fig. 8), while VIMS data suggest an organic one, specifically tholin-like material (Figs. 7a and 7b).The units that are more enriched in organic material according to emissivity are the dunes (*dl, ds, du*) with values ranging between 0.93 and 0.98. As shown in the previous section, the VIMS results of the top surface are in agreement with the organic nature of all types of dunes. Other units with strong organic nature according to emissivity include the undivided irregular plains (*pil*, E≥0.97), the undifferentiated plains (*pul*, E≥0.97), the undivided plains (*pu*, E≥0.96), the undivided dark plains (*pdu*, E≥0.94), the streak-like plains (*psh*, E≥0.95), and the labyrinth terrains (*lbf*, E≥0.95). The VIMS RT analysis of the top surface agrees with the organic appearance of *pil*, *pu*, and *pul* (depending on the latitude). However, the undivided dark plains and the streak-like plains appear more abundant in ice than organic material in the first few microns of their surface. It is important to note that the size and extent of the different features plays an important role in their emissivity measurements since small and thin patches of water-ice lying on an organic substrate may not be detected by radiometry. The rest of the units (*psv, pgh, du, cf3, ceh, ceh, brh,* and *bse*) have intermediate emissivity values suggesting a mixture of abundant icy and organic material with emissivity values ranging from 0.92 to 0.94. The VIMS analysis agrees with this icy and organic nature of the top surfaces of these units. Finally, the variable plains (*pfv*) present a large range of emissivity values (E=0.91-0.96) consistent with VIMS analysis suggesting a varying ice vs. organic nature for the unit depending on the location at all depths, from the thin μm veil covering the surface to 10's of centimeters deep in the surface.

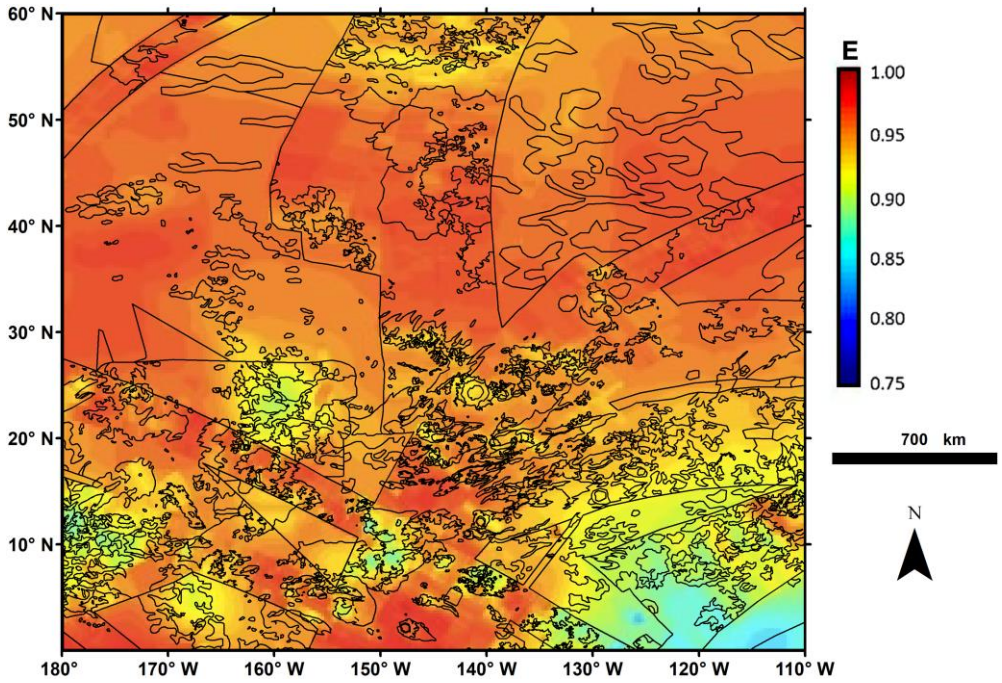

Figure 8. Emissivity map of the Soi crater region with contact lines distinguishing the boundaries of the various geomorphological units. Emissivity data from Janssen et al. (2016).

4 Geologic History of the Soi crater region

4.1 Surface Processes in Soi crater region

The Soi crater region is geomorphologically and compositionally variable, as shown in Figure 7. In this section, we discuss the identified features from the various terrain types within the region and we provide a geologic synthesis with respect to their chemical composition, geomorphology, and potential geologic processes.

Impact processes: There are 10 impact craters identified within the Soi crater region (Wood et al., 2010; Neish et al., 2015; Hedgepeth et al., 2020; Schoenfeld et al., 2023). As also shown in Figure 4c, where the differences in spectral responses between the ejecta and the floors are subtle, the Soi crater region includes characteristic examples of how erosion affects the floors of the craters by allowing dune material to intrude and deposit organic sand.

Inferred Material Transport: Wind and material transport models (Malaska et al., 2016b) have helped distinguish different processes for the Soi crater region. Schoenfeld et al. (2023) presented the sketch map of inferred material direction for the region, which we combined with the map of chemical composition and present in Figure 9. The directions were based on alignments and tapering morphologies of dunes, windstreaks and other terrains which enable the transport direction to be inferred, for details see Malaska et al., (2016b). The map of chemical composition correlates well with the flow path as shown in Figure 9b, with "extensions" of materials suggesting that aeolian transport and subsequent deposition influences surface composition through delivery of fine-grained saltating material (e.g., Schurmeier and Dombard, 2018). For example, in Figure 9b, extended "fingers" of dune materials (purple) are in the tholin-like plains zone (orange area). While the inferred transport direction was determined from geomorphology (primarily by SAR),

it also appears to correlate to the compositional retrieval as well. This compositional analysis further shows that the majority of the equatorial and low latitudes (0-20ºN) are dominated by the dark organic material that transition into an area more dominated by tholin-like materials in the midlatitude. Similarly, mid to high-latitude zone with dark organic spectral components at 50-60ºN transitions to tholins in the midlatitudes (below 50ºN) in a similar fashion. The areas rich in water-ice appear over 20ºN and they are suspected to be unrelated to material transport and deposition and may be more connected to erosional processes. One possible mechanism that could explain these observations would be a surface deposit of equatorially-derived mixed materials, including water-ice and dark materials, which following deposition in the midlatitude plains either have the coating removed (possibly through dissolution/leaching) to reveal a water ice-enriched/tholin lag, or deposition with later coating from bright tholins from atmospheric airfall.

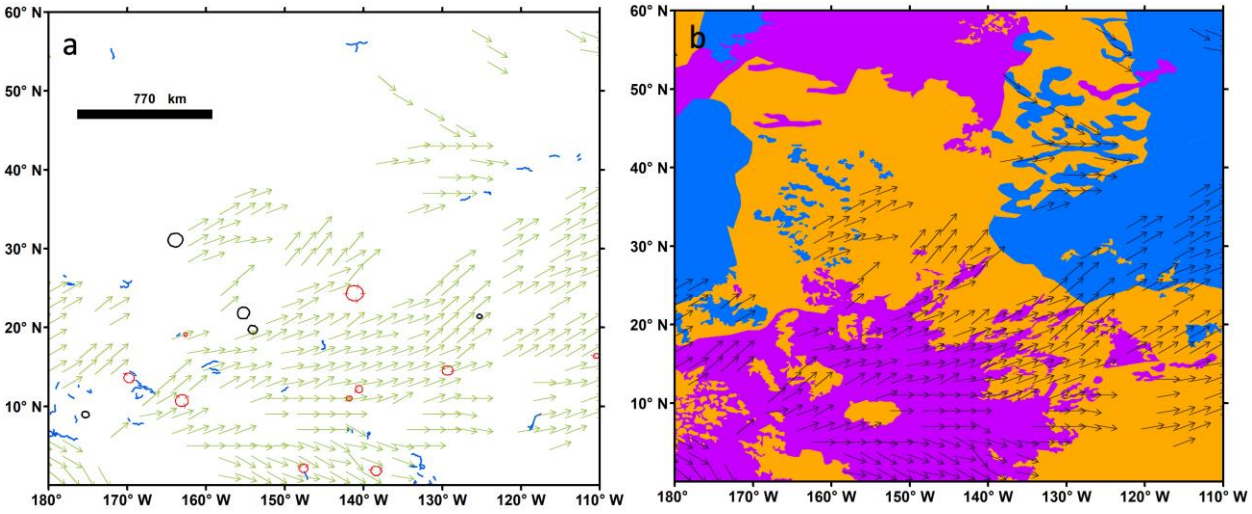

Figure 9. (a) Sketch map of inferred material transport direction (arrows) in the Soi crater region after Malaska et al. (2016b), published in Figure 8 in Schoenfeld et al. (2023), with valleys and channels (blue lines), craters (red), and putative craters (black). (b) Material transport direction on top of the compositional map (color legend in Figure 7b).

Fluvial, Aeolian, and Lacustrine Processes: Two significant units found in the Soi crater region, the bright gradational plains (*phg*) and the bright streak-like plains (*psh*), are proposed to be two endmembers of the same type of fundamental deposit, reflecting either dominantly fluvial or aeolian transport, respectively (Schoenfeld et al., 2023). These aeolian and fluvial origin assumptions are based on geomorphological results from SAR data as presented in Schoenfeld et al. (2013). According to the studies by Schoenfeld et al. (2023) and Malaska et al. (2016), throughout all the mapping datasets the bright gradational plains and the bright streak-like plains have both very similar signatures (bright), diffuse internal texture, and comparable microwave emissivity. The elongated nature of *psh* with directions parallel to adjacent linear dunes suggests aeolian origin for *psh*, while the *pgh* units appear as broad plains originating from alluvial fans and channels. The RT results from the analysis of VIMS data are consistent with these proposed interpretations with regards to their origin (Sections 3.3, 3.4; Figure 4), since in the very top layer of their surfaces, *pgh* is one of the lowest in albedo, which could be consistent with fluvial origin with a surface dampened by liquids. Meanwhile, *psh* is particularly bright at all wavelengths, interpreted as an aeolian deposit with a lack of ponded liquids. As a result the high in albedo values

(bright) *psh* are associated with a dry surface, while the low in albedo values (dark) *pgh* with a wet surface. Radiometry data are inconclusive (*pgh*: 0.92-0.93 and *psh*: 0.94-0.96).

Lacustrine Processes: There are 60 features within the Soi crater region consistent with the morphology and size of the sharp-edged depressions (*bse*) of the north pole (Schoenfeld et al., 2023). In addition, two plains units, the scalloped plains (*psv*) (spectrally analysed in Solomonidou et al., 2018) and the dark irregular plains (*pil*), which are only been found in the midlatitude zone of Titan, are found adjacent to the SEDs (Schoenfeld et al., 2023).

As noted in Malaska et al. (2016a) and Lopes et al. (2020) both units play an important role in the definition of the mid-to-pole transitional zones and due to morphological and microwave emissivity measurements it is suggested that the *psv* is a unit with a thick organic layer much like the undifferentiated plains (Schoenfeld et al., 2021), with which the spectral analysis agrees, suggesting an organic nature with the dark material being dominant (Fig. 6). However, compositional analysis of the *psv* unit suggests that the second most abundant material in the optical surface is water-ice. We propose that this material is mostly organics at depth (consistent with microwave emissivity), but with an optical coating on the top consistent with spectral analysis, which is the opposite of what seems to occur at the Xanadu part of the Soi crater region. As discussed earlier, temporal analysis reveals an interesting temporal albedo change, with two particular *psv* becoming more abundant in dark material in 2014 (T97) than they were in 2007 (T25) and 2013 (T94) (Solomonidou et al., 2016; 2018). All *pil* and *bse* share similar estimated compositions with *psv* having dark material and water-ice mainly in the mixtures of their top layer.

4.2 Correlation of morphology and composition

We have analyzed the Soi crater region and identified various combinations of mixed materials in the top layer of the surfaces of the 22 geomorphological units, including organics, methane, and water-ice.

Our compositional mapping provides a glimpse into the compositional evolution of Titan. Similar to lower equatorial regions, we find abundant dark material to be the major constituent of a mid to high-latitude region (>40ºN, Fig. 7a). This is also the area where scalloped plains are 'hosting' the midlatitude SEDs and the dark irregular plains (40-60ºN, 140-170ºW). In addition, methane-like (simple organics) spectral features are found widespread in the Soi crater region. The high emissivity results consistent with organic materials agree with the constraints put by the VIMS results except for two units: the dark irregular plains and the streak-like plains and the Xanadu region included in the Soi crater region, suggesting compositional differences in the μm to cm layers.

In early VIMS studies, the major spectral "bright" units were found to generally correspond to mountains and elevated areas in radar (Barnes et al., 2007). Our results from the Soi crater region show that there is a significant amount of tholins that appears to be covering the top layers of the hummocky and mountainous terrains at the low latitudes (Fig. 7a), even though the vast majority of the low latitudes of the Soi region is covered with the dark organic material. Notably, another group of hummocky terrains is located in the midlatitudes (30-50ºN) of the Soi crater region and consists mainly of water-ice with a secondary component of tholins. One common characteristic of all highland terrains is that they all appear to have tholins in their mixtures in significant amounts and/or significant amounts of H_2O ice. In addition, the percentage of methane-like materials (simple organics – aliphatic hydrocarbons) in top surfaces found at higher latitudes is larger than those found at lower latitudes (Table 3). Exposed crater rims show a mixture of only water-ice and tholins, suggesting that after the impact revealed water-ice (Crosta et al., 2021), it

was then coated in tholin, but not dark material. However, some highland areas that are exposed to significant fluxes of dune material also show dark material present, while those more protected appear to have less dark material present. In Solomonidou et al. (2018) the hummocky/mountainous units (all located near the equator and 210-245ºW) were among the darkest, while in the Soi crater region they are the brightest in the short wavelengths suggesting some combination of materials that made them very bright at the short wavelength, which we attribute to increased tholin presence. The labyrinth terrains, even though they only appear in the Soi region at a specific location at around 50ºN and represent only ~0.4% of the entire Soi crater region, spectrally look very similar to the ones analyzed in Solomonidou et al. (2018), namely Junction, Tleilax, and Richese and those in Malaska et al. (2020). The Soi region labyrinths are spectrally very similar to the undivided plain materials (*pu*), in both derived RT VIMS and microwave emissivity. They are both consistent with a surface of tholins and water-ice with bulk suggesting mostly organics.

Most craters with the Soi crater region appear to be almost entirely buried under organic material. The ones close to the equator lack any water-ice and are predominantly organic-rich, while the Soi crater rim and ejecta are rich with tholins, followed by water-ice, as also suggested in Solomonidou et al. (2020a).

The undivided dark plains (*pdu*) present some of the highest estimated percent abundances of water-ice within the Soi crater region, along with the hummocky/mountainous terrains. There are, however, three *pdu* high latitude exposures rich in the dark material mixed with water-ice. These differences of the optical surface between the different locations of the same unit suggest that either aeolian or fluvial activity removed part of the optically thin coat of the surface and revealed underlying, possibly wet material. Similarly, the absence of the dark organic material in the undivided plains (*pu*) could be attributed to aeolian and/or fluvial processes that have removed these materials from the visible surface.

Finally, most cases of the featureless sand sheets unit (*ds*), which only appear over 15ºN, appear to be midway in composition between dune sands and midlatitude plains. That is, relative to the dunes, the sand sheet material has less dark material, but more tholin material. This is in contrast to the nature of the linear dunes (*dl*) of the Soi crater region, which are very consistent with having a dark organic composition, at least on the top surface. The featureless nature of *ds* and the fact that the tholins are often secondary suggests either an addition of tholin material to change the relative percentage, or a removal of dark materials. The generic results on the dune unit agree with the organic and less water ice nature of the VIMS ‘brown’ unit that corresponds to the dunes as per previous studies (Barnes et al., 2007; Soderblom et al., 2007).

Previous studies have highlighted a notable correlation between the chemical composition of the thin layer covering Titan's surface, as observed by VIMS (with a thickness on the order of micrometers), and latitude (Lopes et al., 2016; Malaska et al., 2016; Solomonidou et al., 2018; 2020a). While there are instances where geomorphology and composition coincide, such as the distinct 'icy' undivided hummocky terrains (*hu*) within the expansive undivided plains (*pu*) of organic origin at midlatitudes, the influence of latitude, as well as aeolian and fluvial processes, appears to exert significant control over the surface material comprising the thin top layer.

4.3 Interpreted geologic history

The Soi crater region has the typical geomorphology of most of Titan’s surface. It contains plains, dunes, and mountainous terrains (Malaska et al., 2016a; Lopes et al., 2020; Schoenfeld et al., 2021; 2023) and a latitudinal dependence in chemical composition revealing almost complete

coverage of organic material in the equatorial regions and a surface expression of water-ice in the midlatitudes (Solomonidou et al., 2018; 2020b). However, at the higher latitudes a different geologic history is apparent for the Soi crater region.

The presence of dry lakes into the midlatitudes as low as 40ºS supports the hypothesis that Titan had a wetter climate in the past (e.g., Moore et al., 2014). At these midlatitudes, scalloped plains and dark irregular plains have been identified (Schoenfeld et al., 2023) adjacent to the SEDs; this plain/lake northern area is one of the most interesting parts of the Soi region given that it is the first time that the dark organic material has been identified in abundance in a mid-to-high latitude area in the VIMS RT analysis (Fig. 7a).

Our results show that the areas around latitude 35ºN are dominated by surface spectral responses typical of tholin materials, with ice-like materials and dark materials as minor components. Compared to the lower latitudes, there is an enhanced presence of aliphatic hydrocarbon-like materials (methane) in the midlatitudes, while in the higher latitudes, there is an even greater presence. Our compositional analysis is consistent with a gradation of aliphatic hydrocarbon materials being low at the equator, and increasing in relative percentage at higher latitudes (e.g., Mitchell, 2008; Rannou et al., 2006; Tokano et al., 2005; Faulk et al., 2017). The equatorial regions and high midlatitude plains units both contain elevated amounts of dark materials with a lower amount of tholin material when compared to the midlatitude plains units.

From arguments presented in Malaska et al. (2016b) on material transport, Titan's midlatitude regions appear to be areas fed from converging material coming from high latitudes towards the SE, and from equatorial areas towards the NE. This suggests that the midlatitude regions are composed of end stage of Titan windblown deposited materials that have since been subjected to rainfall and perhaps other aging processes. We find that materials at these convergent latitudes are spectrally similar to tholin-like materials and water ice-like materials. In order to convert dune materials and polar plains materials to midlatitude materials requires either removing the dark material component, or adding additional tholin components.

Addition could be due to density-selective transport, if we assume that all three materials have differing densities and/or material properties. For fluvially transported materials, large-scale storms (Faulk et al., 2017) have the potential to transport significant quantities of sediment as overbank deposits. If the tholins and water-ice materials are particularly buoyant compared to the dark materials, then floodplains should lack any significant dark material components. With greater spatial resolution, we would therefore expect floodplains to have a decreasing dark material component away from any given channel. Previous authors have noted the lack of channels in the midlatitude plains (Miller et al., 2021), although there may be effects that obscure the radar signature. In contrast, aeolian processes may transport all three types of sedimentary materials at any given time. To explain the dearth of dark materials at the convergent latitudes, we therefore require that such materials simply do not get deposited there. This could be due to either physical or chemical breakdown over short transport distances, or that the dark materials are denser than the other two sedimentary materials and get left behind due to density-selective transport. In this scenario, we postulate that dark materials may be denser and/or weaker, with both fluvial and aeolian mechanisms acting to sort Titan's different sedimentary materials. This would be analogous to size-selective transport on Earth, except with density playing the role in giving rise to uniquely separated deposits of sedimentary materials.

An alternative possibility is the removal of the dark organic component from the material deposited at the convergent latitudes. Tholin materials and water-ice materials are both predicted to be among the least soluble materials on Titan and would theoretically form a remnant lag

deposit, as more soluble materials, which could possibly include the dark materials, were leached away into the subsurface by occasional rainfall. Leaching in geology corresponds to loss of soluble substances from the top layer of the surface by percolating precipitation. Dark materials are present in deposits to the N and in dune materials in the S in the Soi crater region. Since the dark materials are present in presumably wetter polar deposits, we postulate that some of the dark materials may be sourced there (possibly involving lakes or fluvial activity), while the midlatitudes create a "sink" for these materials. We thus present an alternative compositional evolution cycle where grains and materials coated in dark materials are delivered through aeolian transport into the deposition belts and subjected to extensive leaching which dissolves the dark materials and allows those dissolved materials to percolate into the deep subsurface, thus creating remnant optical surface lag of insoluble materials rich in either water-ice or tholins (Fig. 10). This implies that grains coated in dark materials are more recently formed and have not had their dark material coatings removed. This also implies that dark material would be sourced at high latitudes (for northern polar regions) and at low latitudes (for equatorial dunes).

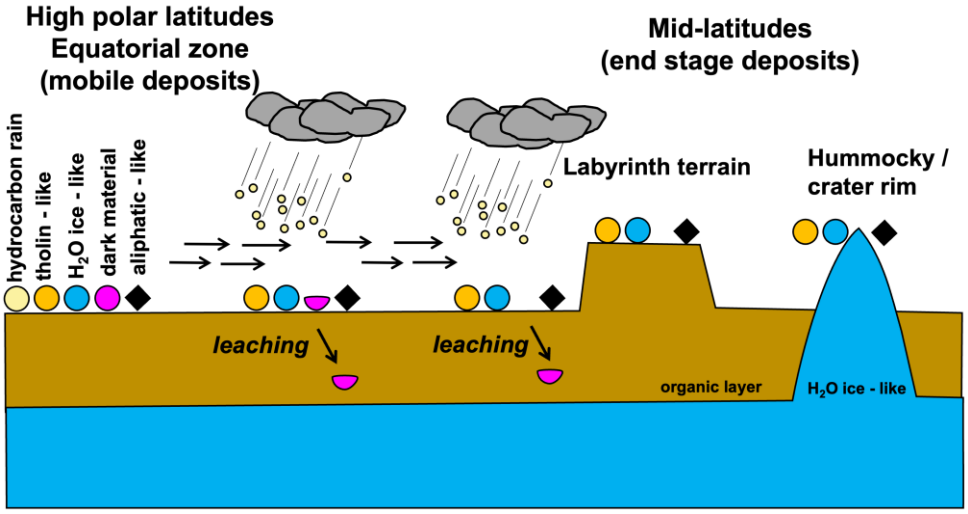

Figure 10. Scheme showing midlatitude leaching of dark material from episodic rainfall on Titan.

Older exposed terrains thus should also be composed of tholins and water-ice materials, as long as they are not receiving new dark material inputs. Thus, the mountains in the SE section of Figure 7c, which is part of the extreme part of Northern Xanadu, appear to be 'protected' from dark material deposition, or, most likely that removal process of the dark material have proceeded quicker than overall deposition. Overall, we envision a scenario as shown in Figure 10, where mobile materials contain dark material, that becomes leached, likely from episodic rainfall, as it arrives to its end-stage destination in the midlatitudes. This scenario as pictured also is supported by microwave emissivity data, which probes deeper. While end stage surface lag composed of tholins coats labyrinth, mountain, and plains almost equally, the deeper probing microwave emissivity can discriminate between hummocky and mountain materials composed of water-ice, and scalloped/undifferentiated plains and labyrinths composed of organic materials.

5 Conclusion

The Soi crater region is an important Titan region as it represents the transition between the equatorial, the midlatitudes, and the high-altitudes of the northern hemisphere of Titan. Our analysis developed a working hypothesis for the formation and evolution of the Soi crater region through the combination of the geomorphological mapping performed by Schoenfeld et al. (2023) and compositional mapping and radiative transfer analysis performed here. Our work suggests propable relationships between the dunes (source), scalloped plains (source), and undifferentiated plains (sink) and brings together and explains the differences in nature of the top layers of the surface from infrared spectra and microwave emissivity measurements. It also infers the geological processes and relationships responsible for their formation and evolution. We suggest that the dark material is a mobile unit that indicates "young" terrains and compositions, while tholin/water-ice mixtures that dominate areas around latitude 35ºN show a material that is older and closer to end stage aeolian plain deposits. This suggests that Titan's compositional evolution cycle includes aeolian transport and leaching. These results provide a better understanding of the geologic processes that govern Titan's surface and will help enhance the science return of future missions such as Dragonfly, and other mission concepts (e.g., Tobie et al., 2014; Lorenz et al., 2021; Barnes et al., 2021; Sulaiman et al., 2021; Rodriguez et al., 2022).

Acknowledgments

We would like to thank the two anonymous reviewers for their thoughtful comments and efforts towards improving our manuscript. This research was partly supported by the NASA Astrobiology Institute through its JPL-led project entitled Habitability of Hydrocarbon Worlds: Titan and Beyond. This research was partly supported by the *Cassini* Data Analysis and Participating Scientists Program (CDAPS) grant #NH16ZDA001N to R.L. A.S. and A.C. acknowledge support from the CNES Appel annuel à Propositions de Recherche Program. A.S. was partly supported by the Czech Science Foundation (grant no. 20-27624Y). S.P.D.B. acknowledges support from the Heising-Simons Foundation (51 Pegasi b Fellowship). Part of this work was conducted at the Jet Propulsion Laboratory (JPL), California Institute of Technology (Caltech) under contract with NASA, and the Hellenic Space Center. ©2023 California Institute of Technology. Government sponsorship acknowledged.

Open Research

All *Cassini* data used in this article can be accessed in the Planetary Data Systems (PDS), PDS Image Atlas (https://pds-imaging.jpl.nasa.gov/search/?fq=-ATLAS_THUMBNAIL_URL%3Abrwsnotavail.jpg&fq=ATLAS_MISSION_NAME%3Acassini&fq=ATLAS_INSTRUMENT_NAME%3Avims&fq=TARGET%3Atitan&q=*%3A*) for VIMS and (https://pds-imaging.jpl.nasa.gov/search/?fq=ATLAS_MISSION_NAME%3Acassini&fq=TARGET%3Atitan&fq=-ATLAS_THUMBNAIL_URL%3Abrwsnotavail.jpg&fq=ATLAS_INSTRUMENT_NAME%3Aradar&q=*%3A*) RADAR. The detailed product IDs for VIMS can be found in Table 2. The spectral library databases can be accessed here: http:// ghosst.osug.fr. Full descriptions of the

radiative transfer model are provided by Hirtzig et al., (2013) (https://doi.org/10.1016/j.icarus.2013.05.033). The VIMS analysis was done using the ENVI Imaging and Analysis software (https://www.l3harrisgeospatial.com/Software-Technology/ENVI) and the Interactive Data Language (IDL), both provided by L3Harris Geospatial.

References

Abplanalp, M.J., Frigge, R., Kaiser, R.I., (2019). Low-temperature synthesis of polycyclic aromatic hydrocarbons in Titan's surface ices and on airless bodies. Sci Adv. 5(10), eaaw5841.

Barnes, J. W., Brown, R. H., Turtle, E. P., McEwen, A. S., Lorenz, R. D., Janssen, M., et al. (2005). A 5-micron-bright spot on Titan: Evidence for surface diversity. Science, 310, 92–95.

Barnes, J.W., Brown, R.H., Soderblom, L., Buratti, B.J., Sotin, C., Rodriguez, S., Le Mouelic, S., Baines, K.H., Clark, R., Nicholson, P., (2007). Global-scale surface spectral variations on Titan seen from Cassini/VIMS. Icarus 186, 242–258.

Barnes, J.W., et al. (2008). Spectroscopy, morphometry, and photoclinometry of Titan's dunefields from Cassini/VIMS. Icarus 195, 400–414.

Barnes, J. W., Hayes, A. G., Soderblom, J. M., MacKenzie, S. M., Hofgartner, J. D., Lorenz, R. D., Turtle. E.P., Radebaugh, J., Burr, D., Lora, J., Neumann, G., Vance, S., Lopes, R., Nixon, C., Corlies, P., Regoli, L., Sciamma-O'Brien, E., Schindhelm, R., Rodgriguez, S., Coll, P., Le Mouélic, Heslar, M., Dhingra, R., Stekloff, J., Sittler, E., Solomonidou, A., Malaska, M.J., Neish, C., Teanby, N., Vinatier, S., Birch, S, Hörst, S., Coustenis, A., Karkoschka, E., Czaplinksi, E., Hayne, P., Brueshaber, S.R., Maue, T. A.D., Dong, C., Cornet, T., McEwen A., Ramirez, K., Royer, E., Salama, F., Koeppel, A. Fenton, L.K., Goudge, T.A., Cable, M.L., Denk, T., Vu, T.H., Nna-Mvondo, D., Cordier, D., Lebonnois, S., Coates, A., Lefticariu, L., Battalio, J..M., Fagents, S., Tortora, P., Beyer, R.A., Momary, T.W., Gurwell, M.A., Schurmeier, L., Neveu, M., Hanley, J., Limaye, A.B., Daudon, C., Desai, R. T. (2021). New Frontiers Titan Orbiter. Bulletin of the AAS, 53(4). https://doi.org/10.3847/25c2cfeb.4c2df948.

Bernard, J.-M., Quirico, E., Brissaud, O., Montagnac, G., Reynard, B., McMillan, B.P., Coll, P., Nguyen, M.-J., Raulin, F., Schmitt, B. (2006). Reflectance spectra and chemical structure of Titan's tholins: Application to the analysis of Cassini Huygens observations. Icarus, 185, 301-307.

Birch, S. P. D., Hayes, A. G., Howard, A.D., Moore, J.M., Radebaugh, J. (2016). Alluvial Fan Morphology, distribution and formation on Titan. Icarus, 270, 238–247.

Bonnefoy, L.E., Hayes, A.G., Hayne, P.O., Malaska, M.J., Le Gall, A., Solomonidou, A., Lucas, A., 2016. Compositional and spatial variations in titan dune and interdune regions from Cassini VIMS and RADAR. Icarus 270, 222–237.

Boudon, V., Rey, M., Loete, M. (2006). The vibrational levels of methane obtained from analyses of high-resolution spectra. J. Quant. Spectrosc. Radiat. Trans. 98, 394–404.

Brassé, C., Munoz, O., Coll, P., Raulin, F. (2015). Optical constants of Titan aerosols and their tholins analogs: Experimental results and modeling/observational data. Planetary and Space Science, 109-110, 159-174.

916 Bratsolis, E., Bampasidis, G., Solomonidou, A., Coustenis, A., (2012). A despeckle filter for the
917 Cassini synthetic aperture radar images of Titan's surface. Planetary and Space Science, 61,
918 108–113.
919 Brossier, J.F., Rodriguez, S., Cornet, T., Lucas, A., Radebaugh, J., Maltagliati, L., Le Mouélic, S.,
920 Solomonidou, A., Coustenis, A., Hirtzig, M., Jaumann, R., Stephan, K., Sotin, C., (2018).
921 Geological evolution of titan's equatorial regions: possible nature and origin of the dune
922 material. JGR, 123, 1089–1112.
923 Brown, R. H., et al. (2006). The Cassini Visual and Infrared Mapping Spectrometer (VIMS)
924 Investigation. Space Science Reviews, 115(1-4), 111-168.
925 Burr, D.M., Perron, J.T., Lamb, M.P., Iriwin, R.P. III, Collins, G.C., Howard, A.D., Sklar, L.S.,
926 Moore, J.M., Ádámkovics, M., Baker, V.R., Drummond, S.A., Black, B.A., (2013). Fluvial
927 features on Titan: Insights from morphology and modeling. Geological Society of America
928 Bulletin 125, 299-321. doi: 10.1130/B30612.1
929 Campargue, A., Wang, L., Mondelain, D., Kassi, S., Bézard, B., Lellouch, E., Coustenis, A., de
930 Bergh, C., Hirtzig, M., Drossart, P. (2012). An empirical line list for methane in the 1.26-1.71
931 μm region for planetary investigations (T=80-300 K). Application to Titan. Icarus, 219, 110-
932 128.
933 Campargue, A., Lopez, S., Beguier, S., Kassi, S., Mondelain, D., (2015). The absorption spectrum
934 of 13CH4 in the region of the 2ν3 band at 1.66 μm: Empirical line lists and temperature
935 dependence. Journal of Quantitative Spectroscopy and Radiative Transfer, 152, 140-148.
936 Clark, R.N., Curchin, J.M., Barnes, J.W., Jaumann, R., Soderblom, L., Cruikshank, D.P., Brown,
937 R.H., Rodriguez, S., Lunine, J., Stephan, K., Hoefen, T.M., Le Mouelic, S., Sotin, C., Baines,
938 K.H., Buratti, B.J., Nicholson, P.D., (2010). Detection and mapping of hydrocarbon deposits
939 on Titan. Journal of Geophysical Research 115, E10005. doi: 10.1029/2009JE003369.
940 Combe, J-P., McCord, T.B., Hayne, P., Hansen, G.B., (2007). Titan's Surface Composition
941 Investigated by Spectral Mixture Analysis of VIMS/Cassini Data. American Astronomical
942 Society, DPS meeting #39, 44.03, Bulletin of the American Astronomical Society, 39, 500.
943 Corlies, P., McDonald, G.D., Hayes, A.G., Wray, J.J., Ádámkovics, M., Malaska, M.,J., Cable,
944 M.L., Hofgartner, J.D., Hörst, S.M., Liuzzo, L.R., Buffo, J. J., Lorenz, R.D., Turtle, E.P.,
945 (2021). Modeling transmission windows in Titan's lower troposphere: Implications for infrared
946 spectrometers aboard future aerial and surface missions. Icarus 357, 114228. doi:
947 10.1016/j.icarus.2020.114228.
948 Court, R.W., Sephton, M.A., Parnell, J., Gilmour, L., (2006). The alteration of organic matter in
949 response to ionising irradiation: Chemical trends and implications for extraterrestrial sample
950 analysis. Geochimica et Cosmochimica Acta, 70, 4, 1020-1039.
951 Coustenis, A., (1995). Titan's Surface: Composition and Variability from the Near-Infrared
952 Albedo. Icarus, 118, 87-104.
953 Coutelier, M., Cordier, D., Seignovert, B., Rannou, P., Le Gall, A., Cours, T., Maltagliati, L.,
954 Rodriguez, S., (2021). Distribution and intensity of water ice signature in South Xanadu and
955 Tui Regio. Icarus, 364, 114464.
956 Crosta, A., Silber, E., Lopes, R., Johnson, B., Bjonnes, E., Malaska, M., Vance, S., Sotin, C.,
957 Solomonidou, A., Soderblom, J., (2021). Modeling the formation of Menrva impact crater on
958 Titan: Implications for habitability. Icarus 370, 114679.
959 de Kok, R., Irwin, P., Teanby, N., Lellouch, E., Bézard, B., Vinatier, S., Nixon, C., Fletecher, L.,
960 Howett, C., Calcutt, S., Bowles, N., Flasar, F.M., Taylor, F. (2007). Oxygen compounds in
961 Titan's stratosphere observed by Cassini CIRS. Icarus, 186, 354-363.

962 Evans, K.F. (2007). SHDOMPPDA: A Radiative Transfer Model for Cloudy Sky Data
963 Assimilation. J. Atmos. Sci., 64, 3854–3864.
964 Faulk, S., Mitchell, J., Moon, S., Lora, J., (2017). Regional patterns of extreme precipitation on
965 Titan consistent with observed alluvial fan distribution. Nature Geoscience, 10, 827-832.
966 Faulk, S., Lora, J., Mitchell, J., Milly, P.C.D., (2020). Titan's climate patterns and surface methane
967 distribution due to the coupling of land hydrology and atmosphere. Nature Astronomy, 4, 390-
968 398.
969 Fulchignoni, M., Ferri, F., Angrilli, F., Ball, A.J., Bar-Nun, A., Barucci, M.A., Bettanini, C.,
970 Bianchini, G., Borucki, W., Colombatti, G., Coradini, M., Coustenis, A., Debei, S., Falkner, P.,
971 Fanti, G., Flamini, E., Gaborit, V., Grard, R., Hamelin, M., Harri, A.M., Hathi, B., Jernej, I.,
972 Leese, M.R., Lehto, A., Lion Stoppato, P.F., López-Moreno, J.J., Mäkinen, T., McDonnell,
973 J.A.M., McKay, C.P., Molina-Cuberos, G., Neubauer, F.M., Pirronello, V., Rodrigo, R.,
974 Saggin, B., Schwingenschuh, K., Seiff, A., Simões, F., Svedhem, H., Tokano, T., Towner,
975 M.C., Trautner, R., Withers, P., Zarnecki, J.C., 2005. In situ measurements of the physical
976 characteristics of Titan's environment. Nature 438, 785-791. doi: 10.1038/nature04314.
977 Gordon, I.E., et al. (2022). The HITRAN2020 molecular spectroscopic database. Journal of
978 Quantitative Spectroscopy & Radiative Transfer, 277, 107949.
979 Greeley, R., & Batson, R. M. (1990). Planetary mapping. Cambridge University Press.
980 Greeley, R., et al., (2000). Geologic Mapping of Europa. JGR-Planets, 105, E9, 22559-22578.
981 Grundy, W.M., Schmitt, B., (1998). The temperature-dependent near-infrared absorption spectrum
982 of hexagonal H2O ice. Journal of Geophysical Research – Planets, 103, E11.
983 Grundy, W.M., Schmitt, B., Quirico, E., (2002). The Temperature-Dependent Spectrum of
984 Methane Ice I between 0.7 and 5 μm and Opportunities for Near-Infrared Remote Thermometry.
985 Icarus, 155, 486-496.
986 Hedgepeth, J.E., Neish, C.D., Turtle, E.P., Stiles, B., Kirk, R., Lorenz, R.D. (2020). Titan's impact
987 crater population after Cassini. Icarus, Icarus, 344, 113664.
988 doi.org/10.1016/j.icarus.2020.113664.
989 Hirtzig, M., et al. (2013). Titan's surface and atmosphere from Cassini/VIMS data with updated
990 methane opacity. Icarus, 226, 470–486.
991 Jacquinet-Husson, N., Crepeau, L., Armante, R., Boutammine, C., Chedin, A., Scott, N. A., et al.
992 (2011). The 2009 edition of the GEISA spec- troscopic database. Journal of Quantitative
993 Spectroscopy and Radiation Transfer, 112, 2395–2445.
994 Janssen, M.A., Lorenz, R.D., West, R., Paganelli, F., Lopes, R.M., Kirk, R.L., Elachi, C., Wall,
995 S.D., Johnson, W.T.K., Anderson, Y., Boehmer, R.A., Callahan, P., Gim, Y., Hamilton, G.A.,
996 Kelleher, K.D., Roth, L., Stiles, B., Le Gall, A., Cassini RADAR Team, (2009). Titan's Surface
997 at 2.2-cm wavelength imaged by the Cassini RDAR radiometer: Calibration and first results.
998 Icarus 200, 222-239. doi: 10.1016/j.icarus.2008.10.017.
999 Janssen, M. A., Le Gall, A., Lopes, R. M., Lorenz, R. D., Malaska, M. J., Hayes, A. G., et al.
1000 (2016). Titan's surface at 2.18-cm wavelength imaged by the Cassini RADAR radiometer:
1001 Results and interpretations through the first ten years of observation. Icarus, 270, 443–459.
1002 Jaumann, R., Brown, R.H., Stephan, K., Barnes, J.W., Soderblom, L.A., Sotin, C., Le Mouélic, S.,
1003 Clark, R.N., Soderblom, J., Buratti, B.J., Wagner, R., McCord, T.B., Rodriguez, S., Baines,
1004 K.H., Cruikshank, D.P., Nicholson, P.D., Griffith, C.A., Langhans, M., Lorenz, R.D., (2008).
1005 Fluvial erosion and post-erosional processes on Titan. Icarus 197, 526-538. doi:
1006 10.1016/j.icarus.2008.06.002.

Jaumann, R., Kirk, R. L. Lorenz, R. D., Lopes, R. M.C., Stofan, E. Turtle, E. P. Keller, H. U. Wood, C. A., Sotin, C. Soderblom, L. A., Tomasko, M. G., (2009). Geology and Surface Processes on Titan. In: Brown, R. H., Leberton, J.-P., Waite, J. H. (Eds.), Titan from Cassini-Huygens. Springer, New York, pp 75–140.

Karkoschka, E., Tomasko, M.G., (2010). Methane absorption coefficients for the jovian planets from laboratory, Huygens, and HST data. Icarus 205, 674–694.

Karkoschka, E. et al., 2012. The reflectivity spectrum and opposition effect of Titan's surface observed by Huygens' DISR spectrometers. Planet. Space Sci. 60, 342–355.

Krasnopolsky, V.A., 2009. A photochemical model of Titan's atmosphere and ionosphere. Icarus 201, 226-256. doi: 10.1016/j.icarus.2008.12.038.

Lafferty, W., Solodov, A., Weber, A., Olson, B., Hartmann, J-M., (1996). Infrared collision-induced absorption by N2 near 4.3 μm for atmospheric applications: measurements and empirical modeling. Applied Optics 35, 5911-5917.

Langhans, M.H., Jaumann, R., Stephan, K., Brown, R.., Buratti, B.J., Clark, R.N., Baines, K.H., Nicholson, P.D., Lorenz, R.D., Soderblom, L.A., Soderblom, J.M., Sotin, C., Barnes, J.W., Nelson, R., 2012. Titan's fluvial valleys: Morphology, distribution, and spectral properties. Planetary and Space Science 60, 34-51. doi: 10.1016/j.pss.2011.01.020.

Lavvas, P.P., Coustenis, A., Vardavas, I.M., (2008). Coupling photochemistry with haze formation in Titan's atmosphere, Part II: Results and validation with Cassini/Huygens data. Planetary and Space Science 56, 67-99. doi: 10.1016/j.psss.2007.05.027.

Le Gall, M.J. Malaska, R.D. Lorenz, M.A. Janssen, T. Tokano, A.G. Hayes, M. Mastrogiuseppe, J.I. Lu- nine, G. Veyssière, P. Encrenaz, O. Karatekin, (2016). Composition, seasonal change and bathymetry of Ligeia Mare, Titan, derived from its microwave thermal emission. J. Geophys. Res., Planets 121, 233–251.

Lellouch, E., Schmitt, B., Coustenis, A., Cuby, J. G., (2004). Titan's 5-micron lightcurve. Icarus, 168, 1, 209-214.

Le Mouélic, S., (2019). The Cassini VIMS archive of Titan: From browse products to global infrared color maps. Icarus, 319, 121-132.

Lopes, R.M.C., Stofan, E.R., Pecyno, R., Radebaugh, J., Mitchell, K.L., Mitri, G., Wood, C.A., Kirk, R.L., Wall, S.D., Lunine, J.L., Hayes, A., Lorenz, R., Farr, T., Wye, L., Craig, J., Ollerenshaw, R., Janssen, M., LeGall, A., Paganelli, F., West, R., Stiles, B., Callahan, P., Anderson, Y., Valora, P., Soderblom, L., and the Cassini RADAR Team, (2010). Distribution and interplay of geologic processes on Titan from Cassini radar data. Icarus 205, 540–558. doi: 10.1016/j.icarus.2009.08.010.

Lopes, R.M.C., Kirk, R.L.; Mitchell, K.L., Le Gall, A., Barnes, J.W., hayes, A., Kargel, J., Wye, L., Radebaugh, J., Stofan, E.R., Janssen, M., Neish, C., Wall, S., Wood, C.A., Lunine, J.I., Malaska, M.J., 2013. Cryovolcanism on Titan: New results from Cassini RADAR and VIMS. Journal of Geophysical Research: Planets 118, 1-20. doi: 10.1002/jgre.20062.

Lopes, R.M.C., Malaska, M.J., Solomonidou, A., LeGall, A., Janssen, M.A., Neish, C., Turtle, E.P., Birch, S.P.D., Hayes, A.G., Radebaugh, J., Coustenis, A., Schoenfeld, A., Stiles, B.W., Kirk, R.L., Mitchell, K.L., Stofan, E.R., Lawrence, K.J., and the Cassini RADAR Team (2016). Nature, Distribution, and Origin of Titan's Undifferentiated Plains ("Blandlands"). Icarus, 270, 162-182.

Lopes, R.M.C., Wall, S.D., Elachi, C. et al. (2019). Titan as Revealed by the Cassini Radar. Space Science Review, 215, 33.

Lopes, R.M.C., M.J. Malaska, A. M. Schoenfeld, A. Solomonidou, S.P.D. Birch, M. Florence, A.G. Hayes, D.A. Williams, J. Radebaugh, T. Verlander, E.P. Turtle, A. Le Gall, S. Wall, and the Cassini RADAR Team, (2020). A Global Geomorphologic Map of Saturn's Moon Titan. Nature Astronomy, 4, 228-233.

Lora, J. M. and Ádámkovics, M. (2017). The near-surface methane humidity on Titan. Icarus 286, 270–279.

Lorenz, R.D., Wall, S., Radebaugh, J., Boubin, G., Reffet, E., Janssen, M., Stofan, E., Lopes, R., Kirk, R., Elachi, C., Lunine, J., Mitchell, K., Paganelli, F., Soderblom, L., Wood, C., Wye, L., Zebker, H., Anderson, Y., Ostro, S., Allison, M., Boehmer, R., Callahan, P., Encrenaz, P., Ori, G.G., Francescitti, G., Gim, Y., Hamilton, G., Hensley, S., Johnson, W., Kelleher, K., Muhleman, D., Picardi, G., Posa, F., Roth, L., Seu, R., Shaffer, S., Stiles, B., Vetrella, S., Flamini, E., West, R., 2006. The Sand Seas of Titan: Cassini RADAR Observations of Longitudinal Dunes. Science 312, 724-727. doi: 10.1126/science.1123257.

Lorenz, R.D., et al. (2021). Selection and Characteristics of the Dragonfly Landing Site near Selk Crater, Titan. The Planetary Science Journal, 2, 24, 13.

MacKenzie, S., et al.: Planet. Sci J. 2, 112 (2021). https://doi.org/10.3847/PSJ/abf7c9

Malaska, M., Radebaugh, J., Le Gall, A., Mitchell, K., Lopes, R., Wall, S., (2011). High-volume meandering channels in titan's south polar region. 42nd Lunar and Planetary Science Conference, 1562.

Malaska, M. J., Lopes, R. M. C., Williams, D. A., Neish, C. D., Solomonidou, A., Soderblom, J. M., et al. (2016a). Geomorphological map of the Afekan Crater region, Titan: Terrain relationships in the equatorial and midlatitude regions. Icarus, 270, 130–161.

Malaska, M.J., Lopes, R.M., Hayes, A.G., Radebaugh, J., Lorenz, R., Turtle, E., 2016b. Material transport map of Titan: the fate of dunes. Icarus, 270, 183-196.

Malaska, M.J., Hodyss, R., Lunine, J.I., Hayes, A.G., Hofgartner, J.D., Hollyday, G., Lorenz, R.D., (2017). Laboratory measurements of nitrogen dissolution in Titan lake fluids. Icarus, 289, 94-105. doi: 10.1016/j.icarus.2017.01.033

Malaska, M. J., Radebaugh, J., Lopes, R. M. C., Mitchell, K., Verlander, T., Schoenfeld, A., Florence, M., Le Gall, A., Solomonidou, A., Hayes, A., Birch, S., Janssen, M., Schurmeier, L., Cornet, T., Ahrens, C., and the Cassini RADAR team, (2020). Labyrinth Terrain on Titan. Icarus, 344, 113764.

McCord, T.B., et al., (2004). Cassini VIMS observations of the Galilean satellites including the VIMS calibration procedure. Icarus, 172, 104-126.

McKellar, A. R. (1989). Low-temperature infrared absorption of gaseous N 2 and N2 + H2 in the 2.0-2.5 μm region: Application to the atmospheres of Titan and Triton. Icarus, 80, 361-369.

Miller, J.W., Birch, S.P.D., Hayes, A.G., Malaska, M.J., Lopes, R.M.C., Schoenfeld, A.M., Corlies, P.M., Burr, D.M., Farr, T.G., Perron, J.T., (2021).Fluvial Features on Titan and Earth: Lessons from Planform Images in Low-resolution SAR. The Planetary Science Journal, 2:142.

Mitchell, J.L., (2008). The drying of Titan's dunes: Titan's methane hydrology and its impact on atmospheric circulation. J. Geophys. Res. E Planets, 113, 1-22.

Mitri, G., Showman, A.P., Lunine, J.I. and Lopes, R.M., 2008. Resurfacing of Titan by ammonia-water cryomagma. Icarus, 196, 216-224.

Mitri, G., Bland, M.T., Showman, A.P., Radebaugh, J., Stiles, B., Lopes, R.M.C., Lunine, J.I., pappalardo, R.T., 2010. Mountains on Titan: Modeling and observations. Journal of Geophysical Research: Planets 115, E10002.

Moore, J.M., Howard, A.D., Morgan, A.M., 2014. The landscape of titan as witness to is climate evolution. Journal of Geophysical Research: Planets 119, 2060-2077. doi: 10.1002/2014JE004608.

Moroz, L.V., Arnold. G., Korochantsev, A.V., Wasch, R., (1998). Natural Solid Bitumens as Possible Analogs for Cometary and Asteroid Organics:. 1. Reflectance Spectroscopy of Pure Bitumens. Icarus, 134, 2, 253-268.

Nelson, R.M., Kamp. L.W., Lopes, R.M.C., Matson, D.L., Kirk, R.L., Hapke, B.W., Wall, S.D., Boryta, M.D., Leader, F.E., Smythe, W.D., Mitchell, K.L., Baines, K.H., Jaumann, R., Sotin, C., Clark, R.N., Cruikshank, D.P., Drossart, P., Lunine, J.I., Combes, M., Bellucci, G., Bibring, J-P., Capaccioni, F., Cerroni, P., Coradini, A., Formisano, V., Filacchione, G., Langevin, Y., McCord, T.B., Mennella, V., Nicholson, P.D., Sicardy, B., Irwin, P.G.J. (2009). Photometric Changes on Saturn's Moon Titan: Evidence for Cryovolcanism. Geophys. Res. Lett., 36, L04202, doi:10.1029/2008GL036206.

Neish, C.D., Barnes, J.W., Sotin, C., MacKenzie, S., Soderblom, J.M., Le Mouélic, S., Kirk, R.L., Stiles, B.W., Malaska, M.J., Le Gall, A., Brown, R.H., Baines, K.H., Buratti, B., Clark, R.N., Nicholson, P.D., (2015). Spectral properties of Titan's impact craters imply chemical weathering of its surface. Geophys. Res. Lett. 42, 3746–3754.

Niemann, H.B., Atreya, S.K., Demick, J., Gautier, D., Haverman, J., Harpold, D., Kasprzak, W., Lunine, J., Owen, T., Raulin, F. (2010). Composition of Titan's lower atmosphere and simple surface volatiles as measured by the Cassini-Huygens probe gas chromatograph mass spectrometer experiment. J. Geophys. Res., 115, E12006.

Nixon, R. Clark, R. Courtin, A. Hayes, R. Lopes, R. Yelle, C. Sotin, A. Rymer, R. Johnson, R. Lorenz, M. Mastrogiuseppe, H. Smith, D. Strobel, R. Achterberg, A. Buch, K. Mandt, D. Mitchell, F. Raulin, E. Turtle, L. Iess, V. Vuitton, A. Solomonidou, R. West, P. Coll, (2018). Titan's cold case files—outstanding questions after Cassini-Huygens. Planet. Space Sci. 155, 50–72.

Quirico, E., Schmitt, B., (1997). Near-Infrared Spectroscopy of Simple Hydrocarbons and Carbon Oxides Diluted in Solid N2 and as Pure Ices: Implications for Triton and Pluto. Icarus, 127, 354-378.

Patterson, G.W. et al., (2010). Global geological mapping of Ganymede. Icarus 207, 845–867. http://dx.doi.org/10.1016/j.icarus.2009.11.035.

Peck, E. R., and Khanna, B. N. (1966) JOSA, 56, 1059.

Poggiali, V., Mastrogiuseppe, M., Hayes, A., Seu, R., Birch, S., Lorenz, R., Grima, C., Hofgartner, J., (2016). Liquid-filled canyons on Titan. Geophysical Research Letter, 43, 7887-7894.

Radebaugh, J., Lorenz, R.D., Kirk, R.L., Lunine, J.I., Stofan, E.R., Lopes, R.M.C., Wall, S.D., 2007. Mountains on Titan as observed by Cassini Radar. Icarus 192, 77-91. doi: 10.1016/j.icarus.2007.026.020.

Radebaugh, J., Lorenz, R.D., Lunine, J.I., Wall, S.D., Boubin, G., Reffet, E., Kirk, R.L., Lopes, R.M., Stofan, E.R., Soderblom, L., Allison, M., Janssen, M., Paillouo, P., Callahan, P., Spencer, C., Cassini RADAR Team, 2008. Dunes on Titan observed by Cassini Radar. Icarus 194, 690-703. doi: 10.1016/j.icarus.2007.10.015.

Radebaugh, J., Ventra, D., Lorenz, R.D., Farr, T.G., Kirk, R.L., Hayes, A., Malaska, M.J., Birch, S., Liu, Z.Y.C., Lunine, J.I., Barnes, J., Le Gall, A., Lopes, R., Stofan, E., Wall, S., Pailloy, P. (2016). Alluvial and fluvial fans on Saturn's moon Titan reveal processes, materials and regional geology. Ventra, D. & Clarke, L. E. (eds) Geology and Geomorphology of Alluvial

and Fluvial Fans: Terrestrial and Planetary Perspectives. Geological Society, London, Special Publications, 440.
Rannou, P., Montmessin, F., Hourdin, F., Lebonnois, S., (2006). The latitudinal distribution of clouds on Titan. Science, 311, 201-205.
Rey, M., Nikitin, V., Bezard, B., Rannou, P., Coustenis, A., & Tyuterev, V. (2018). New accurate theoretical line lists of 12CH4 and 13CH4 in the 0–13400 cm 1 range: Application to the modeling of methane absorption in Titan's atmosphere. Icarus, 303, 114–130.
Rodriguez, S., et al. (2014). Global mapping and characterization of Titan's dune fields with Cassini: Correlation between RADAR and VIMS observations. Icarus 230, 168–179.
Rodriguez, S., et al. (2022). Science goals and new mission concepts for future exploration of Titan's atmosphere, geology and habitability: titan POlar scout/orbitEr and in situ lake lander and DrONe explorer (POSEIDON). Experimental Astronomy, https://doi.org/10.1007/s10686-021-09815-8.
Rothman, L. S., Gordon, I. E., Babikov, Y., Barbe, A., Chris Benner, D., Bernath, P. F., et al. (2013). The HITRAN2012 molecular spectroscopic database. Journal of Quantitative Spectroscopy and Radiation Transfer, 112, 2395–2445.
Schoenfeld, A., Lopes, R., Malaska, M., Solomonidou, A., Williams, D., Birch, S., Hayes, A., Corlies, P., Le Gall, A., Janssen, M., Le Mouelic, S., Turtle, E., Florence, M., Verlander, T., (2021). Geomorphological map of the South Belet Region of Titan. Icarus, 366, 114516.
Schoenfeld, A., Solomonidou, A., Malaska, M., Lopes, R., Birch, S., Mouelic, S., Florence, M., Verlander, T., Wall, S., Elachi, C. (2023). Geomorphological map of the Soi crater region on Titan. Journal of Geophysical Research: Planets, 128, e2022JE007499. https://doi.org/10.1029/2022JE007499.
Schurmeier, L.R., Dombard, A., (2018). Crater relaxation on Titan aided by low thermal conductivity sand infill. Icarus, 305, 314-323.
Seignovert, B., Le Mouelic, S., Brown, R.H., Karkoschka, E., Pasek, V., Sotin, C., Turtle, E.P. (2019). Titan's Global Map Combining Vims and Iss Mosaics. EPSC - European Planetary Science Congress 2019, Geneva, Switzerland, September 15-20, 2019, JPL Open Repository.
Smith, P. H., et al. (2005). Results from the Descent Imager/Spectral Radiometer (DISR) experiment on the Huygens entry probe of Titan. Nature, 438(7069), 779-784.
Soderblom, L.A. et al., (2007). Correlations between Cassini VIMS spectra and RADAR SAR images: Implications for Titan's surface composition and the character of the Huygens Probe Landing Site. Planet. Space Sci. 55, 2025–2036.
Sohl, F. et al., (2014). Tidal stresses on Titan and implications for its geology and habitability. J. Geophys. Res. 119, 1013–1036.
Solomonidou, A., G. Bampasidis, M. Hirtzig, A. Coustenis, K. Kyriakopoulos, K. Seymour, E. Brastolis, and X. Moussas (2013), Morphotectonic features on Titan and their possible origin, Planet. Space Sci., 77, 104–117.
Solomonidou, A., Hirtzig, M., Coustenis, A., Bratsolis, E., Le Mouélic, S., Rodriguez, S., et al. (2014). Surface albedo spectral properties of geologically interesting areas on Titan. Journal of Geophysical Research: Planets, 119, 1729–1747.
Solomonidou, A., Coustenis, A., Hirtzig, M., Rodriguez, S., Stephan, K., Lopes, R. M. C., et al. (2016). Temporal variations of Titan's surface with Cassini/VIMS. Icarus, 270, 85–99.
Solomonidou, A., A. Coustenis, R. Lopes, M. Malaska, S. Rodriguez, P. Drossart, C. Elachi, B. Schmitt, M. Janssen, M. Hirtzig, S. Wall, C. Sotin, K. Lawrence, N. Altobelli, N. Bratsolis, J. Radebaugh, K. Stephan, R. Brown, S. Le Mouélic, A. Le Gall, E.V. Villanueva, J.F. Brossier,

A.A. Bloom, O. Witasse, C. Matsoukas and A., Schoenfeld (2018). The Spectral Nature of Titan's Major Geomorphological Units: Constraints on Surface Composition. J. Geophys. Res, 123, 2, 489-507.

Solomonidou, A., Neish, C., Coustenis, A., Malaska, M., Le Gall, A., Lopes, R., Werynski, A., Markonis, Y., Lawrence, K., Altobelli, N., Witasse, O., Schoenfeld, A., Matsoukas, C., Baziotis, I., Drossart, P., (2020a). The chemical composition of impact craters on Titan I. Implications for exogenic processing. Astronomy & Astrophysics, 641, A16.

Solomonidou, A., Le Gall, A., Malaska, M., Birch, S., Lopes, R., Coustenis, A., Rodriguez, S., et al. (2020b). Spectral and emissivity analysis of the raised ramparts around Titan's northern lakes. Icarus, 344, 113338.

Solomonidou, A., Coustenis, A., Lopes, R., Malaska, M., Le Gall, A., Schmitt, B., Schoenfeld, A., Wall, S., Lawrence, K., Sotin, C., Matsoukas, C., Markonis, I., Drossart, P., Elachi, C., (2022). Chemical composition analysis of Titan's equatorial and midlatitude surface regions. Europlanet Science Congress 2022.

Stofan, E.R., Elachi, C., Lunine, J.I., Lorenz, R.D., Stiles, B., Mitchell, K.L., Ostro, S., Soderblom, L., Wood, C., Zebker, H., Wall, S., Janssen, M., Kirk, R., Lopes, R., Paganelli, F., Radebaugh, J., Wye, L., Anderson, Y., Allison, M., Boehmer, R., Callahan, P., Encrenaz, P., Flamini, E., Francescetti, G., Gim, Y., Hamilton, G., Hensley, S., Johnson, W.T.K., Kelleher, K., Muhlman, D., Paillou, P., Picardi, G., Posa, F., Roth, Seu, R., Shaffer, S., Vetrella, S., West, R., 2007. The lakes of Titan. Nature 445, 61-64. doi: 10.1038/nature05438.

Sulaiman, A., et al. (2021). Enceladus and Titan: emerging wolds of the Solar System. Experimental Astronomy, https://doi.org/10.1007/s10686-021-09810-z.

Tobie, G., et al. (2014). Science goals and mission concept for the future exploration of Titan and Enceladus. Planetary and Space Science. 104, 59–77.

Tokano, T., (2005). Meteorological assessment of the surface temperatures on Titan: constraints on the surface type. Icarus, 173, 222-242.

Tomasko, M. G., Doose, L., Engel, S., Dafoe, L. E., West, R., Lemmon, M., et al. (2008). A model of Titan's aerosols based on measurements made inside the atmosphere. Planetary and Space Science, 56, 669–707.

Wall, S.D., Lopes, R.M., Stofan, E.R., Wood, C.A., Radebaugh, J.L., Hörst, S.M., Stiles, B.W., Nelson, R.M., Kamp, L.W., Janssen, M.A. and Lorenz, R.D., 2009. Cassini RADAR images at Hotei Arcus and western Xanadu, Titan: Evidence for geologically recent cryovolcanic activity. Geophysical Research Letters, 36.

Weber, M.J., (2003). Handbook of Optical Materials. CRC Press, Boca Raton, Florida.

Werynski, A., Neish, C.D., Le Gall, A., Janssen, M.A., The Cassini RADAR Team, (2019). Compositional variations of Titan's impact craters indicates active surface erosion. Icarus, 321, 508-521.

Williams, D.A., Radebaugh, J., Lopes, R.M.C., Stofan, E., 2011. Geomorphologic mapping of the Menrva region of Titan using *Cassini* RADAR data. Icarus 212, 744-750. doi: 10.1016/j.icarus.2011.01.014.

Williams, D.A., Yingst, R.A., Garry, W.B., 2014. Introduction: The geologic mapping of Vesta. Icarus 244, 1–12. http://dx.doi.org/10.1016/j.icarus.2014.03.001.

Wilson, E.H., Atreya, S.K., 2004. Current state of modeling the photochemistry of Titan's mutually dependent atmosphere and ionosphere. Journal of Geophysical Research 109, E06002. doi: 10.1029/2003JE002181.

Wood, C.A., Lorenz, R., Kirk, R., Lopes, R., Mitchell, K., Stofan, E., and the Cassini RADAR Team, (2010). Impact craters on Titan. Icarus, 206 (2010) 334-344.
Wood, C.A. and Radebaugh, J., 2020. Morphologic evidence for volcanic craters near Titan's north polar region. Journal of Geophysical Research: Planets, 125(8), p.e2019JE006036.

Appendix

Table 3. Compositional constraints of the various units (261 locations) within the Soi crater region. The various locations are shown in Figure 4. The mixtures are given by percentages of different constituents (H_2O, CH_4, tholins, and dark organic material). HC_3N, CO_2, NH_3 ices were not detected in these locations. Spectra in full resolution for all presented constituents can be found in Figure 3.

Items	Location	Unit	Dark	H_2O ice	Tholins %	CH_4 %
1.	8	***pul***	40	10	45	5
2.	8b	*pul*	60	-	40	-
3.	14	*pul*	60	-	45	-
4.	24b	*pul*	20	30	40	10
5.	29	*pul*	-	40	40	20
6.	41	*pul*	-	50	25	25
7.	44	*pul*	50	30	10	10
8.	52	*pul*	-	20	80	-
9.	53b	*pul*	-	25	60	15
10.	55b	*pul*	35	15	30	20
11.	56	*pul*	-	25	60	15
12.	58b	*pul*	-	45	35	10
13.	63	*pul*	-	50	40	10
14.	73c	*pul*	20	25	40	15
15.	79	*pul*	-	25	60	15
16.	80b	*pul*	-	40	60	-
17.	98b	*pul*	-	45	35	20
18.	101	*pul*	-	45	50	5
19.	101b	*pul*	-	45	50	5
20.	102b	*pul*	-	50	45	5
21.	105	*pul*	-	40	55	5
22.	106	*pul*	-	30	65	5
23.	108c	*pul*	-	30	50	20
24.	A3	*pul*	50	25	15	10
25.	A4	*pul*	65	20	10	5
26.	A6	*pul*	60	35	-	5
27.	A13	*pul*	60	30	-	10
28.	A13c	*pul*	60	30	-	10
29.	A18b	*pul*	-	35	50	15
30.	A20	*pul*	-	50	30	20
31.	A22	*pul*	-	30	50	20
32.	6b	***pfv***	60	15	25	-
33.	8c	*pfv*	50	-	45	5
34.	9c	*pfv*	40	-	55	5
35.	10	*pfv*	35	10	50	5
36.	10c	*pfv*	60	-	40	-
37.	11b	*pfv*	60	25	15	-
38.	12	*pfv*	60	-	40	-
39.	21	*pfv*	-	25	65	10
40.	22b	*pfv*	35	-	50	10
41.	23	*pfv*	70	20	-	10
42.	27b	*pfv*	40	-	60	-
43.	34	*pfv*	45	30	10	15
44.	35	*pfv*	5	25	55	15
45.	35b	*pfv*	5	25	55	15
46.	44b	*pfv*	15	40	30	15
47.	53c	*pfv*	15	30	40	15
48.	56b	*pfv*	-	45	40	15
49.	58c	*pfv*	-	45	35	10
50.	60	*pfv*	-	55	45	-
51.	60b	*pfv*	-	55	45	-
52.	67	*pfv*	75	-	25	-
53.	70	*pfv*	60	25	10	5
54.	73	*pfv*	-	50	50	-
55.	75	*pfv*	-	40	60	-
56.	75b	*pfv*	-	40	60	-

57.	77b	*pfv*	50	30	20	-
58.	79b	*pfv*	-	25	60	15
59.	97	*pfv*	50	30	-	20
60.	104	*pfv*	-	60	35	5
61.	107	*pfv*	-	40	50	10
62.	108	*pfv*	-	40	40	20
63.	109b	*pfv*	-	40	40	20
64.	110	*pfv*	-	35	60	5
65.	A2b	*pfv*	60	35	-	5
66.	A13b	*pfv*	-	30	60	10
67.	A18	*pfv*	35	-	50	15
68.	A19b	*pfv*	-	55	45	-
69.	A36	*pfv*	-	25	70	5
70.	A41	*pfv*	-	30	65	5
71.	A53	*pfv*	-	30	65	5
72.	43	***psv***	45	30	10	15
73.	43b	*psv*	45	30	10	15
74.	47	*psv*	40	25	15	20
75.	81	*psv*	35	25	20	20
76.	87	*psv*	40	20	20	20
77.	87b	*psv*	40	25	20	15
78.	50	***pil***	-	25	55	20
79.	82	*pil*	45	30	15	10
80.	84b	*pil*	20	25	35	20
81.	94	*pil*	30	25	25	20
82.	94b	*pil*	25	25	30	20
83.	95	*pil*	55	25	-	20
84.	96	*pil*	50	30	5	15
85.	97b	*pil*	50	30	5	15
86.	98	*pil*	-	45	35	20
87.	98c	*pil*	-	45	35	20
88.	55	***psh***	35	15	30	20
89.	61	*psh*	-	50	50	-
90.	80	*psh*	-	40	60	-
91.	100	*psh*	-	35	55	10
92.	77	***pgh***	55	20	25	-
93.	78	*pgh*	55	20	25	-
94.	A10b	*pgh*	55	20	25	-
95.	4	***pu***	40	5	50	5
96.	5	*pu*	30	10	55	5
97.	7	*pu*	45	5	45	5
98.	30b	*pu*	5	30	40	25
99.	31b	*pu*	5	30	40	25
100.	33	*pu*	10	25	40	25
101.	36	*pu*	-	30	45	25
102.	36b	*pu*	-	30	45	25
103.	39b	*pu*	25	65	-	10
104.	40	*pu*	-	40	45	15
105.	40b	*pu*	-	40	45	15
106.	41c	*pu*	-	45	30	25
107.	42	*pu*	35	35	-	30
108.	45	*pu*	10	40	30	20
109.	45b	*pu*	-	20	60	20
110.	46	*pu*	30	25	30	15
111.	46b	*pu*	40	15	30	15
112.	48	*pu*	-	20	60	20
113.	57	*pu*	-	35	60	5

114.	59	*pu*	-	45	40	15
115.	62	*pu*	-	35	40	25
116.	64	*pu*	-	35	40	25
117.	65	*pu*	-	50	35	15
118.	72	*pu*	-	35	55	10
119.	74	*pu*	-	40	55	5
120.	76	*pu*	-	40	35	25
121.	89	*pu*	-	40	55	5
122.	90	*pu*	-	50	50	-
123.	90b	*pu*	-	40	55	5
124.	91	*pu*	-	25	60	15
125.	93	*pu*	-	35	60	5
126.	99b	*pu*	-	60	30	10
127.	106b	*pu*	-	30	65	5
128.	111	*pu*	-	35	60	5
129.	A10	*pu*	40	-	50	10
130.	30	***pdu***	25	40	25	10
131.	31	*pdu*	25	35	30	10
132.	32	*pdu*	15	35	35	15
133.	32b	*pdu*	15	40	30	15
134.	33b	*pdu*	15	40	30	15
135.	37	*pdu*	15	40	40	5
136.	37b	*pdu*	10	45	40	5
137.	38	*pdu*	25	40	20	15
138.	38b	*pdu*	25	40	20	15
139.	39	*pdu*	-	65	25	10
140.	42b	*pdu*	40	25	20	15
141.	48b	*pdu*	40	25	20	15
142.	49	*pdu*	35	25	25	15
143.	49b	*pdu*	30	25	30	15
144.	104b	*pdu*	-	60	35	5
145.	A15	*pdu*	-	50	40	10
146.	A15b	*pdu*	-	50	40	10
147.	A19c	*pdu*	-	55	45	-
148.	9b	***ds***	60	25	-	15
149.	19c	*ds*	60	25	-	15
150.	21b	*ds*	10	20	60	10
151.	22	*ds*	10	20	55	15
152.	24	*ds*	50	30	-	20
153.	25	*ds*	60	25	-	15
154.	27	*ds*	65	35	-	-
155.	51	*ds*	60	-	30	10
156.	54	*ds*	70	-	30	-
157.	A5	*ds*	10	30	60	-
158.	A19	*ds*	-	45	55	-
159.	A31	*ds*	-	25	60	15
160.	A39	*ds*	-	25	65	10
161.	A40	*ds*	10	25	60	5
162.	A47	*ds*	-	35	60	5
163.	A48	*ds*	-	35	65	-
164.	A49	*ds*	-	35	65	-
165.	6	***dl***	65	5	30	-
166.	9	*dl*	75	5	20	-
167.	10b	*dl*	80	-	20	-
168.	11	*dl*	85	5	10	-
169.	13	*dl*	75	-	25	-
170.	15	*dl*	75	-	25	-

171.	23b	*dl*	65	-	35	-
172.	28	*dl*	45	30	15	10
173.	66	*dl*	75	-	25	-
174.	A1	*dl*	85	-	10	5
175.	A2	*dl*	80	15	-	5
176.	A9	*dl*	70	-	25	5
177.	A12	*dl*	60	15	20	5
178.	A21b	*dl*	35	20	25	20
179.	A27	*dl*	40	25	25	10
180.	A28	*dl*	40	20	35	5
181.	A34	*dl*	-	35	60	5
182.	A44	*dl*	-	30	65	5
183.	A46	*dl*	-	30	65	5
184.	A52	*dl*	-	35	65	-
185.	1	***du***	70	5	20	5
186.	23e	*du*	65	-	30	5
187.	26	*du*	60	-	35	5
188.	57b	*du*	60	-	30	10
189.	A7	*du*	70	10	20	-
190.	A13d	*du*	70	15	25	-
191.	9d	***hm***	50	30	20	-
192.	19b	*hm*	40	-	45	15
193.	41b	*hm*	-	50	25	25
194.	58	*hm*	-	35	45	10
195.	77c	*hm*	50	30	20	-
196.	103b	*hm*	-	45	50	5
197.	15c	***hh***	45	-	55	-
198.	16	*hh*	-	40	60	-
199.	17	*hh*	-	25	60	15
200.	17b	*hh*	-	25	60	15
201.	17c	*hh*	-	20	65	15
202.	23d	*hh*	40	-	60	-
203.	53	*hh*	60	-	40	-
204.	68	*hh*	55	20	20	5
205.	71	*hh*	70	30	-	-
206.	73b	*hh*	40	20	25	15
207.	83	*hh*	40	25	20	15
208.	102	*hh*	-	45	50	5
209.	103	*hh*	-	50	45	5
210.	109	*hh*	-	50	20	30
211.	A11	*hh*	20	20	55	5
212.	A14	*hh*	15	40	45	-
213.	A32	*hh*	-	25	65	10
214.	A33	*hh*	-	25	60	15
215.	A20b	*hh*	-	45	35	20
216.	A21	*hh*	25	25	35	15
217.	A24	*hh*	-	25	65	10
218.	A25	*hh*	-	25	60	15
219.	A37	*hh*	-	30	65	5
220.	A38	*hh*	-	30	65	5
221.	A50	*hh*	-	40	60	
222.	A51	*hh*	-	30	60	10
223.	A54	*hh*	-	30	65	5
224.	A55	*hh*	-	35	60	5
225.	2	***hu***	10	25	60	5
226.	3	*hu*	50	15	35	-
227.	18	*hu*	40	-	45	15

228.	18b	*hu*	40	-	45	15
229.	19	*hu*	-	25	65	10
230.	20	*hu*	40	-	45	15
231.	64b	*hu*	-	65	35	-
232.	92	*hu*	-	65	35	-
233.	99	*hu*	-	65	20	15
234.	99c	*hu*	-	65	20	15
235.	108b	*hu*	-	40	40	20
236.	A8	*hu*	55	-	45	-
237.	A16	*hu*	-	40	60	-
238.	A17	*hu*	-	35	65	-
239.	15b	***hph***	45	-	55	-
240.	A23	*hph*	-	25	60	15
241.	A26	*hph*	-	30	65	5
242.	A29	*hph*	-	25	65	10
243.	A30	*hph*	-	30	65	5
244.	A35	*hph*	-	30	65	5
245.	A42	*hph*	-	35	60	5
246.	A43	*hph*	-	35	60	5
247.	A45	*hph*	-	35	65	-
248.	*114*	***lbf***	20	25	40	15
249.	*114b*	*lbf*	20	25	40	15
250.	23c	***ceh***	70	-	30	-
251.	52b	*ceh*		20	80	-
252.	69	*ceh*	70	-	30	-
253.	52c	***crh***		20	80	-
254.	112	*crh*	-	20	80	-
255.	88	***cf3***	70	15	15	-
256.	84	***bse***	45	35	-	20
257.	85	*bse*	35	30	20	15
258.	86	*bse*	35	30	20	15
259.	*113*	*bse*	25	20	35	20
260.	*115*	***brh***	20	25	40	15
261.	*116*	*brh*	40	25	20	15

1244

Detailed chemical composition analysis of the Soi crater region on Titan

A. Solomonidou[1,2], M. J. Malaska[3], R. M. C. Lopes[3], A. Coustenis[2], A. M. Schoenfeld[4], B. Schmitt[5], S. P. D. Birch[6], A. Le Gall[7, 8], K. Lawrence[3], C. Matsoukas[9], S. D. Wall[10], C. Elachi[10]

[1]Hellenic Space Center, Athens, Greece.

[2]LESIA–Observatoire de Paris, CNRS, UPMC Univ. Paris 06, Univ. Paris-Diderot, Meudon, France.

[3]Jet Propulsion Laboratory, California Institute of Technology, Pasadena, CA, USA.

[4]Department of Earth, Planetary, and Space Sciences, University of California Los Angeles, Los Angeles, CA, USA.

[5]Institut de Planétologie et d'Astrophysique de Grenoble, Université Grenoble Alpes, CNRS, Grenoble, France.

[6]Department of Earth, Atmospheric, and Planetary Science, Massachusetts Institute of Technology, Cambridge, MA, USA.

[7]Institut LATMOS/IPSL, UVSQ Université Paris-Saclay, Sorbonne Université, CNRS, France.

[8]Institut Universitaire de France, Paris, France.

[9]KTH-Royal Institute of Technology, Stockholm, Sweden.

[10]California Institute of Technology, Pasadena, CA, USA.

Corresponding author: Anezina Solomonidou (anezina.solomonidou@hsc.gov.gr), 178 Kifissias Avenue, Athens 15231, Greece

Highlights:

- Titan's compositional evolution cycle includes aeolian transport and leaching.
- Areas around latitude 35ºN are dominated by tholin and ice-like spectral signatures
- The midlatitudes are composed of end-stage materials that were subjected to rainfall.
- Empty lakes at the midlatitudes have same composition as the northern empty lakes.

Abstract

The Soi crater region (0º to 60ºN, 180ºW to -110ºW), which includes the well-preserved Soi crater in its center, spans a region from Titan's aeolian-dominated equatorial regions to fluvially-dominated high northern latitudes. This provides a rich diversity of landscapes, one that is also representative of the diversity encountered across Titan. Schoenfeld et al. (2023) mapped this region at 1:800,000 scale and produced a geomorphological map showing that the area consists of 22 types of geomorphological units. The Visual and Infrared Mapping Spectrometer (VIMS) coverage of the region enabled the detailed analysis of spectra of 261 different locations using a radiative transfer technique and a mixing model, yielding compositional constraints on Titan's optical surface layer. Additional constraints on composition on the near-surface substrate were obtained from microwave emissivity. We have derived combinations of top surface materials between dark materials, tholins, water-ice, and methane suggesting that dark mobile organic material at equatorial and high latitudes indicates "young" terrains and compositions, while tholin/water-ice mixtures that dominate areas around latitude 35ºN show a material that is older plains deposits that we interpret to be the end stage of aeolian and fluvial transport and deposition. We found no spectral evidence of CO_2, HC_3N, and NH_3 ice. We use the stratigraphic relations between the various mapping units and the relation between the geomorphology and the composition of the surface layers to build hypotheses on the origin and evolution of the regional geology. We suggest that sedimentary deposits, likely aeolian, are dominant in the region with fluvial activity and leaching changing the nature of the top surfaces of the midlatitude areas of the Soi crater region.

1 Introduction

The surface of Saturn's moon Titan has been revealed by the Cassini-Huygens spacecraft to be geologically complex with both exogenic and putative endogenic processes modifying its appearance. Titan's dense atmosphere and active methane cycle has enabled aeolian, fluvial, pluvial, and lacustrial processes, causing erosion and deposition. Few impact craters are seen, attesting that the surface is geologically young (e.g., Wood et al., 2010; Hedgepeth et al., 2020). Tectonism and possibly cryovolcanism have also contributed to surface modification (Jaumann et al., 2009; Mitri et al., 2008, 2010; Radebaugh et al., 2007; Lopes et al., 2013; 2019; Wall et al., 2009; Nelson et al., 2009; Solomonidou et al., 2013; 2016; Sohl et al., 2014; Wood and Radebaugh, 2020). The rich variety of geologic features on Titan and how the processes have dominated different latitudes have been discussed in previous works. For example, lakes and seas are present at high latitudes (e.g., Stofan et al., 2007; Bratsolis et al., 2012; Birch et al., 2016), while dunes of organic materials are concentrated at low latitudes (Lorenz et al., 2006; Radebaugh et al., 2008; Lopes et al., 2010; Rodriguez et al., 2014). Fluvial channel networks are present across large areas of the surface (Jaumann et al., 2008; Malaska et al., 2011; Langhans et al., 2012; Burr et al., 2013; Radebaugh et al., 2016; Miller et al., 2021), with a rich diversity in morphology (Burr et al., 2013; Miller et al., 2021), and are both liquid-filled (Poggiali et al., 2016) and dry. The mountainous and hummocky units represent remnants of an older crust, making them the oldest exposed unit on Titan, and they mostly appear in the equatorial zones and small areas all over the globe (Williams et al., 2011; Lopes et al., 2020a; Malaska et al., 2016a; 2020; Schoenfeld et al., 2021). Organic materials, produced by high-altitude photochemistry of methane and nitrogen in Titan's atmosphere, cover much of Titan's surface (Wilson and Atreya, 2004; Lavvas et al., 2008; Krasnopolsky, 2009; Clark et al., 2010; Solomonidou et al., 2018; 2020a). The buildup of these organic materials is evidenced by large standing dissected plateaux elevated by hundreds of meters

(Malaska et al., 2020). The midlatitudes of Titan are dominated by undifferentiated plains (Lopes et al., 2016; 2019; 2020) which are interpreted as being sedimentary in nature and likely formed by aeolian processes (Malaska et al., 2016b). Titan's latitudinal dependence for composition of the upper surface layer (Solomonidou et al., 2018), as well as patterns of wind deposition (Malaska et al., 2016b), show that, for both hemispheres, winds may transport material from both equatorial regions and high latitudes towards a zone at ~35º. That zone, at the midlatitudes may represent a 'sink', where materials are deposited as undifferentiated plains (Lopes et al., 2016; Malaska et al., 2016b; Solomonidou et al., 2020a).

The Soi crater region is scientifically valuable as it straddles the equatorial, midlatitude, and northern regions of Titan. The present study on the composition complements the geomorphological study of Schoenfeld et al. (2023). Our compositional map for this region is created using a radiative transfer code with Visual and Infrared Mapping Spectrometer (VIMS) data that help estimate the haze contribution to the data and extract surface information that are later matched to surface component mixture simulations (Hirtzig et al., 2013; Bonnefoy et al., 2016; Solomonidou et al., 2014; 2018; 2020a;b). The goal of this paper is to bring constraints on the formation and evolution of the selected area through the combination of the geomorphological and compositional maps of the Soi crater region. The maps will help reveal the types and extent of the geomorphologic units and the differences in nature of the top layers of the surface, and to infer the geological processes responsible for their formation and evolution. Our compositional mapping follows the methods described in Solomonidou et al. (2014; 2018; 2020a;b). Our efforts here are part of a global compositional mapping project that is currently in progress (Solomonidou et al., 2022), attempting to improve our knowledge of Titan's complex systems.

2 Geologic Setting

The Soi crater region was defined in Schoenfeld et al. (2023) as the area spanning from longitude 180º W to 110º W and from latitude 0 to 60ºN and the area contained in this region amounts to ~8×10^6 km^2 (~9.7% of Titan's surface). This region is geomorphologically mapped in detail and presented in the same article. For the production of the map by Schoenfeld et al. (2023) ~5.6% of the total surface area was mapped by using high resolution Synthetic Aperture Radar (SAR) data and the rest of the area was covered by non-SAR data (microwave emissivity, Imaging Science Subsystem -ISS, and VIMS), and mapped at lower resolution. For VIMS and the compositional mapping efforts, the area that was covered with data compatible and adequate to our radiative transfer modeling (detailed in section 3) spanned approximately 5.4×10^6 km^2, which corresponds to ~6.5% of Titan's total surface. The Soi crater region contains 22 distinct geomorphological units many of which were found in the Afekan (Malaska et al., 2016a) and South Belet regions (Schoenfeld et al., 2021).

The geomorphological map presented in Schoenfeld et al. (2023) used SAR and non-SAR datasets including altimetry, Radiometry-Emissivity, ISS, and VIMS (Fig. 1). All the different Cassini data used to create the geomorphological map of the Soi crater region (SAR, HiSAR, SARTopo and Digital Terrain Model, emissivity, VIMS, and ISS data) can be seen in Figure 2 of Schenfeld et al. (2023). The 22 geomorphological units identified include features of empty lakes, mountains, dunes, craters, labyrinth, and vast plains (Table 1). The Soi crater region is dominated by plains, matching the general trend around Titan's globe (see Lopes et al., 2020), followed by dunes, mountainous terrains, and finally very few craters and empty sharp-edged depressions

(SEDs) (Table 1). As for most of Titan, impacts have been erased by more recent geological processes, likely those that form dunes and plains.

Table 1. Terrain class, terrain units, terrain unit code found in the Soi crater region. Details, locations, and descriptions of the units are in Table 1 of Schoenfeld et al. (2023). The letter codes followed here are based on mapping efforts that have followed the general principles of previous Titan mapping and other planetary mapping efforts (Greeley and Batson, 1990; Greeley et al., 2000; Patterson et al., 2010; Williams et al., 2014; Lopes et al., 2016; 2020; Malaska et al., 2016; 2020; Schoenfeld et al., 2021; 2023).

Terrain class/ % of total area	**Terrain unit name and code**
Plains (73%)	Undifferentiated plains (*pul*)
	Variable plains (*pfv*)
	Scalloped plains (*psv*)
	Dark irregular plains (*pil*)
	Streak-like plains (*psh*)
	Bright gradational plains (*pgh*)
	Undivided plains (*pu*)
	Undivided dark plains (*pdu*)
Dunes (14%)	Featureless sand sheets (*ds*)
	Linear dunes (*dl*)
	Undivided dunes (*du*)
Mountains / Hummocky / Labyrinth (12%)	Mountain (*hm*)
	Hummocky (*hh*)
	Degraded hummocky (*hdm*)
	Pitted hummocky (*hph*)
	Finely dissected labyrinth (*lbf*)
	Undivided mountain chains/hummocky areas (*hu*)
Craters (<1%)	Crater rim (*crh*)
	Crater ejecta (*ceh*)
	Crater fill 3 (*cf3*)
Lakes (<1%)	Sharp-edged depression (*bse*)
	Ramparts (*brh*)

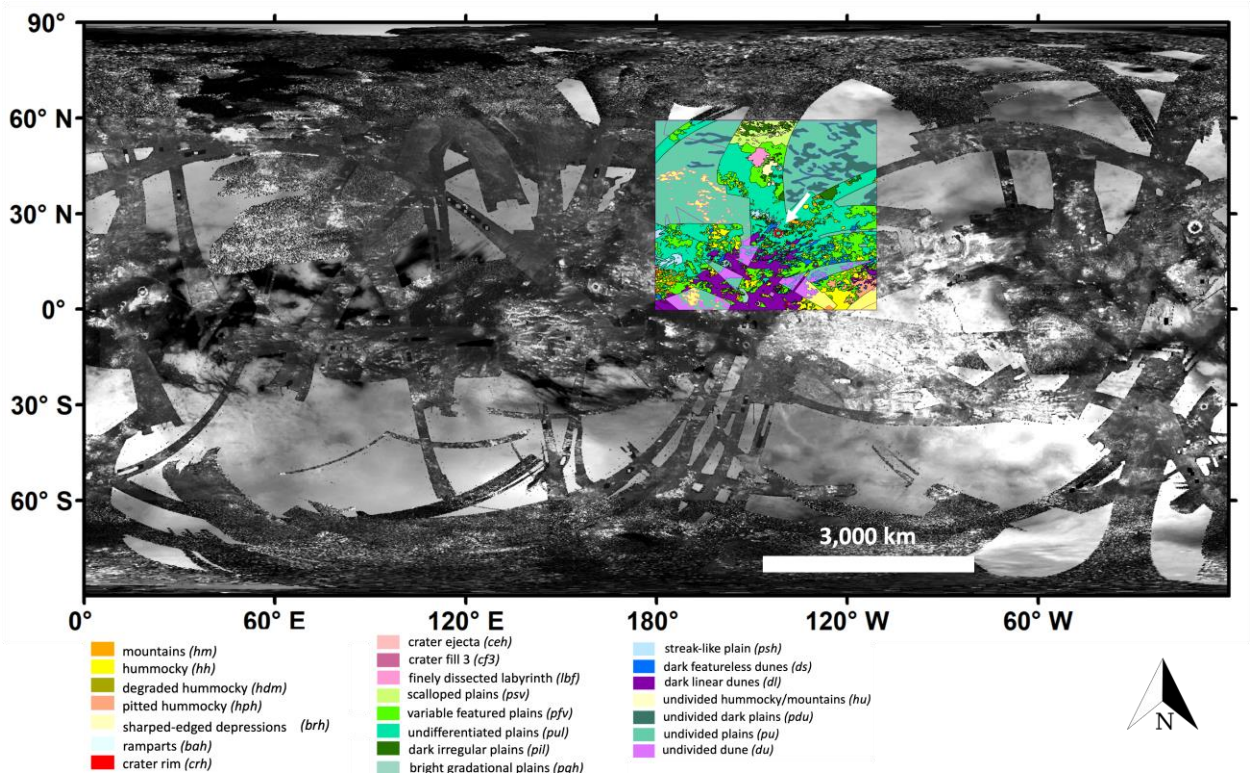

Figure 1. Geomorphological map of the Soi crater region (adapted from Schoenfeld et al., 2023) in global context. Geomorphological map for all SAR and non-SAR data at zero transparency (map layer fully opaque), same color scheme as the global geomorphological map of Titan in Lopes et al. (2020). The arrow points to the Soi crater. The background map is a global mosaic of Titan created from Imaging Science Subsystem (ISS) data (USGS Astrogeology Science Center).

3 Compositional mapping

Titan's surface composition remains, to this day, largely a mystery. Due to both atmospheric effects and spectral degeneracies, we have so far been prevented from making quantitative and accurate estimates of material concentrations within the numerous and varied geologic units on Titan's surface. This is a complex situation that can only be improved in a step-by-step approach in which every new constraint brings useful additional information, while waiting for new observations from ground-based facilities or *in situ* data from space missions like Dragonfly (e.g., Tobie et al., 2014; Lorenz et al., 2021; Barnes et al., 2021; Sulaiman et al., 2021; Rodriguez et al., 2022). There are, however, select windows through Titan's atmosphere in the near-infrared where the methane absorption is reduced (e.g., Barnes et al., 2005; Corlies et al., 2021). Due to Titan's complex atmosphere and processes therein, we apply a radiative transfer code to Cassini VIMS data in order to tackle as well as possible the issue of lingering methane absorption and scattering of atmospheric components.

For the chemical compositional mapping, we used methods that have been successfully used in the past on VIMS data (Bonnefoy et al., 2016; Lopes et al., 2016; Malaska et al., 2016a; Brossier et al., 2018; Solomonidou et al., 2014; 2016; 2018; 2020a;b), to account for the atmospheric contribution to the data and extract the actual surface information in the form of

albedo values and spectral responses. Further, similar to Solomonidou et al. (2018), where the first attempt of constraining the chemical composition of all major Titan geomorphological units was made, in addition to the compositional analysis of one specific unit, the impact craters (Solomonidou et al., 2020a), here we provide a compositional analysis of the entire Soi crater region in greater detail than in the previous efforts and for a significantly larger number of units and locations. Efforts to spectrally analyze Titan's vast areas and constrain their composition can be found in Nelson et al. (2006), McCord et al. (2006; 2008), Barnes et al. (2008), Brown et al. (2008), Clark et al. (2010), Soderblom et al. (2010), MacKenzie et al. (2014), Rodriguez et al. (2014), Brossier et al. (2018), Griffith et al. (2019), Coutelier et al. (2021) and others. All of these studies have analyzed VIMS data. Some of them have utilized radiative transfer codes (e.g., Coutelier et al., 2021) for their data analyses, while others have employed geophysical and remote sensing tools and methods such as Principal Component Analysis (PCA) (e.g., Griffith et al., 2019) and spectral ratios (e.g., Barnes et al., 2008). These methods are often employed to highlight differences between features and to reduce the effect of varying light reflectance intensities. In Coutelier et al. (2021), the radiative transfer code is utilized to factor in atmosphere scattering and absorption, thereby eliminating atmospheric effects and discrepancies caused by observational geometries. The ultimate outcome is the retrieval of atmospheric albedos across all atmospheric windows. Their findings underscore a significant observation, which is compatible to findings of this present work: the relationship between water ice and VIMS 'dark blue' and 'bright blue' areas is not as straightforward as previously believed (Barnes et al., 2007a, 2007b).

Our chemical composition map was created using the measurements of VIMS through our radiative transfer code (RT) and spectral deconvolution analysis. We recognize that the spectral analysis is only of the very thin optical layer (tens of microns) that covers the surface of Titan. To take into account the material below the optical covering, in our interpretations of the geological history of the area we also use the microwave emissivity measurements that probe the surface to greater depths (tens of centimeters). Microwave emissivity can be used to constrain the composition in depths that IR is unable to reach. Indeed, the radiometry provides a measure of the averaged emissivity of the near subsurface down to a depth that can be approximately defined as the electrical skin depth (Janseen et al., 2016). The sounding depth has been estimated based on the seasonal thermal signature in Janssen et al. (2009; 2016) and it is of the order of 40 cm - 1 m in the radar dark terrains, and to 200 m in liquid methane. This largely depends on the microwave transparency of the material, while the presence of high dielectric constant materials and/or volume scattering due to the presence of structures in the subsurface, are considered factors that decrease the emissivity values (Janssen et al., 2016).

3.1 Radiative Transfer Technique and Mixing Model

The compositional results are extracted through a series of analyses of VIMS data. We have analyzed 261 different locations from within the Soi crater region using 14 VIMS datacubes from 8 different Cassini flybys (Table 2; Figure 2). The selection of our 261 regions of interest (RoIs) was made after carefully examining the available VIMS datacubes compatible to our RT approximation and was based on the identification of pixels that thoroughly include different geomorphological units as described in Schoenfeld et al. (2013) in good resolution. We then used our RT code to extract surface albedos from the VIMS data (Hirtzig et al., 2013; Solomonidou et al., 2014;2016; 2018; 2020a;b).

Table 2. Selected Cassini/VIMS datacube observations including flybys, dates of acquisition, product IDs, and cube properties (angles of incidence *i*, emergence *e*, and phase α; spatial resolution res).

Flyby	Date	Selected pixels with numbers as shown in Fig. 2 and product IDs	Datacube Properties Geometry-Spatial Resolution (*i*,*e*,*α*,res/pxl)
Tb	12/2004	79-80: 1481629409	*i:* 52-53º, *e:* 15-17º, *α:* 36-37º, res: 03 km
T08	10/2005	A7-A31, A33, 98: 1509148649 50-58, 107-110: 1509149009 59-62, 72-75, 89-93: 1559085140	*i:* 30-57º, *e:* 09-46º, *α:* 23-24º, res: 46 km *i:* 34-60º, *e:* 26-42º, *α:* 22-23º, res: 45 km *i:* 49-60º, *e:* 26-42º, *α:* 25-26º, res: 39 km
T10	01/2006	1-6: 1516007480	*i:* 36-49º, *e:* 01-12º, *α:* 37-38º, res: 14 km
T12	03/2006	15-22: 1521407900 23-29, 111-112: 1521405451 A1-A6, A32, A34-A55: 1521402363	*i:* 29-37º, *e:* 34-55º, *α:* 65-66º, res: 15 km *i*: 45-57º, *e:* 19-38º, *α:* 64-65º, res: 38 km *i:* 54-59º, *e:* 11-41º, *α:* 63-64º, res: 23 km
T31	05/2007	63-66, 76, 99-106: 1559081653	*i:* 48-59º, *e:* 37-51º, *α:* 26-27º, res: 29 km
T77	06/2011	7-12, 14, 77-78b: 1687307753	*i*: 10-38º, *e*: 27-58º, *α:* 21-22º, res: 25 km
T97	01/2014	30-36, 96-97, 113-116: 1767303982 33b, 37-42: 1767303262 43-49, 81-88, 94-95: 1767301842	*i:* 33-49º, *e:* 10-28º, *α:* 51-54º, res: 10 km *i:* 43-60º, *e*: 08-30º, *α:* 52-53º, res: 12 km *i:* 32-44º, *e:* 11-22º, *α:* 55-56º, res: 16 km
T113	09/2015	13, 67-71: 1822165321	*i:* 37-59º, e: 02-09º, *α:* 57-58º, res: 14 km

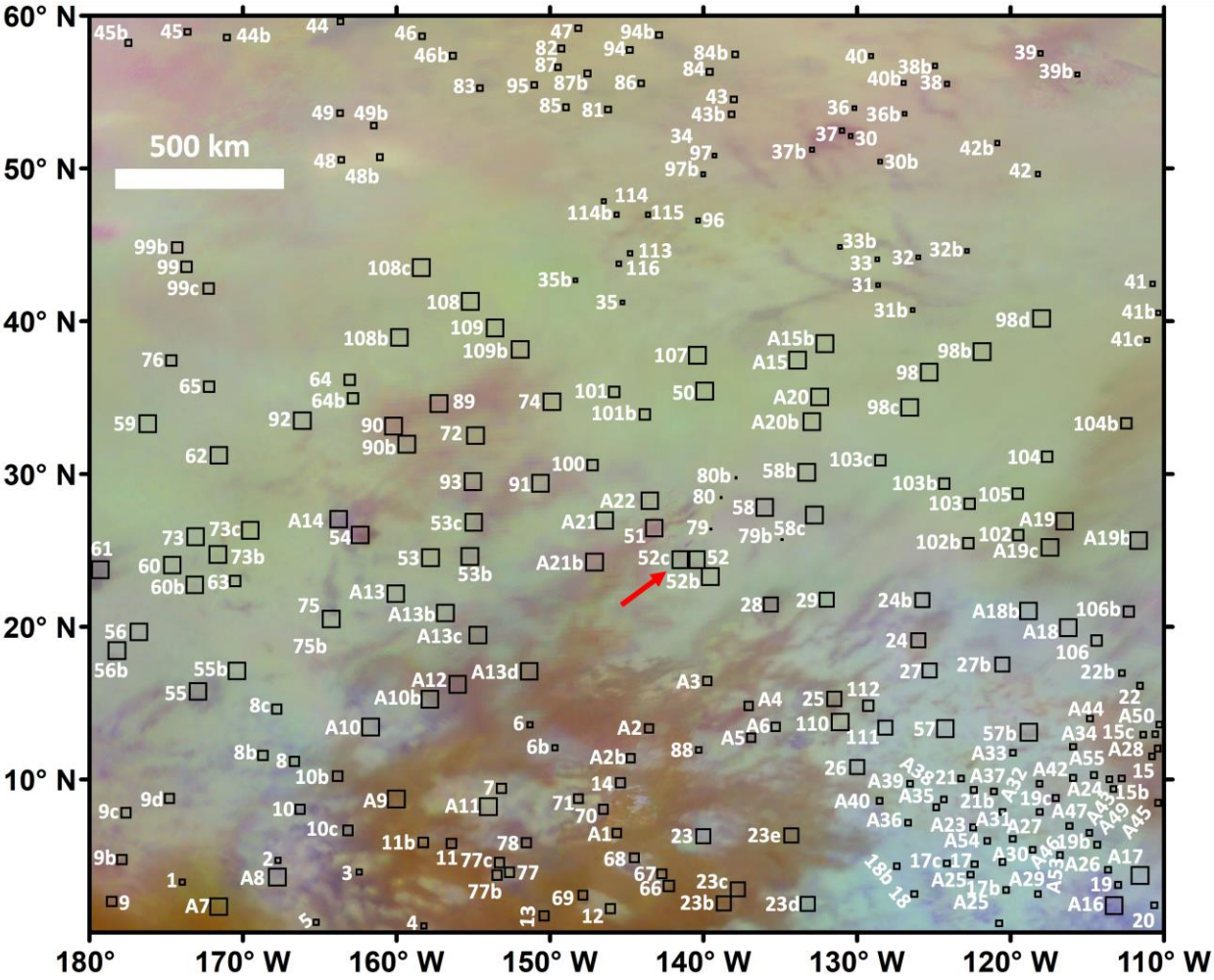

Figure 2. Regions of interest within the Soi crater region and pixel selections on VIMS for RT analysis from 261 different locations. The black squares correspond to the region of interest (RoI)

selected at each location based on their spatial resolution (see Table 2). The red arrow indicates the location of the Soi crater. North is at the top.

Our RT code (Hirtzig et al., 2013) is a plane-parallel code based on a Spherical Harmonic Discrete Ordinate Method solver (SHDOMPP) (Evans, 2007) that incorporates: (a) the vertical profiles of temperature and pressure provided by the Huygens Atmospheric Structure Instrument (HASI) (Fulchignoni et al., 2005); (b) the methane vertical mixing ratio from the Gas Chromatograph Mass Spectrometer (GCMS) (Niemann et al., 2010); (c) a uniform CO mole fraction equal to 4.5 x 10^{-5} based on Cassini/CIRS measurements (de Kok et al., 2007); (d) atmospheric opacity sources from aerosols and gases: Rayleigh scattering from N_2 and CH_4 (Peck and Khanna, 1966; Weber, 2003); collision-induced absorption by nitrogen (N_2) and hydrogen (H_2) (McKellar et al. (1989); Lafferty et al. (1996); lines for methane (Campargue et al., 2015; TheoReTS - Rey et al., 2018) and its isotopologues (e.g., $^{12}CH_4$, $^{13}CH_4$, $^{12}CH_3D$) (HITRAN2020 - Rothman et al., 2013; Gordon et al., 2022); lines for CO and C_2H_2 isotopologues (GEISA2009 - Jacquinet-Husson et al., 2011) with the use of correlated-*k* absorption coefficients as described in Hirtzig et al. (2013). Considering all components (a-d), the code analyses the VIMS data and produces simulations of the surface albedo with various haze opacities.

The results are then calibrated with respect to the albedo measurements derived by the Descent Imager Spectral Radiometer (DISR) at the Huygens landing site (HLS), which we use as a reference area and a calibration tool. Given that the haze extinction profile reference is adjusted to the measurements from DISR, the haze contribution to the VIMS data at the landing site of Huygens is defined as 100%. By iteration for the best possible fit, the code derives the haze contributions with an absolute accuracy of ±5% (Hirtzig et al., 2013). After estimating the haze population at all window wavelengths, the surface albedos are extracted at full spectral resolution and in weighted averages over each window's wavelength range (Tomasko et al., 2008; Hirtzig et al., 2013). In a weighted average, each data point value from within each of the 8 atmospheric windows is multiplied by an assigned weight, which is then summed and divided by the number of data points. For this reason, a weighted average can improve the data's accuracy. In this current analysis, we calculated single points of weighted averages of the surface albedo within the windows, with larger weights for channels with higher transmittance around the center. The spectral resolution (Full Width at Half Maximum, FWHM) is about 13 nm below 2.0 μm, increases up to 22 nm at 4.2 μm, and decreases to 18 nm at 4.8 μm (Brown et al., 2004). An example of weighted averages of the surface albedos in the atmospheric windows compared to the full resolution surface albedo spectrum in the 0.89–5.2 μm of the Visual and Infrared Mapping Spectrometer range can be found in Figure 5 of Solomonidou et al. (2018).

In our RT code and the extraction of surface albedos, we consider several uncertainties calculated and summed at the 3σ level including random errors due to noise in the data and due to propagation of haze retrieval errors, as well as systematic errors due to model, resulting from uncertainties due to the CH_4 far-wings opacity, the CH_4 linelist, the CH_4 vertical concentration profile, the aerosol phase function, the aerosol vertical distribution, and the aerosol forced single scattering albedo. All the details on the error estimation can be found in Section 3.3. in Hirtzig et al. (2013). In this current analysis we also take into account errors in the existing spectral line profiles, the haze extinction fit, the data intrinsic noise, which unlike random noise, is not random but arises from specific characteristics or imperfections in the sensor (McCord et al., 2004) and the phase function uncertainty. The surface albedos are then inverted with relative errors of 35%, 35%, 26%, 21%, 26%, 50%, 50%, and 43% for the 0.94, 1.08, 1.28, 1.58, 2.03, 2.69, 2.79, 5.00 μm windows, respectively. At the longer wavelengths of 2.69-5 μm, the uncertainties are larger

due to the lower signal to noise ratio (S/N). In any case, the error bars on the best fit of surface albedos take into account not only S/N limitations, but also errors due to uncertainties on the haze model (typical error on the extinction is 5%). Since the RT code adopts a plane-parallel and a Lambertian approximation and for the accuracy of the results, only VIMS data with geometry observations of both incidence and emergence angles <60º are selected, with only 15% of the data selected having incidence or emergence angles >50º (Table 2). We followed the approach used previously and in the recent study by Es-Sayeh et. al. (2023) where the authors use the RT code with the plane-parallel approximation used in this current analysis as well, and recommend the use of VIMS datacubes with incidence angles up to 50° incidence angle. The phase angle of all selected datacubes are higher than 10-15º and up to 70º and hence the surface behaves almost as Lambertian (Karkoschka et al., 2012). The effects of the phase angle on the I/F value are included in the error bars on our results (Karkoschka et al., 2012; Solomonidou et al., 2014). The spatial resolution of our selected datacubes ranges from 3 to 46 km/pixel (Table 2).

Finally, we use a linear mixing model, as in previous work (Solomonidou et al., 2018; 2020a), to place semi-quantitative constraints on the relative composition of Titan's surface. The model includes a selected spectral library of molecules, used as proxies for Titan candidate materials convoluted to VIMS spectral resolution, in order to examine the compositional properties of the various regions within the Soi crater region. While some of the specific molecules and complex carbonaceous materials included in our mixing model library are not expected to be found on Titan, we have used them to represent complex organic materials. Many of these materials are biogenic in origin, and through terrestrial diagenetic processes have become chemically aromatized and converted into complex refractory materials. The purpose of this exercise is not to imply exact chemical composition, but to constrain the relative types of molecular classes that could be present.

The Titan candidate materials include ices of ammonia (NH_3), carbon dioxide (CO_2), water (H_2O), cyanoacetylene (HC_3N), methane (CH_4), tholins, kerite, asphaltite, three different types of anthraxolites, and amorphous carbon (Quirico and Schmitt 1997; Grundy and Schmitt 1998; Grundy et al., 2002; Bernard et al., 2006; Brasse et al., 2015; GhoSST @ SSHADE database).

Tholins are laboratory-produced materials which may differ from the complex aerosols produced in Titan's atmosphere and later processed at the surface by fluvial/pluvial/aeolian activity. However, their spectral properties have been used in Titan's spectral analyses to simulate the atmospheric haze content.

We use 'methane' as a representative for any aliphatic hydrocarbon solid including alkanes, alkynes, and alkenes (e.g., Lora and Ádámkovics, 2017; Malaska et al., 2017; Faulk et al., 2017; 2020). These other solid aliphatic materials may be part of the compositional mix, however, these larger aliphatic materials will not be liquid since at Titan temperatures only methane, ethane, propane, and 1-butene are liquid. As a proxy for solid materials, methane does not have measurable significant position shifts (i.e., any shifts are much smaller than VIMS resolution). In addition, the optical constants of methane remain virtually unchanged between liquid and solid at 93 K (Grundy et al., 2002). Thus, we use methane as a general proxy for materials (simple organics) although the spectral and optical constant properties of the actual materials could be much more complicated.

The data of the icy components have been calculated with the 'SPECTRIMAG' radiative transfer code for granular surfaces (Douté and Schmitt, 1998), in sets of 15 different pathlengths spanning 2 orders of magnitude. All components in the constituent library are in the VIMS spectrum and hence simulations with the extracted RT albedos are possible. The mixing model fits the RT extracted albedos with the most compatible mixture of the proxy constituents and linear mixtures thereof, inferring at least 4 constituents (Solomonidou et al., 2018; 2020a). The model provides compositional constraints using the limited number of available atmospheric windows

and that entails that there is no unique solution for the mixtures. A perfect fit cannot be achieved between the simulations and the observations because all radiative transfer codes are incapable of totally reproducing the complexity of Titan's system (atmosphere, surface, and interactions among these convoluted elements) and no simple mixture of components can reproduce what exists on the surface of Titan. Our method tests to what extent the available observations (absolute values and spectral shape) can be match with these basic constituents. The code output includes estimated errors of the derived abundances of the different components of the mixture.

Bitumens are used as proxies to lower the total surface albedo (Moroz et al., 1998; Lellouch et al., 2004; Court et al., 2006; Combe et al., 2007; Hirtzig et al., 2012) as it is expected to be low for Titan. Bitumen on Earth is a very complex intractable mixture containing many hydrocarbon and functionalized hydrocarbon components. It derives from coal and petroleum residues which in turn derived from diagenetically processed humic acids, steroids, and wax lignins from buried (usually vegetative) biologically produced organic matter. It is not likely that bitumen as produced on Earth would be exactly present on Titan. However, in the absence of another good analogue for dark materials we have applied this component as a proxy in our simulations. In particular, bitumen contains a large amount of naphthene aromatics (naphthalene), consisting of partially hydrogenated polycyclic aromatic compounds. We use these as a proxy for complex mixtures of Titan aromatic molecules that fused and linked such as (for fused) phenylacetylene, naphthalene, and phenanthrene (Abplanalp et al., 2019) and linked aromatics such as biphenyl, terphenyl and higher homologs. All solid small-molecule organics included in the spectral library are in 15 grain sizes (10, 20, 30, 40, 50, 75, 100, 150, 200, 250, 300, 400, 500, 750, and 1,000 μm), the laboratory tholins in 6 grain sizes (1, 2, 5, 10, 30, and 100 μm), and the amorphous carbon in 3 grain sizes (10, 200, and 500 μm) (Quirico and Schmitt, 1997; Grundy and Schmitt 1998; Grundy et al., 2002; Bernard et al., 2006; GhoSST @ SSHADE solid spectroscopic database). Hence, in total we examined 90 different spectral possibilities. The spectra data used in this study in the VIMS range can be seen in Figure 3.

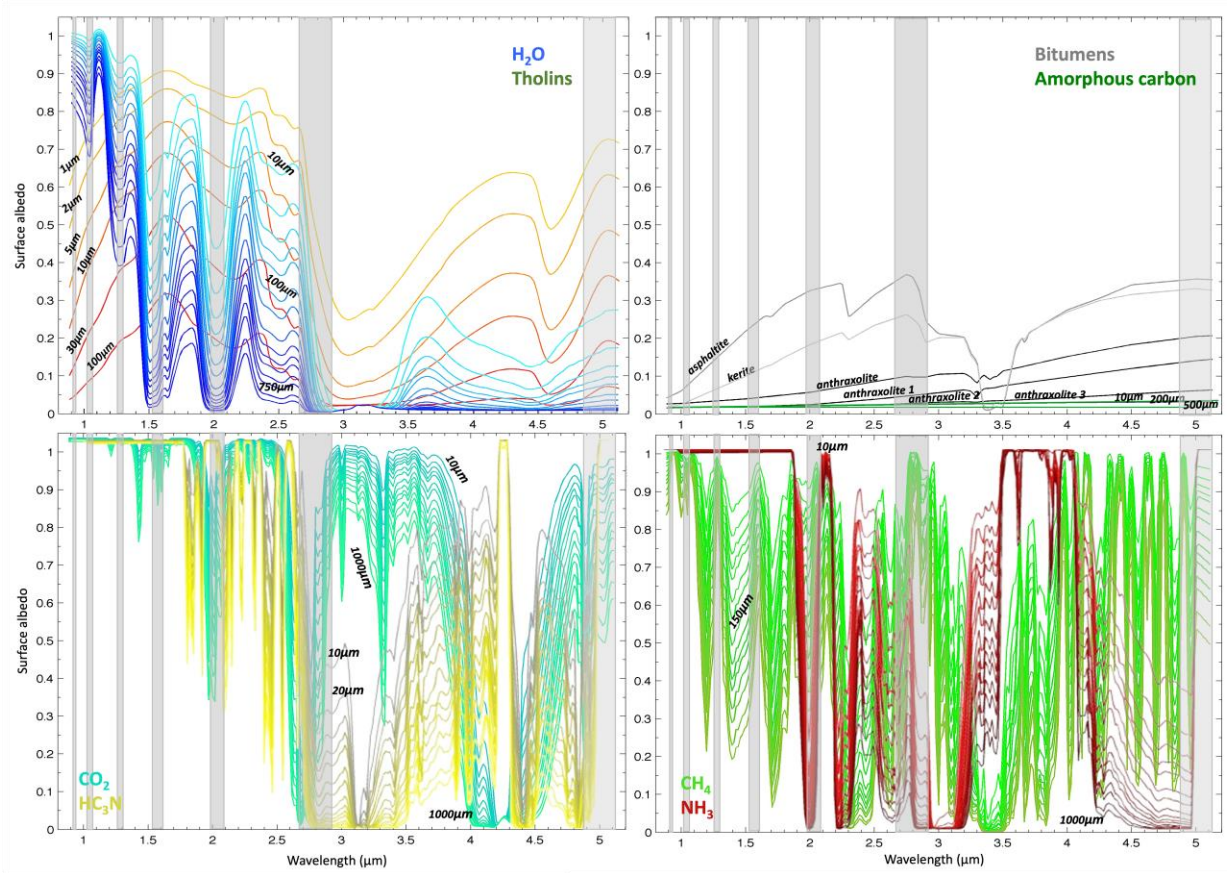

Figure 3. Spectra data of candidate components used in this work adapted from Solomonidou et al. (2020a). H_2O in shades of blue; laboratory tholins in shades of orange; bitumens in gray, and amorphous carbon in dark green; CO_2 in shades of turquoise, and HC_3N in shades of yellow; CH_4 in shades of light green, and NH_3 in shades of red. These spectra are plotted in the spectral range of VIMS at different grain sizes (Bernard et al. 2006; Brassé et al. 2015; GhoSST database, http://ghosst.osug.fr). The light gray columns correspond to Titan's atmospheric windows.

3.2 Haze Estimations and Surface Albedos

The VIMS datacubes shown in Table 2 were acquired at different observational properties and at different times during the Cassini mission (Tb – T113: 2004-2015). The analyzed VIMS pixels from the 261 different locations are expected to include different atmospheric effects, which is something that has been found to occur even at adjacent pixels from within the same VIMS datacube (Solomonidou et al., 2016; 2018). Indeed, the analyses of the VIMS data from the various locations within the Soi crater region showed that the haze contributions to the VIMS data ranges from 70-130% (±5%) with respect to the Huygens Landing Site DISR measurements used a calibration point (Karkoschka & Tomasko, 2010). In particular, the haze contribution to the data seems to present a relative dependance with latitude. Datacubes from flybys Tb, T08, T10, T12, and T77 that cover mostly low to mid latitudes when treated with RT the haze estimation ranges between 70-110%, while from T31 and T97 that cover mostly higher latitudes range from 100-130%.

The examples of extracted surface albedos in the form of weighted averages are shown in Figure 4, including one example for each geomorphological unit and their various types. There are four groups based on their geomorphological characterization: (a) dunes; (b) highlands such as mountainous/hummocky and labyrinth terrains; (c) crater units and SEDs; and (d) plains. In Figure 4 the extracted albedo from HLS is also present for comparative purposes.

The overall albedo values of the dunes (Fig. 4a) at all wavelengths are among the lowest compared to the rest of the units, as demonstrated in previous studies (e.g., Soderblom et al., 2007; Barnes et al., 2008; Rodriguez et al., 2014; Bonnefoy et al., 2016; Solomonidou et al., 2016; 2018; Brossier et al., 2018). The featureless sand sheets (*ds*) present much brighter albedos than the other types of dunes, which we find correlated with their locations, as they appear mostly over 15ºN and are completely absent from the equator. The dark linear dunes (*dl*) and the undivided dunes (*du*) have similar spectral behavior and albedo values within error bars at all wavelengths, except for the 2 μm window where the dark linear dunes have particularly low albedo, suggesting the presence of a constituent very absorbent at this wavelength. The lower albedo at all wavelengths for units closer to the equator is attributed to the transport and incorporation of dark material from the dunes due to aeolian transport processes (Malaska et al., 2016b; Lopes et al., 2016; Solomonidou et al., 2018; 2020a).

The highland terrains (Fig. 4b) present differences in their surface albedos, with the hummocky terrains (*hh*) having low albedo values, agreeing with the results in Solomonidou et al. (2018), and the mountainous terrains (*hm*) presenting significantly high albedo values, especially at the short wavelengths (0.94-2 μm). Interestingly, the undivided hummocky/mountainous terrains (*hu*) have albedo values in between the values of hummocky and mountainous terrains as shown in Fig. (4b). The labyrinth terrains (*lbf*) present relatively high surface albedos, with spectral similarities with the undifferentiated plains (*pul*) (Fig. 4d)

The albedos extracted from crater subunits (Fig. 4c) show that the crater fill 3 (*cf3*) is filled with the same material that is present in the dunes. The crater rim and crater ejecta show very similar spectral behavior and albedo values within error bars, something that was also shown for the Soi crater subunits in Solomonidou et al. (2020a). The albedos of the sharp-edged depressions (*bse*) and of their ramparts (*brh*) are intermediately bright with high values at the double window (2.69-2.79 μm) and the 5 μm window, similarly to the albedos extracted from VIMS data of three empty lake floors at 69ºN-134ºW in Solomonidou et al. (2020b). This study found that the material of the high-latitude empty lake floors is the same as the material of the raised ramparts that appear surrounding less than 10 SEDs of the north pole, suggesting that the ramparts are spectrally distinct from the surrounding plains.

Finally, the plains (Fig. 4d) present a great variety of different albedo values, with the new unit of gradational plains (*pgh*) having the lowest albedo of the plains units, marginally close to that of the dark linear dunes, following the dark linear dunes' drop in albedo from 1.59 to the 2 μm window; a decrease that is not frequently observed in Titan's albedos. The dark irregular (*pil*), the undifferentiated (*pul*), the undivided dark (*pdu*), and the variable (*pfv*) plains present intermediate albedo values at the short wavelengths. The *pfv* is particularly bright at long wavelengths and the *pil* are very bright at the 2.69-2.79 μm double window. This brightness of Soi's *pfv* units at the 2.69-5 μm range was not observed in other locations of variable plains analyzed in Solomonidou et al. (2018) and seems compatible with the high latitude location of the Soi region variables that reach 50º N. The scalloped plains (*psv*) present intermediate to high albedo values at most wavelengths. The streak-like (*psh*) plains are very bright at all wavelengths, agreeing with the results in Solomonidou et al. (2018) and Lopes et al. (2016), while the newly

introduced undivided plains present high albedos at shorter wavelengths (0.94 – 2 μm), as well as at 5 μm.

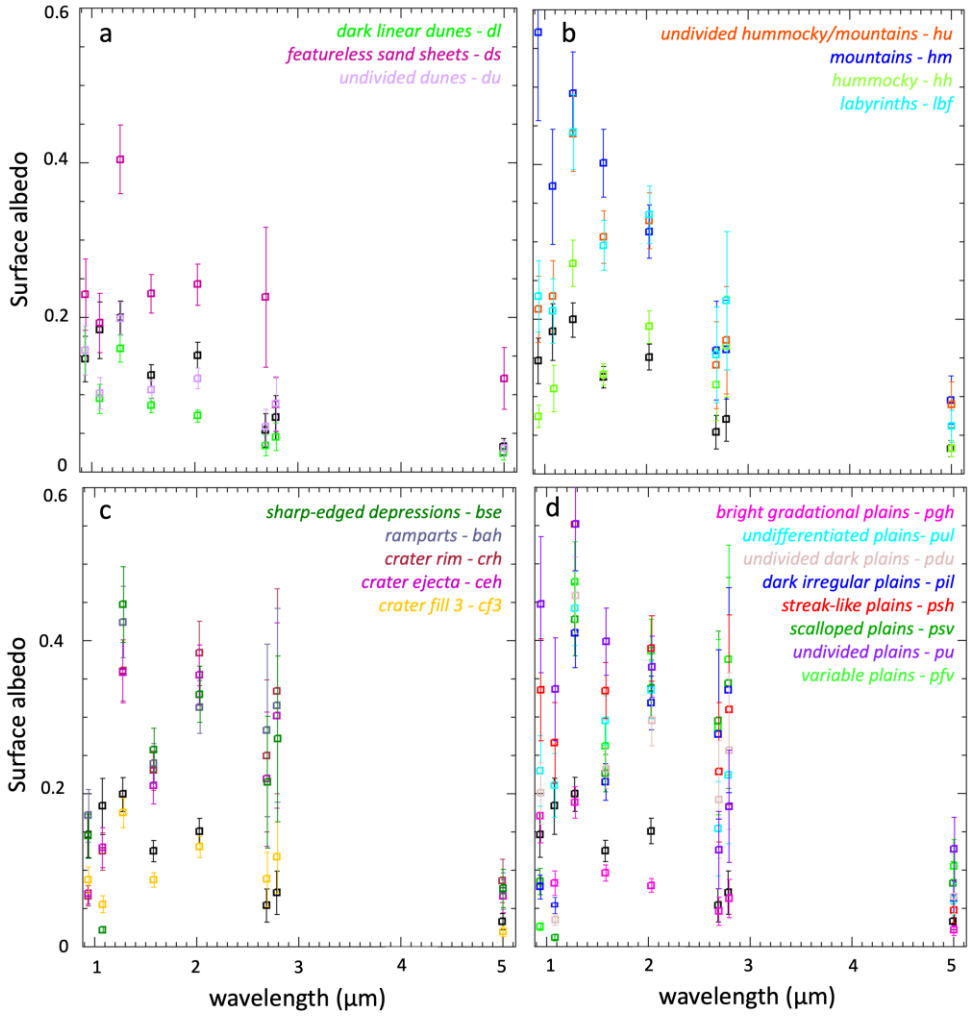

Figure 4. Examples of surface albedo weighted averages in the atmospheric windows as extracted from VIMS data with RT for four different groups of units: (a) dunes; (b) hummocky/mountainous and labyrinth; (c) impact crater units and sharped-edged depressions; and (d) plains. The Huygens Landing Site (HLS) albedos (in black) are used as reference.

3.3 Surface Mixtures

The extracted albedos presented in the previous section are used in the mixing model to provide linear mixture simulations that would fit the albedo data in the most optimal way, given the available albedo points and the candidate Titan materials in the spectral database, and from the perspective of what can be done in such a complex situation with limited available *in situ* observations. Even if the fits between the mixture simulations and the albedo data are not perfect, they provide insights into the surface composition of Titan's top surface layer, which is still unknown even after 13 years of Cassini exploration (e.g., Nixon et al., 2018; MacKenzie et al., 2021). Table 3 includes the results from all 261 locations and Figure 5 presents ternary diagrams for the composition of plains (a), dunes (b), hummocky terrains and labyrinths (c), and craters and

lakes (d). Examples of the mixture simulation results from representative units within the Soi crater region can be found in Figure 6. The χ^2 values from the analyzed areas range from 0.24 to 3.48, suggesting high correlation between the mixture simulations and the albedo data. From first read of Figure 5 it seems that the majority of plains (5a) and hummocky and labyrinth terrains (5c) are lacking the contribution of the dark organic material in their mixtures, something that as expected the dunes (5b) have in abundance. The empty sharp-edged depressions, their surrounding ramparts, and craters on the other hand seem to have a combination of all three constituents in their mixtures.

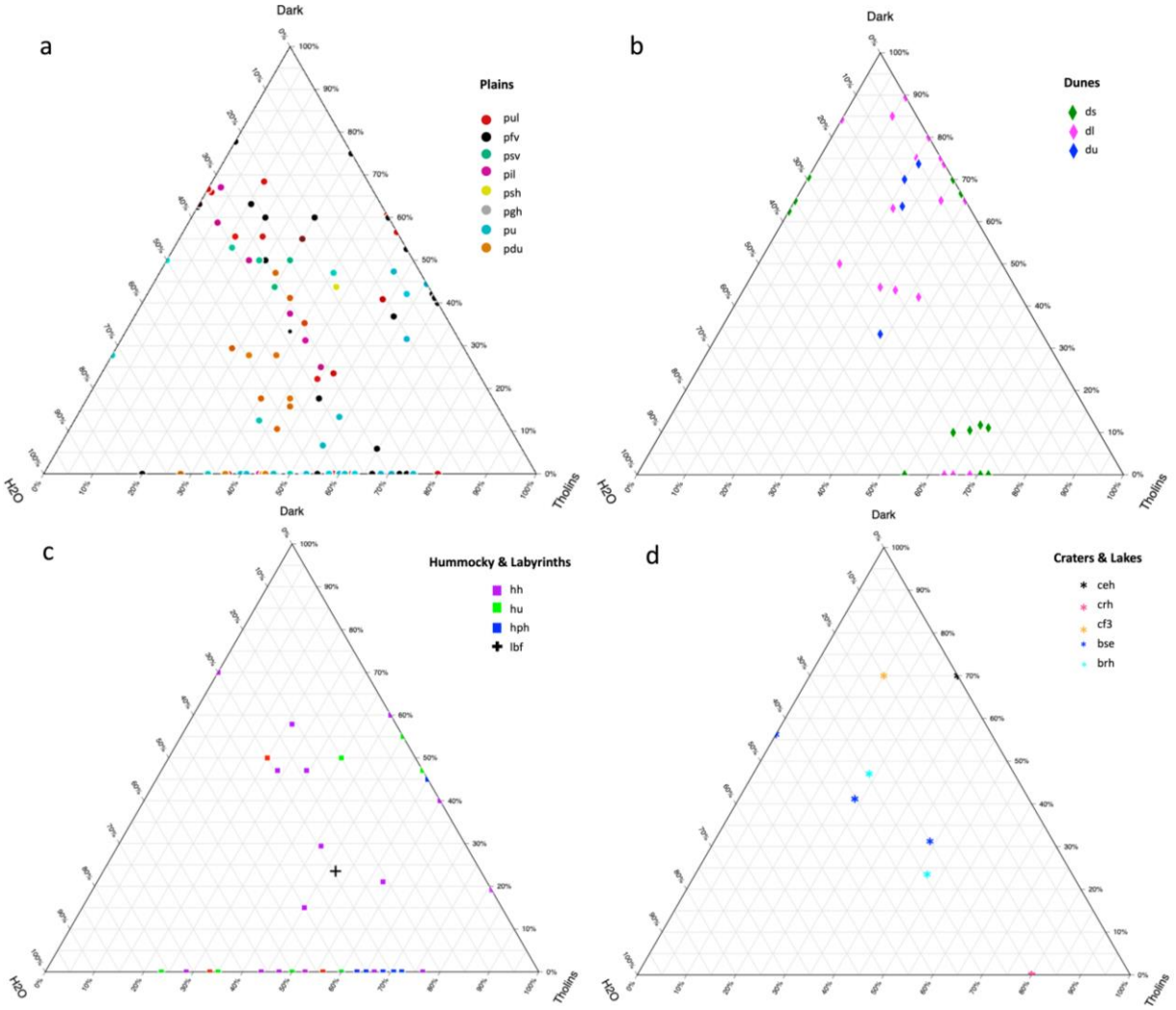

Figure 5. Ternary diagrams representing a composition from the three major constituents: H_2O, tholin-like constituent, and unknown dark constituent. (a) various types of plains; (b) various types of dunes; (c) various types of hummocky terrains and labyrinths; (d) different parts of craters and lake features. Detailed compositional constraints for each unit and their various locations can be found in Table 3.

In our attempts to understand the chemical composition of Titan's surface as well as possible, the code provides simulations of mixtures including at least four major constituents, based on which we built our compositional map for the Soi crater region (see following section). It was particularly difficult to reproduce in some cases the 0.94 and 1.08 μm albedo values,

something that was previously found in Solomonidou et al. (2020a), when studying the composition of Titan's major impact craters. Furthermore, in Solomonidou et al. (2018) in a similar attempt to characterize the composition of the surface, fewer compounds were added from the library, which led to a worse fit especially for 0.94, 2.03, and 2.79μm. In this present study we have added more components in our simulation, increasing the number of component spectra available for potential matches in our library from 75 to 90, when taking into account the grain sizes. For the latter, the best fits are obtained using spectra from specific grain sizes for the different components since the albedo can be very dependent on the grain size, as shown in Figure 3. For the areas where their mixture includes tholins, the best fits are obtained using 30μm and 100μm tholins. For CH_4 ice, the optimal grain size is 1000μm, while for H_2O ice, it ranges from 10μm to 50μm. Finally, among the various bitumens, the ones that provide the best fit with the extracted albedos are amorphous carbon at 200μm and 500μm, along with asphaltite.

In all 261 cases, we obtained matches within error bars in at least four out of the eight wavelengths. Such challenges in spectroscopic analyses for Titan have been faced by previous studies for both ground-based and Cassini-Huygens observations and measurements (VIMS, DISR) (Coustenis et al., 1995; Smith et al., 2005; Tomasko et al., 2005; Brown et al., 2006; Clark et al., 2010; Soderblom et al., 2007). Here, the matches that are more difficult to achieve are at the very short wavelengths, and for some cases the double window (2.69-2.79 μm), and the 5 μm window. The mismatch, especially at the shorter wavelengths, is indicative of the limitations set by the VIMS data, the modeling, and the variability of the material library compared to the expected complexity of Titan's surface. In contrast to previous surface composition simulation studies (Solomonidou et al., 2018; 2020a), here we are better able to match the 2 μm and the 2.79 μm albedo data with mixtures of components. Furthermore, we have a match at 1.59 μm in almost all 261 regions. In addition, some units present very low albedo values at short wavelengths and there is conspicuous absence of fit at 1.08μm compared to other units. Particularly intriguing are the SEDs, ramparts, and labyrinths, which exhibit markedly low albedos at short wavelengths and comparatively higher values at 2.03 and double-window wavelengths (Fig. 6b). This characteristic poses challenges for fitting all atmospheric windows, as the code uses materials within the current databases exhibiting absorption at short wavelengths while strongly reflecting light within the 2.03-2.79μm range. Further work on the Cassini data, along with the advanced development of tools for their processing and additional data from future missions (e.g., Dragonfly) and observations (e.g., JWST), will help us better understand the reasons behind these mismatches and provide solutions for improved fits between the albedos and the simulated surface mixtures.

In the next section we discuss in detail the compositional behavior of each unit. In the next section we discuss in detail the compositional behavior of each unit.

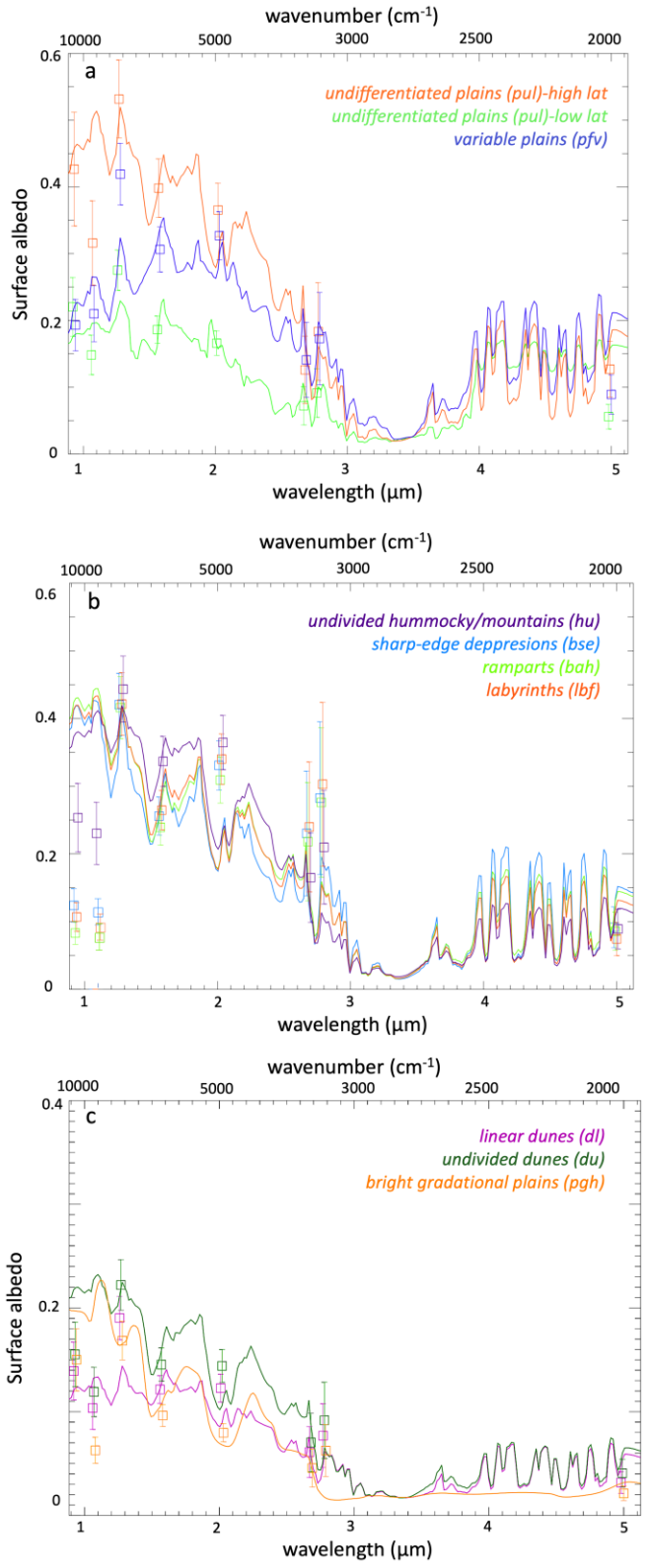

Figure 6. Examples of inferred spectra based on modelled constituent mixtures of different units in the Soi crater region. (a) Examples of an undifferentiated plain from over 30ºN (*pul* -high lat), from close to the equator (*pul* -low lat), and a variable plain (*pfv*). (b) Examples of a sharp-edged

depression (*bse*), of its surrounding rampart (*brh*), a labyrinth terrain (*lbf*), and an undivided hummocky terrain (*hu*). (c) Examples of a linear dune (*dl*), an undivided dune (*du*), and a gradational plain (*pgh*). The point symbols correspond to extracted surface albedos from locations shown in Figure 2 and others, and the full lines to the compositional simulations, which are produced by the code using the best fit attained between the simulated spectra and the albedos. The 3σ error bars are shown on the simulations and are inferred by the code during the extraction of the surface albedos (detailed description of the 3σ error bars can be found in section 3.1).

3.4. Spectral Class Compositional Map

The 261 locations (Figure 2) we analyzed with VIMS from the Soi crater region showed that it is a diverse region in terms of compositional variety for the visible surface (Figure 7; Table 3). Figure 7a shows the extrapolated compositional results of the selected regions of interest as shown in Figure 2 with contact lines distinguishing the boundaries of the various geomorphological units of which we discuss their composition in detail in this section. In Figure 7b, we classified the extrapolated composition from Fig. 7a into ice and organic material; the latter includes the dark material and tholins. Figure 7c shows the results from mapping of the Soi crater region as presented in Schoenfeld et al. (2023). Here, we do not attempt to provide exact molecular composition, given the limitations of the VIMS data described earlier, rather we treat each material as a representative for possible compositions of the upper layer of the surface. Our radiative transfer code takes into account a large number of uncertainties and translates them into error bars as described in section 3.1 and shown in Figures 4 and 6. Given those caveats, we provide constraints on the chemical composition of the surface though the classification of spectral types of materials, focusing on the major constituent of the mixture and up to the 4th constituent in abundance (Table 3). As a reminder, these maps represent compositional constraints of mixtures that possibly make up the very thin veil (few microns) that cover the surface. The deeper layers (few cms) of the surface and their composition are being discussed later in this section (subsection 3.5).

We will examine each unit separately, however one result that is common for all analyzed locations in the Soi crater region is that we found no indication for the presence of significant amounts of carbon dioxide (CO_2), cyanoacetylene (HC_3N), or ammonia (NH_3) ices in the mixtures, to within our aforementioned uncertainties.

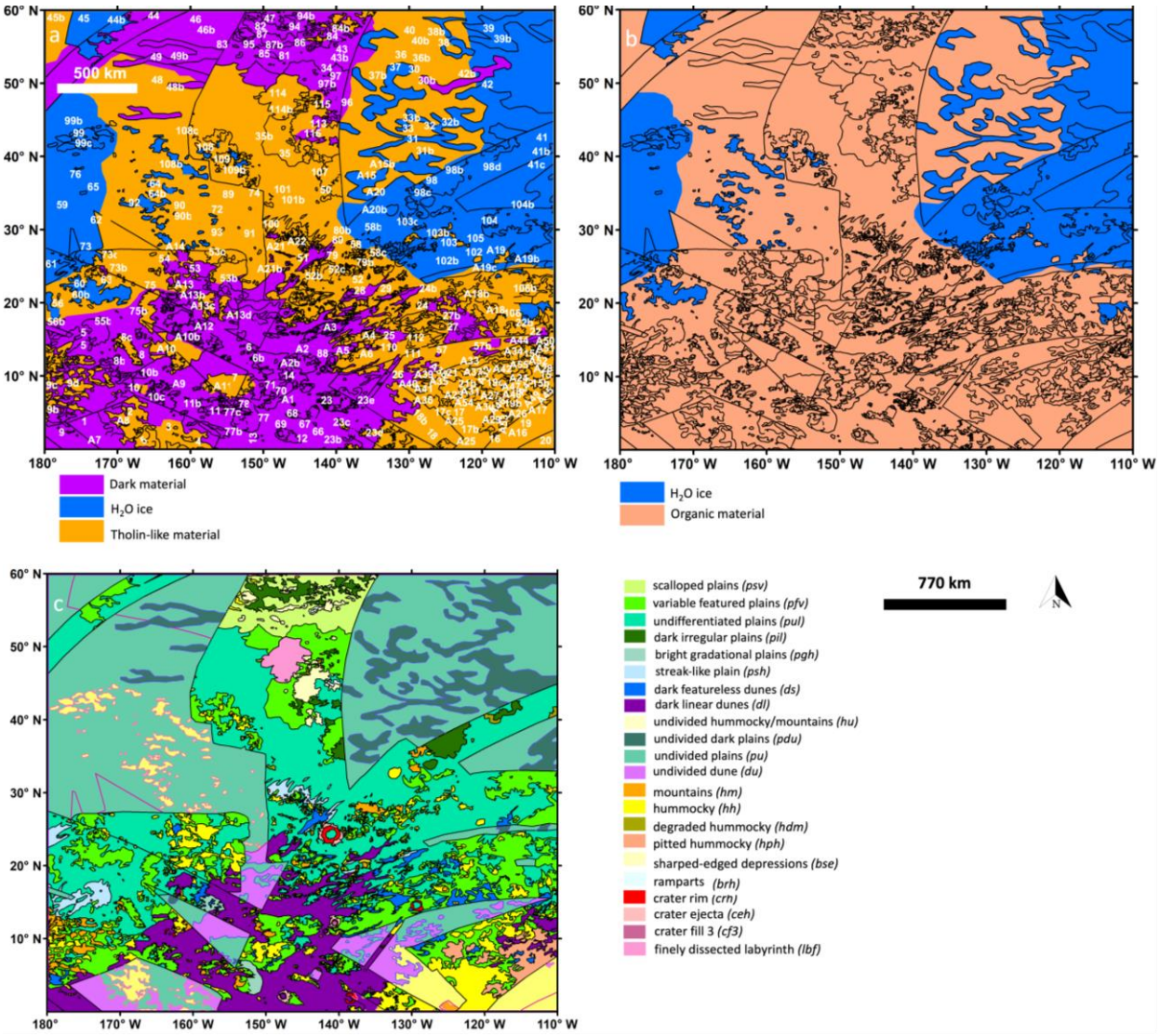

Figure 7. (a) Extrapolated composition map of the Soi crater region for the major constituents from VIMS RT analysis and mixing model simulations with contact lines distinguishing the boundaries of the various geomorphological units based on the boundaries drawn for the geomorpohological map in (c). The numbers represent the selections of regions of interest as shown in Figure 2. The colored pixels are based on their compositional results for the major constituent (blue for water-ice, magenta for dark organic material -a combination of bitumens and amorphous carbon, orange for tholins). (b) Same as (a) with classification between ice (blue) and organic (pink). (c) Geomorphological map for all SAR and non-SAR data (Schoenfeld et al., 2023) at zero transparency (the map layer is fully opaque), same color scheme as the global geomorphological map of Titan in Lopes et al. (2020).

All dune terrain units (*dl*, *du*, *ds*) have a primarily organic nature, but the different units present differences in their secondary materials. The highland terrains (*hh*, *hm*, *hu*, *lbf*) lack a characteristic major constituent among all their different units (Fig. 5c) and their nature depends on their location. One common characteristic of all highland terrains is that they all appear to have tholins in their mixtures (not as a major constituent) in significant amounts and that the presence

of CH_4, as a tertiary or quaternary constituent, in their composition is stronger than in the dunes. The three crater units (*crh*, *ceh*, *cf3*) are primarily organic with the presence of water-ice only in the mixtures when the crater is located in regions dominated by plains (around the 30ºN latitudinal zone), as shown in Solomonidou et al., (2020a). One such example is Soi crater. Furthermore, the composition of the empty sharp-edged depressions (*bse*) and their surrounding ramparts (*brh*) (Fig. 5d) was found to be the same or very similar to those of the north polar empty lakes around 70ºN discussed in Solomonidou et al. (2020b), which is a mixture of organics, water-ice, and simple organics. In Solomonidou et al. (2020b), it is noted that the emissivity of the northern raised ramparts points to a moderate-to-high contamination by organics. This emissivity is comparable to that of the northern empty basins. Combined with the VIMS results, this observation suggests that the ramparts and the empty lake floors, both located at the north pole, may share the same or similar composition. Here, as illustrated in Table 3 and discussed later in section 3.5, and similarly to the northern SEDs, the midlatitide empty SEDs are enriched in organic components.

The plains, in the same way as they present variable morphologies, present complex mixtures in their visible composition. The eight different units of plains are covered by different mixtures of materials. The recently introduced plain type (Schoenfled et al., 2023), the gradational plains (*pgh*), is located close to the equator and below 20ºN and is primarily organic in nature (dark material) and as shown in Fig. (4c) completely covered by dune materials. In contrast, the streak-like plains (*psh*) over 20ºN do not include any dark material in their mixture and appear almost equally rich in water-ice and tholins. Similarly, the undivided dark plains (*pdu*), even though they were expected to be mostly abundant in the organic dark material due to their dark signature in VIMS, are instead relatively richer in water-ice, presenting some of the highest abundances in water-ice within the Soi crater region, along with the highland terrains. The undivided plains (*pu*) and the variable plains (*pfv*) are also covered by a mixture of organics and water-ice. The dark irregular plains (*pil*) and the scalloped plains (*psv*) are spectrally very similar, varying primarily in the amount of dark material present. Counterintuitively, the dark (in SAR) irregular plains, on average, have lower amounts of the dark material component than the scalloped plains. Previous analysis from a couple of scalloped plains (*psv*) from the region, which were analysed in Solomonidou et al. (2018) from older flybys (T25 and T94) than T97 (Table 2) and were found to be mainly abundant in water-ice, here are instead found to be abundant in the dark material (major) and water-ice (secondary). While our model uncertainties are significant, this may represent a change in the surface composition, which we hypothesize to be related to fluvial activity depositing a fresh overlying layer of dark material. Moreover, the dark irregular plains (*pil*) are mainly concentrated in latitudes higher than 30ºN within the Soi crater region and were expected to be primarily rich in water-ice; however, even though water-ice is present in their mixtures, organic material seems to be the most abundant. Lastly, the undifferentiated plains (*pul*) seem to present a similar latitudinal dependence as shown in Solomonidou et al. (2018), with those in the 0-20ºN zone being abundant in the dark material, while those in the higher latitudes being richer in water-ice (see Figure 7a;c). However, a large number of undifferentiated plains sample locations have tholins as the most abundant constituent, making these locations having the highest abundances in tholins. There is a significant amount of CH_4 in some cases reaching even 25% of the total mixture in some samples.

Detailed compositional constraints for each unit and their various locations can be found in Table 3. These are all suggestive compositional constrains and we acknowledge that they can be satisfied by other compositional solutions as well.

3.5 Emissivity results

As explained in Janssen et al. (2016) the presence of water-ice in the near subsurface is strongly indicated by the higher degree of volume scattering observed in radar-bright and low emissivity regions. Indeed, water-ice is highly transparent to microwaves, and therefore allows longer pathlengths which results in a higher probability for microwaves to encounter scatterers embedded in the subsurface. This in turn causes volume scattering, thus enhancing the radar cross-section and lowering the emissivity (Paillou et al., 2008; Janssen et al., 2016). A characteristic range of emissivity values for the different geomorphological units within the Soi crater region can be found in Table 1 in Schoenfeld et al. (2023) and the map of Figure 8. Though somewhat arbitrary, we interpret the units with values lower than 0.90 to be enriched in water-ice in their near subsurface (top decimeter of the regolith), and we interpret units with emissivity (E) values larger than 0.95 to be enriched in organic materials, and all values in between (E=0.90-0.95) to be consistent with a mixture of the two (Werynski et al., 2019; Malaska et al., 2020; Solomonidou et al., 2020a). The units that are more enriched in water-ice in their near subsurface (40 cm to 1 m) according to the emissivity values are the mountains, the hummocky terrains, and the undivided mountains/hummocky. The VIMS analysis agrees with the strong presence of water-ice in these units, which is always present in the mixtures of the top layer surface of these units; at few locations as major constituent (e.g., items 231-234 of Table 3) and except a very few regions of interest (e.g., items 192, 228 of Table 3) located near the equator which are completed coated with organic material (Table 3, items 191-249). However, a notable difference between the emissivity and VIMS/albedo results is the inconsistency in the major constituent of the mixtures at the southeast 'corner' of the Soi crater region of interest. Here, the emissivity data indicate a major water ice constituent (Fig. 8), while VIMS data suggest an organic one, specifically tholin-like material (Figs. 7a and 7b).The units that are more enriched in organic material according to emissivity are the dunes (*dl, ds, du*) with values ranging between 0.93 and 0.98. As shown in the previous section, the VIMS results of the top surface are in agreement with the organic nature of all types of dunes. Other units with strong organic nature according to emissivity include the undivided irregular plains (*pil*, E≥0.97), the undifferentiated plains (*pul*, E≥0.97), the undivided plains (*pu*, E≥0.96), the undivided dark plains (*pdu*, E≥0.94), the streak-like plains (*psh*, E≥0.95), and the labyrinth terrains (*lbf*, E≥0.95). The VIMS RT analysis of the top surface agrees with the organic appearance of *pil*, *pu*, and *pul* (depending on the latitude). However, the undivided dark plains and the streak-like plains appear more abundant in ice than organic material in the first few microns of their surface. It is important to note that the size and extent of the different features plays an important role in their emissivity measurements since small and thin patches of water-ice lying on an organic substrate may not be detected by radiometry. The rest of the units (*psv, pgh, du, cf3, ceh, ceh, brh,* and *bse*) have intermediate emissivity values suggesting a mixture of abundant icy and organic material with emissivity values ranging from 0.92 to 0.94. The VIMS analysis agrees with this icy and organic nature of the top surfaces of these units. Finally, the variable plains (*pfv*) present a large range of emissivity values (E=0.91-0.96) consistent with VIMS analysis suggesting a varying ice vs. organic nature for the unit depending on the location at all depths, from the thin μm veil covering the surface to 10's of centimeters deep in the surface.

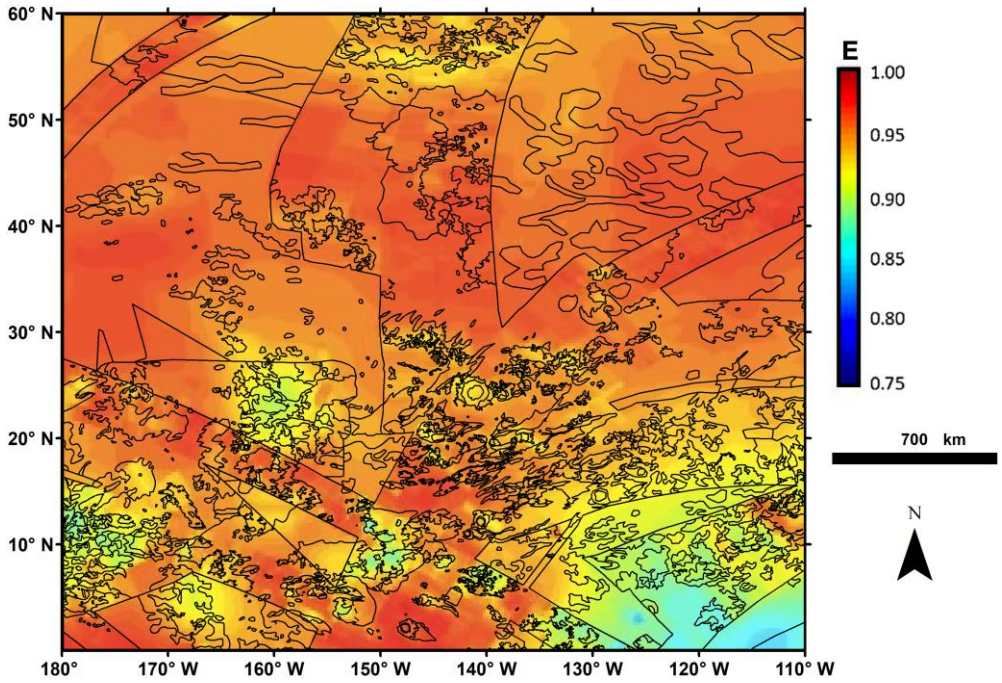

Figure 8. Emissivity map of the Soi crater region with contact lines distinguishing the boundaries of the various geomorphological units. Emissivity data from Janssen et al. (2016).

4 Geologic History of the Soi crater region

4.1 Surface Processes in Soi crater region

The Soi crater region is geomorphologically and compositionally variable, as shown in Figure 7. In this section, we discuss the identified features from the various terrain types within the region and we provide a geologic synthesis with respect to their chemical composition, geomorphology, and potential geologic processes.

Impact processes: There are 10 impact craters identified within the Soi crater region (Wood et al., 2010; Neish et al., 2015; Hedgepeth et al., 2020; Schoenfeld et al., 2023). As also shown in Figure 4c, where the differences in spectral responses between the ejecta and the floors are subtle, the Soi crater region includes characteristic examples of how erosion affects the floors of the craters by allowing dune material to intrude and deposit organic sand.

Inferred Material Transport: Wind and material transport models (Malaska et al., 2016b) have helped distinguish different processes for the Soi crater region. Schoenfeld et al. (2023) presented the sketch map of inferred material direction for the region, which we combined with the map of chemical composition and present in Figure 9. The directions were based on alignments and tapering morphologies of dunes, windstreaks and other terrains which enable the transport direction to be inferred, for details see Malaska et al., (2016b). The map of chemical composition correlates well with the flow path as shown in Figure 9b, with "extensions" of materials suggesting that aeolian transport and subsequent deposition influences surface composition through delivery of fine-grained saltating material (e.g., Schurmeier and Dombard, 2018). For example, in Figure 9b, extended "fingers" of dune materials (purple) are in the tholin-like plains zone (orange area). While the inferred transport direction was determined from geomorphology (primarily by SAR),

it also appears to correlate to the compositional retrieval as well. This compositional analysis further shows that the majority of the equatorial and low latitudes (0-20ºN) are dominated by the dark organic material that transition into an area more dominated by tholin-like materials in the midlatitude. Similarly, mid to high-latitude zone with dark organic spectral components at 50-60ºN transitions to tholins in the midlatitudes (below 50ºN) in a similar fashion. The areas rich in water-ice appear over 20ºN and they are suspected to be unrelated to material transport and deposition and may be more connected to erosional processes. One possible mechanism that could explain these observations would be a surface deposit of equatorially-derived mixed materials, including water-ice and dark materials, which following deposition in the midlatitude plains either have the coating removed (possibly through dissolution/leaching) to reveal a water ice-enriched/tholin lag, or deposition with later coating from bright tholins from atmospheric airfall.

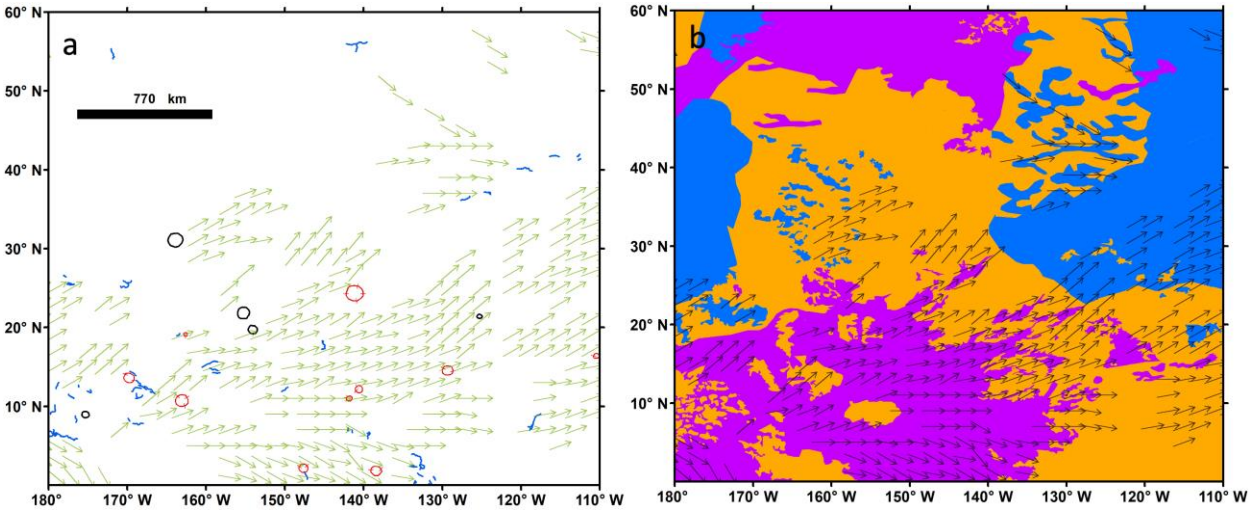

Figure 9. (a) Sketch map of inferred material transport direction (arrows) in the Soi crater region after Malaska et al. (2016b), published in Figure 8 in Schoenfeld et al. (2023), with valleys and channels (blue lines), craters (red), and putative craters (black). (b) Material transport direction on top of the compositional map (color legend in Figure 7b).

Fluvial, Aeolian, and Lacustrine Processes: Two significant units found in the Soi crater region, the bright gradational plains (*phg*) and the bright streak-like plains (*psh*), are proposed to be two endmembers of the same type of fundamental deposit, reflecting either dominantly fluvial or aeolian transport, respectively (Schoenfeld et al., 2023). These aeolian and fluvial origin assumptions are based on geomorphological results from SAR data as presented in Schoenfeld et al. (2013). According to the studies by Schoenfeld et al. (2023) and Malaska et al. (2016), throughout all the mapping datasets the bright gradational plains and the bright streak-like plains have both very similar signatures (bright), diffuse internal texture, and comparable microwave emissivity. The elongated nature of *psh* with directions parallel to adjacent linear dunes suggests aeolian origin for *psh*, while the *pgh* units appear as broad plains originating from alluvial fans and channels. The RT results from the analysis of VIMS data are consistent with these proposed interpretations with regards to their origin (Sections 3.3, 3.4; Figure 4), since in the very top layer of their surfaces, *pgh* is one of the lowest in albedo, which could be consistent with fluvial origin with a surface dampened by liquids. Meanwhile, *psh* is particularly bright at all wavelengths, interpreted as an aeolian deposit with a lack of ponded liquids. As a result the high in albedo values

(bright) *psh* are associated with a dry surface, while the low in albedo values (dark) *pgh* with a wet surface. Radiometry data are inconclusive (*pgh*: 0.92-0.93 and *psh*: 0.94-0.96).

Lacustrine Processes: There are 60 features within the Soi crater region consistent with the morphology and size of the sharp-edged depressions (*bse*) of the north pole (Schoenfeld et al., 2023). In addition, two plains units, the scalloped plains (*psv*) (spectrally analysed in Solomonidou et al., 2018) and the dark irregular plains (*pil*), which are only been found in the midlatitude zone of Titan, are found adjacent to the SEDs (Schoenfeld et al., 2023).

As noted in Malaska et al. (2016a) and Lopes et al. (2020) both units play an important role in the definition of the mid-to-pole transitional zones and due to morphological and microwave emissivity measurements it is suggested that the *psv* is a unit with a thick organic layer much like the undifferentiated plains (Schoenfeld et al., 2021), with which the spectral analysis agrees, suggesting an organic nature with the dark material being dominant (Fig. 6). However, compositional analysis of the *psv* unit suggests that the second most abundant material in the optical surface is water-ice. We propose that this material is mostly organics at depth (consistent with microwave emissivity), but with an optical coating on the top consistent with spectral analysis, which is the opposite of what seems to occur at the Xanadu part of the Soi crater region. As discussed earlier, temporal analysis reveals an interesting temporal albedo change, with two particular *psv* becoming more abundant in dark material in 2014 (T97) than they were in 2007 (T25) and 2013 (T94) (Solomonidou et al., 2016; 2018). All *pil* and *bse* share similar estimated compositions with *psv* having dark material and water-ice mainly in the mixtures of their top layer.

4.2 Correlation of morphology and composition

We have analyzed the Soi crater region and identified various combinations of mixed materials in the top layer of the surfaces of the 22 geomorphological units, including organics, methane, and water-ice.

Our compositional mapping provides a glimpse into the compositional evolution of Titan. Similar to lower equatorial regions, we find abundant dark material to be the major constituent of a mid to high-latitude region (>40ºN, Fig. 7a). This is also the area where scalloped plains are 'hosting' the midlatitude SEDs and the dark irregular plains (40-60ºN, 140-170ºW). In addition, methane-like (simple organics) spectral features are found widespread in the Soi crater region. The high emissivity results consistent with organic materials agree with the constraints put by the VIMS results except for two units: the dark irregular plains and the streak-like plains and the Xanadu region included in the Soi crater region, suggesting compositional differences in the μm to cm layers.

In early VIMS studies, the major spectral "bright" units were found to generally correspond to mountains and elevated areas in radar (Barnes et al., 2007). Our results from the Soi crater region show that there is a significant amount of tholins that appears to be covering the top layers of the hummocky and mountainous terrains at the low latitudes (Fig. 7a), even though the vast majority of the low latitudes of the Soi region is covered with the dark organic material. Notably, another group of hummocky terrains is located in the midlatitudes (30-50ºN) of the Soi crater region and consists mainly of water-ice with a secondary component of tholins. One common characteristic of all highland terrains is that they all appear to have tholins in their mixtures in significant amounts and/or significant amounts of H_2O ice. In addition, the percentage of methane-like materials (simple organics – aliphatic hydrocarbons) in top surfaces found at higher latitudes is larger than those found at lower latitudes (Table 3). Exposed crater rims show a mixture of only water-ice and tholins, suggesting that after the impact revealed water-ice (Crosta et al., 2021), it

was then coated in tholin, but not dark material. However, some highland areas that are exposed to significant fluxes of dune material also show dark material present, while those more protected appear to have less dark material present. In Solomonidou et al. (2018) the hummocky/mountainous units (all located near the equator and 210-245ºW) were among the darkest, while in the Soi crater region they are the brightest in the short wavelengths suggesting some combination of materials that made them very bright at the short wavelength, which we attribute to increased tholin presence. The labyrinth terrains, even though they only appear in the Soi region at a specific location at around 50ºN and represent only ~0.4% of the entire Soi crater region, spectrally look very similar to the ones analyzed in Solomonidou et al. (2018), namely Junction, Tleilax, and Richese and those in Malaska et al. (2020). The Soi region labyrinths are spectrally very similar to the undivided plain materials (*pu*), in both derived RT VIMS and microwave emissivity. They are both consistent with a surface of tholins and water-ice with bulk suggesting mostly organics.

Most craters with the Soi crater region appear to be almost entirely buried under organic material. The ones close to the equator lack any water-ice and are predominantly organic-rich, while the Soi crater rim and ejecta are rich with tholins, followed by water-ice, as also suggested in Solomonidou et al. (2020a).

The undivided dark plains (*pdu*) present some of the highest estimated percent abundances of water-ice within the Soi crater region, along with the hummocky/mountainous terrains. There are, however, three *pdu* high latitude exposures rich in the dark material mixed with water-ice. These differences of the optical surface between the different locations of the same unit suggest that either aeolian or fluvial activity removed part of the optically thin coat of the surface and revealed underlying, possibly wet material. Similarly, the absence of the dark organic material in the undivided plains (*pu*) could be attributed to aeolian and/or fluvial processes that have removed these materials from the visible surface.

Finally, most cases of the featureless sand sheets unit (*ds*), which only appear over 15ºN, appear to be midway in composition between dune sands and midlatitude plains. That is, relative to the dunes, the sand sheet material has less dark material, but more tholin material. This is in contrast to the nature of the linear dunes (*dl*) of the Soi crater region, which are very consistent with having a dark organic composition, at least on the top surface. The featureless nature of *ds* and the fact that the tholins are often secondary suggests either an addition of tholin material to change the relative percentage, or a removal of dark materials. The generic results on the dune unit agree with the organic and less water ice nature of the VIMS ‘brown’ unit that corresponds to the dunes as per previous studies (Barnes et al., 2007; Soderblom et al., 2007).

Previous studies have highlighted a notable correlation between the chemical composition of the thin layer covering Titan's surface, as observed by VIMS (with a thickness on the order of micrometers), and latitude (Lopes et al., 2016; Malaska et al., 2016; Solomonidou et al., 2018; 2020a). While there are instances where geomorphology and composition coincide, such as the distinct 'icy' undivided hummocky terrains (*hu*) within the expansive undivided plains (*pu*) of organic origin at midlatitudes, the influence of latitude, as well as aeolian and fluvial processes, appears to exert significant control over the surface material comprising the thin top layer.

4.3 Interpreted geologic history

The Soi crater region has the typical geomorphology of most of Titan’s surface. It contains plains, dunes, and mountainous terrains (Malaska et al., 2016a; Lopes et al., 2020; Schoenfeld et al., 2021; 2023) and a latitudinal dependence in chemical composition revealing almost complete

coverage of organic material in the equatorial regions and a surface expression of water-ice in the midlatitudes (Solomonidou et al., 2018; 2020b). However, at the higher latitudes a different geologic history is apparent for the Soi crater region.

The presence of dry lakes into the midlatitudes as low as 40ºS supports the hypothesis that Titan had a wetter climate in the past (e.g., Moore et al., 2014). At these midlatitudes, scalloped plains and dark irregular plains have been identified (Schoenfeld et al., 2023) adjacent to the SEDs; this plain/lake northern area is one of the most interesting parts of the Soi region given that it is the first time that the dark organic material has been identified in abundance in a mid-to-high latitude area in the VIMS RT analysis (Fig. 7a).

Our results show that the areas around latitude 35ºN are dominated by surface spectral responses typical of tholin materials, with ice-like materials and dark materials as minor components. Compared to the lower latitudes, there is an enhanced presence of aliphatic hydrocarbon-like materials (methane) in the midlatitudes, while in the higher latitudes, there is an even greater presence. Our compositional analysis is consistent with a gradation of aliphatic hydrocarbon materials being low at the equator, and increasing in relative percentage at higher latitudes (e.g., Mitchell, 2008; Rannou et al., 2006; Tokano et al., 2005; Faulk et al., 2017). The equatorial regions and high midlatitude plains units both contain elevated amounts of dark materials with a lower amount of tholin material when compared to the midlatitude plains units.

From arguments presented in Malaska et al. (2016b) on material transport, Titan's midlatitude regions appear to be areas fed from converging material coming from high latitudes towards the SE, and from equatorial areas towards the NE. This suggests that the midlatitude regions are composed of end stage of Titan windblown deposited materials that have since been subjected to rainfall and perhaps other aging processes. We find that materials at these convergent latitudes are spectrally similar to tholin-like materials and water ice-like materials. In order to convert dune materials and polar plains materials to midlatitude materials requires either removing the dark material component, or adding additional tholin components.

Addition could be due to density-selective transport, if we assume that all three materials have differing densities and/or material properties. For fluvially transported materials, large-scale storms (Faulk et al., 2017) have the potential to transport significant quantities of sediment as overbank deposits. If the tholins and water-ice materials are particularly buoyant compared to the dark materials, then floodplains should lack any significant dark material components. With greater spatial resolution, we would therefore expect floodplains to have a decreasing dark material component away from any given channel. Previous authors have noted the lack of channels in the midlatitude plains (Miller et al., 2021), although there may be effects that obscure the radar signature. In contrast, aeolian processes may transport all three types of sedimentary materials at any given time. To explain the dearth of dark materials at the convergent latitudes, we therefore require that such materials simply do not get deposited there. This could be due to either physical or chemical breakdown over short transport distances, or that the dark materials are denser than the other two sedimentary materials and get left behind due to density-selective transport. In this scenario, we postulate that dark materials may be denser and/or weaker, with both fluvial and aeolian mechanisms acting to sort Titan's different sedimentary materials. This would be analogous to size-selective transport on Earth, except with density playing the role in giving rise to uniquely separated deposits of sedimentary materials.

An alternative possibility is the removal of the dark organic component from the material deposited at the convergent latitudes. Tholin materials and water-ice materials are both predicted to be among the least soluble materials on Titan and would theoretically form a remnant lag

deposit, as more soluble materials, which could possibly include the dark materials, were leached away into the subsurface by occasional rainfall. Leaching in geology corresponds to loss of soluble substances from the top layer of the surface by percolating precipitation. Dark materials are present in deposits to the N and in dune materials in the S in the Soi crater region. Since the dark materials are present in presumably wetter polar deposits, we postulate that some of the dark materials may be sourced there (possibly involving lakes or fluvial activity), while the midlatitudes create a "sink" for these materials. We thus present an alternative compositional evolution cycle where grains and materials coated in dark materials are delivered through aeolian transport into the deposition belts and subjected to extensive leaching which dissolves the dark materials and allows those dissolved materials to percolate into the deep subsurface, thus creating remnant optical surface lag of insoluble materials rich in either water-ice or tholins (Fig. 10). This implies that grains coated in dark materials are more recently formed and have not had their dark material coatings removed. This also implies that dark material would be sourced at high latitudes (for northern polar regions) and at low latitudes (for equatorial dunes).

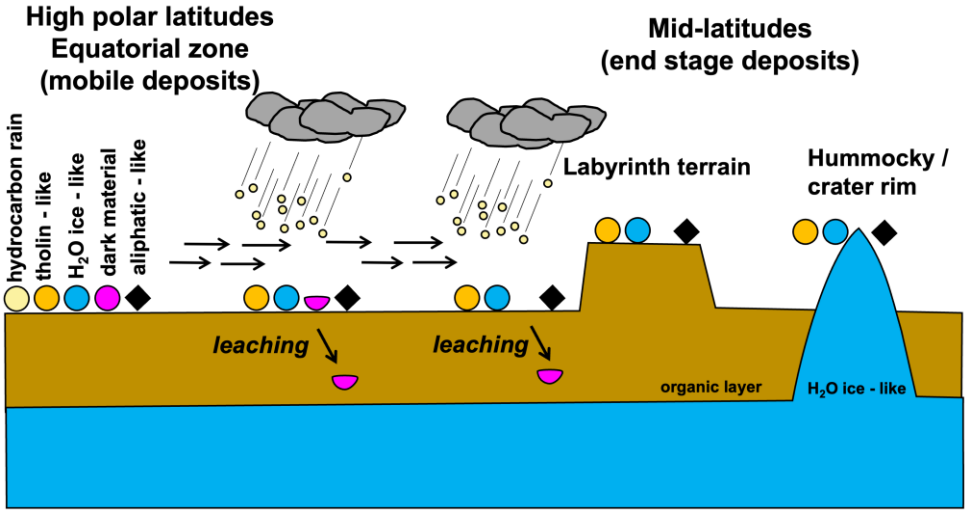

Figure 10. Scheme showing midlatitude leaching of dark material from episodic rainfall on Titan.

Older exposed terrains thus should also be composed of tholins and water-ice materials, as long as they are not receiving new dark material inputs. Thus, the mountains in the SE section of Figure 7c, which is part of the extreme part of Northern Xanadu, appear to be 'protected' from dark material deposition, or, most likely that removal process of the dark material have proceeded quicker than overall deposition. Overall, we envision a scenario as shown in Figure 10, where mobile materials contain dark material, that becomes leached, likely from episodic rainfall, as it arrives to its end-stage destination in the midlatitudes. This scenario as pictured also is supported by microwave emissivity data, which probes deeper. While end stage surface lag composed of tholins coats labyrinth, mountain, and plains almost equally, the deeper probing microwave emissivity can discriminate between hummocky and mountain materials composed of water-ice, and scalloped/undifferentiated plains and labyrinths composed of organic materials.

5 Conclusion

The Soi crater region is an important Titan region as it represents the transition between the equatorial, the midlatitudes, and the high-altitudes of the northern hemisphere of Titan. Our analysis developed a working hypothesis for the formation and evolution of the Soi crater region through the combination of the geomorphological mapping performed by Schoenfeld et al. (2023) and compositional mapping and radiative transfer analysis performed here. Our work suggests propable relationships between the dunes (source), scalloped plains (source), and undifferentiated plains (sink) and brings together and explains the differences in nature of the top layers of the surface from infrared spectra and microwave emissivity measurements. It also infers the geological processes and relationships responsible for their formation and evolution. We suggest that the dark material is a mobile unit that indicates "young" terrains and compositions, while tholin/water-ice mixtures that dominate areas around latitude 35ºN show a material that is older and closer to end stage aeolian plain deposits. This suggests that Titan's compositional evolution cycle includes aeolian transport and leaching. These results provide a better understanding of the geologic processes that govern Titan's surface and will help enhance the science return of future missions such as Dragonfly, and other mission concepts (e.g., Tobie et al., 2014; Lorenz et al., 2021; Barnes et al., 2021; Sulaiman et al., 2021; Rodriguez et al., 2022).

Acknowledgments

We would like to thank the two anonymous reviewers for their thoughtful comments and efforts towards improving our manuscript. This research was partly supported by the NASA Astrobiology Institute through its JPL-led project entitled Habitability of Hydrocarbon Worlds: Titan and Beyond. This research was partly supported by the *Cassini* Data Analysis and Participating Scientists Program (CDAPS) grant #NH16ZDA001N to R.L. A.S. and A.C. acknowledge support from the CNES Appel annuel à Propositions de Recherche Program. A.S. was partly supported by the Czech Science Foundation (grant no. 20-27624Y). S.P.D.B. acknowledges support from the Heising-Simons Foundation (51 Pegasi b Fellowship). Part of this work was conducted at the Jet Propulsion Laboratory (JPL), California Institute of Technology (Caltech) under contract with NASA, and the Hellenic Space Center. ©2023 California Institute of Technology. Government sponsorship acknowledged.

Open Research

All *Cassini* data used in this article can be accessed in the Planetary Data Systems (PDS), PDS Image Atlas (https://pds-imaging.jpl.nasa.gov/search/?fq=-ATLAS_THUMBNAIL_URL%3Abrwsnotavail.jpg&fq=ATLAS_MISSION_NAME%3Acassini&fq=ATLAS_INSTRUMENT_NAME%3Avims&fq=TARGET%3Atitan&q=*%3A*) for VIMS and (https://pds-imaging.jpl.nasa.gov/search/?fq=ATLAS_MISSION_NAME%3Acassini&fq=TARGET%3Atitan&fq=-ATLAS_THUMBNAIL_URL%3Abrwsnotavail.jpg&fq=ATLAS_INSTRUMENT_NAME%3Aradar&q=*%3A*) RADAR. The detailed product IDs for VIMS can be found in Table 2. The spectral library databases can be accessed here: http:// ghosst.osug.fr. Full descriptions of the

radiative transfer model are provided by Hirtzig et al., (2013) (https://doi.org/10.1016/j.icarus.2013.05.033). The VIMS analysis was done using the ENVI Imaging and Analysis software (https://www.l3harrisgeospatial.com/Software-Technology/ENVI) and the Interactive Data Language (IDL), both provided by L3Harris Geospatial.

References

Abplanalp, M.J., Frigge, R., Kaiser, R.I., (2019). Low-temperature synthesis of polycyclic aromatic hydrocarbons in Titan's surface ices and on airless bodies. Sci Adv. 5(10), eaaw5841.

Barnes, J. W., Brown, R. H., Turtle, E. P., McEwen, A. S., Lorenz, R. D., Janssen, M., et al. (2005). A 5-micron-bright spot on Titan: Evidence for surface diversity. Science, 310, 92–95.

Barnes, J.W., Brown, R.H., Soderblom, L., Buratti, B.J., Sotin, C., Rodriguez, S., Le Mouelic, S., Baines, K.H., Clark, R., Nicholson, P., (2007). Global-scale surface spectral variations on Titan seen from Cassini/VIMS. Icarus 186, 242–258.

Barnes, J.W., et al. (2008). Spectroscopy, morphometry, and photoclinometry of Titan's dunefields from Cassini/VIMS. Icarus 195, 400–414.

Barnes, J. W., Hayes, A. G., Soderblom, J. M., MacKenzie, S. M., Hofgartner, J. D., Lorenz, R. D., Turtle. E.P., Radebaugh, J., Burr, D., Lora, J., Neumann, G., Vance, S., Lopes, R., Nixon, C., Corlies, P., Regoli, L., Sciamma-O'Brien, E., Schindhelm, R., Rodgriguez, S., Coll, P., Le Mouélic, Heslar, M., Dhingra, R., Stekloff, J., Sittler, E., Solomonidou, A., Malaska, M.J., Neish, C., Teanby, N., Vinatier, S., Birch, S, Hörst, S., Coustenis, A., Karkoschka, E., Czaplinksi, E., Hayne, P., Brueshaber, S.R., Maue, T. A.D., Dong, C., Cornet, T., McEwen A., Ramirez, K., Royer, E., Salama, F., Koeppel, A. Fenton, L.K., Goudge, T.A., Cable, M.L., Denk, T., Vu, T.H., Nna-Mvondo, D., Cordier, D., Lebonnois, S., Coates, A., Lefticariu, L., Battalio, J..M., Fagents, S., Tortora, P., Beyer, R.A., Momary, T.W., Gurwell, M.A., Schurmeier, L., Neveu, M., Hanley, J., Limaye, A.B., Daudon, C., Desai, R. T. (2021). New Frontiers Titan Orbiter. Bulletin of the AAS, 53(4). https://doi.org/10.3847/25c2cfeb.4c2df948.

Bernard, J.-M., Quirico, E., Brissaud, O., Montagnac, G., Reynard, B., McMillan, B.P., Coll, P., Nguyen, M.-J., Raulin, F., Schmitt, B. (2006). Reflectance spectra and chemical structure of Titan's tholins: Application to the analysis of Cassini Huygens observations. Icarus, 185, 301-307.

Birch, S. P. D., Hayes, A. G., Howard, A.D., Moore, J.M., Radebaugh, J. (2016). Alluvial Fan Morphology, distribution and formation on Titan. Icarus, 270, 238–247.

Bonnefoy, L.E., Hayes, A.G., Hayne, P.O., Malaska, M.J., Le Gall, A., Solomonidou, A., Lucas, A., 2016. Compositional and spatial variations in titan dune and interdune regions from Cassini VIMS and RADAR. Icarus 270, 222–237.

Boudon, V., Rey, M., Loete, M. (2006). The vibrational levels of methane obtained from analyses of high-resolution spectra. J. Quant. Spectrosc. Radiat. Trans. 98, 394–404.

Brassé, C., Munoz, O., Coll, P., Raulin, F. (2015). Optical constants of Titan aerosols and their tholins analogs: Experimental results and modeling/observational data. Planetary and Space Science, 109-110, 159-174.

916 Bratsolis, E., Bampasidis, G., Solomonidou, A., Coustenis, A., (2012). A despeckle filter for the
917 Cassini synthetic aperture radar images of Titan's surface. Planetary and Space Science, 61,
918 108–113.
919 Brossier, J.F., Rodriguez, S., Cornet, T., Lucas, A., Radebaugh, J., Maltagliati, L., Le Mouélic, S.,
920 Solomonidou, A., Coustenis, A., Hirtzig, M., Jaumann, R., Stephan, K., Sotin, C., (2018).
921 Geological evolution of titan's equatorial regions: possible nature and origin of the dune
922 material. JGR, 123, 1089–1112.
923 Brown, R. H., et al. (2006). The Cassini Visual and Infrared Mapping Spectrometer (VIMS)
924 Investigation. Space Science Reviews, 115(1-4), 111-168.
925 Burr, D.M., Perron, J.T., Lamb, M.P., Iriwin, R.P. III, Collins, G.C., Howard, A.D., Sklar, L.S.,
926 Moore, J.M., Ádámkovics, M., Baker, V.R., Drummond, S.A., Black, B.A., (2013). Fluvial
927 features on Titan: Insights from morphology and modeling. Geological Society of America
928 Bulletin 125, 299-321. doi: 10.1130/B30612.1
929 Campargue, A., Wang, L., Mondelain, D., Kassi, S., Bézard, B., Lellouch, E., Coustenis, A., de
930 Bergh, C., Hirtzig, M., Drossart, P. (2012). An empirical line list for methane in the 1.26-1.71
931 μm region for planetary investigations (T=80-300 K). Application to Titan. Icarus, 219, 110-
932 128.
933 Campargue, A., Lopez, S., Beguier, S., Kassi, S., Mondelain, D., (2015). The absorption spectrum
934 of 13CH4 in the region of the 2ν3 band at 1.66 μm: Empirical line lists and temperature
935 dependence. Journal of Quantitative Spectroscopy and Radiative Transfer, 152, 140-148.
936 Clark, R.N., Curchin, J.M., Barnes, J.W., Jaumann, R., Soderblom, L., Cruikshank, D.P., Brown,
937 R.H., Rodriguez, S., Lunine, J., Stephan, K., Hoefen, T.M., Le Mouelic, S., Sotin, C., Baines,
938 K.H., Buratti, B.J., Nicholson, P.D., (2010). Detection and mapping of hydrocarbon deposits
939 on Titan. Journal of Geophysical Research 115, E10005. doi: 10.1029/2009JE003369.
940 Combe, J-P., McCord, T.B., Hayne, P., Hansen, G.B., (2007). Titan's Surface Composition
941 Investigated by Spectral Mixture Analysis of VIMS/Cassini Data. American Astronomical
942 Society, DPS meeting #39, 44.03, Bulletin of the American Astronomical Society, 39, 500.
943 Corlies, P., McDonald, G.D., Hayes, A.G., Wray, J.J., Ádámkovics, M., Malaska, M.,J., Cable,
944 M.L., Hofgartner, J.D., Hörst, S.M., Liuzzo, L.R., Buffo, J. J., Lorenz, R.D., Turtle, E.P.,
945 (2021). Modeling transmission windows in Titan's lower troposphere: Implications for infrared
946 spectrometers aboard future aerial and surface missions. Icarus 357, 114228. doi:
947 10.1016/j.icarus.2020.114228.
948 Court, R.W., Sephton, M.A., Parnell, J., Gilmour, L., (2006). The alteration of organic matter in
949 response to ionising irradiation: Chemical trends and implications for extraterrestrial sample
950 analysis. Geochimica et Cosmochimica Acta, 70, 4, 1020-1039.
951 Coustenis, A., (1995). Titan's Surface: Composition and Variability from the Near-Infrared
952 Albedo. Icarus, 118, 87-104.
953 Coutelier, M., Cordier, D., Seignovert, B., Rannou, P., Le Gall, A., Cours, T., Maltagliati, L.,
954 Rodriguez, S., (2021). Distribution and intensity of water ice signature in South Xanadu and
955 Tui Regio. Icarus, 364, 114464.
956 Crosta, A., Silber, E., Lopes, R., Johnson, B., Bjonnes, E., Malaska, M., Vance, S., Sotin, C.,
957 Solomonidou, A., Soderblom, J., (2021). Modeling the formation of Menrva impact crater on
958 Titan: Implications for habitability. Icarus 370, 114679.
959 de Kok, R., Irwin, P., Teanby, N., Lellouch, E., Bézard, B., Vinatier, S., Nixon, C., Fletecher, L.,
960 Howett, C., Calcutt, S., Bowles, N., Flasar, F.M., Taylor, F. (2007). Oxygen compounds in
961 Titan's stratosphere observed by Cassini CIRS. Icarus, 186, 354-363.

962 Evans, K.F. (2007). SHDOMPPDA: A Radiative Transfer Model for Cloudy Sky Data
963 Assimilation. J. Atmos. Sci., 64, 3854–3864.
964 Faulk, S., Mitchell, J., Moon, S., Lora, J., (2017). Regional patterns of extreme precipitation on
965 Titan consistent with observed alluvial fan distribution. Nature Geoscience, 10, 827-832.
966 Faulk, S., Lora, J., Mitchell, J., Milly, P.C.D., (2020). Titan's climate patterns and surface methane
967 distribution due to the coupling of land hydrology and atmosphere. Nature Astronomy, 4, 390-
968 398.
969 Fulchignoni, M., Ferri, F., Angrilli, F., Ball, A.J., Bar-Nun, A., Barucci, M.A., Bettanini, C.,
970 Bianchini, G., Borucki, W., Colombatti, G., Coradini, M., Coustenis, A., Debei, S., Falkner, P.,
971 Fanti, G., Flamini, E., Gaborit, V., Grard, R., Hamelin, M., Harri, A.M., Hathi, B., Jernej, I.,
972 Leese, M.R., Lehto, A., Lion Stoppato, P.F., López-Moreno, J.J., Mäkinen, T., McDonnell,
973 J.A.M., McKay, C.P., Molina-Cuberos, G., Neubauer, F.M., Pirronello, V., Rodrigo, R.,
974 Saggin, B., Schwingenschuh, K., Seiff, A., Simões, F., Svedhem, H., Tokano, T., Towner,
975 M.C., Trautner, R., Withers, P., Zarnecki, J.C., 2005. In situ measurements of the physical
976 characteristics of Titan's environment. Nature 438, 785-791. doi: 10.1038/nature04314.
977 Gordon, I.E., et al. (2022). The HITRAN2020 molecular spectroscopic database. Journal of
978 Quantitative Spectroscopy & Radiative Transfer, 277, 107949.
979 Greeley, R., & Batson, R. M. (1990). Planetary mapping. Cambridge University Press.
980 Greeley, R., et al., (2000). Geologic Mapping of Europa. JGR-Planets, 105, E9, 22559-22578.
981 Grundy, W.M., Schmitt, B., (1998). The temperature-dependent near-infrared absorption spectrum
982 of hexagonal H2O ice. Journal of Geophysical Research – Planets, 103, E11.
983 Grundy, W.M., Schmitt, B., Quirico, E., (2002). The Temperature-Dependent Spectrum of
984 Methane Ice I between 0.7 and 5 μm and Opportunities for Near-Infrared Remote Thermometry.
985 Icarus, 155, 486-496.
986 Hedgepeth, J.E., Neish, C.D., Turtle, E.P., Stiles, B., Kirk, R., Lorenz, R.D. (2020). Titan's impact
987 crater population after Cassini. Icarus, Icarus, 344, 113664.
988 doi.org/10.1016/j.icarus.2020.113664.
989 Hirtzig, M., et al. (2013). Titan's surface and atmosphere from Cassini/VIMS data with updated
990 methane opacity. Icarus, 226, 470–486.
991 Jacquinet-Husson, N., Crepeau, L., Armante, R., Boutammine, C., Chedin, A., Scott, N. A., et al.
992 (2011). The 2009 edition of the GEISA spec- troscopic database. Journal of Quantitative
993 Spectroscopy and Radiation Transfer, 112, 2395–2445.
994 Janssen, M.A., Lorenz, R.D., West, R., Paganelli, F., Lopes, R.M., Kirk, R.L., Elachi, C., Wall,
995 S.D., Johnson, W.T.K., Anderson, Y., Boehmer, R.A., Callahan, P., Gim, Y., Hamilton, G.A.,
996 Kelleher, K.D., Roth, L., Stiles, B., Le Gall, A., Cassini RADAR Team, (2009). Titan's Surface
997 at 2.2-cm wavelength imaged by the Cassini RDAR radiometer: Calibration and first results.
998 Icarus 200, 222-239. doi: 10.1016/j.icarus.2008.10.017.
999 Janssen, M. A., Le Gall, A., Lopes, R. M., Lorenz, R. D., Malaska, M. J., Hayes, A. G., et al.
1000 (2016). Titan's surface at 2.18-cm wavelength imaged by the Cassini RADAR radiometer:
1001 Results and interpretations through the first ten years of observation. Icarus, 270, 443–459.
1002 Jaumann, R., Brown, R.H., Stephan, K., Barnes, J.W., Soderblom, L.A., Sotin, C., Le Mouélic, S.,
1003 Clark, R.N., Soderblom, J., Buratti, B.J., Wagner, R., McCord, T.B., Rodriguez, S., Baines,
1004 K.H., Cruikshank, D.P., Nicholson, P.D., Griffith, C.A., Langhans, M., Lorenz, R.D., (2008).
1005 Fluvial erosion and post-erosional processes on Titan. Icarus 197, 526-538. doi:
1006 10.1016/j.icarus.2008.06.002.

Jaumann, R., Kirk, R. L. Lorenz, R. D., Lopes, R. M.C., Stofan, E. Turtle, E. P. Keller, H. U. Wood, C. A., Sotin, C. Soderblom, L. A., Tomasko, M. G., (2009). Geology and Surface Processes on Titan. In: Brown, R. H., Leberton, J.-P., Waite, J. H. (Eds.), Titan from Cassini-Huygens. Springer, New York, pp 75–140.

Karkoschka, E., Tomasko, M.G., (2010). Methane absorption coefficients for the jovian planets from laboratory, Huygens, and HST data. Icarus 205, 674–694.

Karkoschka, E. et al., 2012. The reflectivity spectrum and opposition effect of Titan's surface observed by Huygens' DISR spectrometers. Planet. Space Sci. 60, 342–355.

Krasnopolsky, V.A., 2009. A photochemical model of Titan's atmosphere and ionosphere. Icarus 201, 226-256. doi: 10.1016/j.icarus.2008.12.038.

Lafferty, W., Solodov, A., Weber, A., Olson, B., Hartmann, J-M., (1996). Infrared collision-induced absorption by N2 near 4.3 μm for atmospheric applications: measurements and empirical modeling. Applied Optics 35, 5911-5917.

Langhans, M.H., Jaumann, R., Stephan, K., Brown, R.., Buratti, B.J., Clark, R.N., Baines, K.H., Nicholson, P.D., Lorenz, R.D., Soderblom, L.A., Soderblom, J.M., Sotin, C., Barnes, J.W., Nelson, R., 2012. Titan's fluvial valleys: Morphology, distribution, and spectral properties. Planetary and Space Science 60, 34-51. doi: 10.1016/j.pss.2011.01.020.

Lavvas, P.P., Coustenis, A., Vardavas, I.M., (2008). Coupling photochemistry with haze formation in Titan's atmosphere, Part II: Results and validation with Cassini/Huygens data. Planetary and Space Science 56, 67-99. doi: 10.1016/j.psss.2007.05.027.

Le Gall, M.J. Malaska, R.D. Lorenz, M.A. Janssen, T. Tokano, A.G. Hayes, M. Mastrogiuseppe, J.I. Lu- nine, G. Veyssière, P. Encrenaz, O. Karatekin, (2016). Composition, seasonal change and bathymetry of Ligeia Mare, Titan, derived from its microwave thermal emission. J. Geophys. Res., Planets 121, 233–251.

Lellouch, E., Schmitt, B., Coustenis, A., Cuby, J. G., (2004). Titan's 5-micron lightcurve. Icarus, 168, 1, 209-214.

Le Mouélic, S., (2019). The Cassini VIMS archive of Titan: From browse products to global infrared color maps. Icarus, 319, 121-132.

Lopes, R.M.C., Stofan, E.R., Pecyno, R., Radebaugh, J., Mitchell, K.L., Mitri, G., Wood, C.A., Kirk, R.L., Wall, S.D., Lunine, J.L., Hayes, A., Lorenz, R., Farr, T., Wye, L., Craig, J., Ollerenshaw, R., Janssen, M., LeGall, A., Paganelli, F., West, R., Stiles, B., Callahan, P., Anderson, Y., Valora, P., Soderblom, L., and the Cassini RADAR Team, (2010). Distribution and interplay of geologic processes on Titan from Cassini radar data. Icarus 205, 540–558. doi: 10.1016/j.icarus.2009.08.010.

Lopes, R.M.C., Kirk, R.L.; Mitchell, K.L., Le Gall, A., Barnes, J.W., hayes, A., Kargel, J., Wye, L., Radebaugh, J., Stofan, E.R., Janssen, M., Neish, C., Wall, S., Wood, C.A., Lunine, J.I., Malaska, M.J., 2013. Cryovolcanism on Titan: New results from Cassini RADAR and VIMS. Journal of Geophysical Research: Planets 118, 1-20. doi: 10.1002/jgre.20062.

Lopes, R.M.C., Malaska, M.J., Solomonidou, A., LeGall, A., Janssen, M.A., Neish, C., Turtle, E.P., Birch, S.P.D., Hayes, A.G., Radebaugh, J., Coustenis, A., Schoenfeld, A., Stiles, B.W., Kirk, R.L., Mitchell, K.L., Stofan, E.R., Lawrence, K.J., and the Cassini RADAR Team (2016). Nature, Distribution, and Origin of Titan's Undifferentiated Plains ("Blandlands"). Icarus, 270, 162-182.

Lopes, R.M.C., Wall, S.D., Elachi, C. et al. (2019). Titan as Revealed by the Cassini Radar. Space Science Review, 215, 33.

Lopes, R.M.C., M.J. Malaska, A. M. Schoenfeld, A. Solomonidou, S.P.D. Birch, M. Florence, A.G. Hayes, D.A. Williams, J. Radebaugh, T. Verlander, E.P. Turtle, A. Le Gall, S. Wall, and the Cassini RADAR Team, (2020). A Global Geomorphologic Map of Saturn's Moon Titan. Nature Astronomy, 4, 228-233.

Lora, J. M. and Ádámkovics, M. (2017). The near-surface methane humidity on Titan. Icarus 286, 270–279.

Lorenz, R.D., Wall, S., Radebaugh, J., Boubin, G., Reffet, E., Janssen, M., Stofan, E., Lopes, R., Kirk, R., Elachi, C., Lunine, J., Mitchell, K., Paganelli, F., Soderblom, L., Wood, C., Wye, L., Zebker, H., Anderson, Y., Ostro, S., Allison, M., Boehmer, R., Callahan, P., Encrenaz, P., Ori, G.G., Francescitti, G., Gim, Y., Hamilton, G., Hensley, S., Johnson, W., Kelleher, K., Muhleman, D., Picardi, G., Posa, F., Roth, L., Seu, R., Shaffer, S., Stiles, B., Vetrella, S., Flamini, E., West, R., 2006. The Sand Seas of Titan: Cassini RADAR Observations of Longitudinal Dunes. Science 312, 724-727. doi: 10.1126/science.1123257.

Lorenz, R.D., et al. (2021). Selection and Characteristics of the Dragonfly Landing Site near Selk Crater, Titan. The Planetary Science Journal, 2, 24, 13.

MacKenzie, S., et al.: Planet. Sci J. 2, 112 (2021). https://doi.org/10.3847/PSJ/abf7c9

Malaska, M., Radebaugh, J., Le Gall, A., Mitchell, K., Lopes, R., Wall, S., (2011). High-volume meandering channels in titan's south polar region. 42nd Lunar and Planetary Science Conference, 1562.

Malaska, M. J., Lopes, R. M. C., Williams, D. A., Neish, C. D., Solomonidou, A., Soderblom, J. M., et al. (2016a). Geomorphological map of the Afekan Crater region, Titan: Terrain relationships in the equatorial and midlatitude regions. Icarus, 270, 130–161.

Malaska, M.J., Lopes, R.M., Hayes, A.G., Radebaugh, J., Lorenz, R., Turtle, E., 2016b. Material transport map of Titan: the fate of dunes. Icarus, 270, 183-196.

Malaska, M.J., Hodyss, R., Lunine, J.I., Hayes, A.G., Hofgartner, J.D., Hollyday, G., Lorenz, R.D., (2017). Laboratory measurements of nitrogen dissolution in Titan lake fluids. Icarus, 289, 94-105. doi: 10.1016/j.icarus.2017.01.033

Malaska, M. J., Radebaugh, J., Lopes, R. M. C., Mitchell, K., Verlander, T., Schoenfeld, A., Florence, M., Le Gall, A., Solomonidou, A., Hayes, A., Birch, S., Janssen, M., Schurmeier, L., Cornet, T., Ahrens, C., and the Cassini RADAR team, (2020). Labyrinth Terrain on Titan. Icarus, 344, 113764.

McCord, T.B., et al., (2004). Cassini VIMS observations of the Galilean satellites including the VIMS calibration procedure. Icarus, 172, 104-126.

McKellar, A. R. (1989). Low-temperature infrared absorption of gaseous N 2 and N2 + H2 in the 2.0-2.5 μm region: Application to the atmospheres of Titan and Triton. Icarus, 80, 361-369.

Miller, J.W., Birch, S.P.D., Hayes, A.G., Malaska, M.J., Lopes, R.M.C., Schoenfeld, A.M., Corlies, P.M., Burr, D.M., Farr, T.G., Perron, J.T., (2021).Fluvial Features on Titan and Earth: Lessons from Planform Images in Low-resolution SAR. The Planetary Science Journal, 2:142.

Mitchell, J.L., (2008). The drying of Titan's dunes: Titan's methane hydrology and its impact on atmospheric circulation. J. Geophys. Res. E Planets, 113, 1-22.

Mitri, G., Showman, A.P., Lunine, J.I. and Lopes, R.M., 2008. Resurfacing of Titan by ammonia-water cryomagma. Icarus, 196, 216-224.

Mitri, G., Bland, M.T., Showman, A.P., Radebaugh, J., Stiles, B., Lopes, R.M.C., Lunine, J.I., pappalardo, R.T., 2010. Mountains on Titan: Modeling and observations. Journal of Geophysical Research: Planets 115, E10002.

Moore, J.M., Howard, A.D., Morgan, A.M., 2014. The landscape of titan as witness to is climate evolution. Journal of Geophysical Research: Planets 119, 2060-2077. doi: 10.1002/2014JE004608.

Moroz, L.V., Arnold. G., Korochantsev, A.V., Wasch, R., (1998). Natural Solid Bitumens as Possible Analogs for Cometary and Asteroid Organics:. 1. Reflectance Spectroscopy of Pure Bitumens. Icarus, 134, 2, 253-268.

Nelson, R.M., Kamp. L.W., Lopes, R.M.C., Matson, D.L., Kirk, R.L., Hapke, B.W., Wall, S.D., Boryta, M.D., Leader, F.E., Smythe, W.D., Mitchell, K.L., Baines, K.H., Jaumann, R., Sotin, C., Clark, R.N., Cruikshank, D.P., Drossart, P., Lunine, J.I., Combes, M., Bellucci, G., Bibring, J-P., Capaccioni, F., Cerroni, P., Coradini, A., Formisano, V., Filacchione, G., Langevin, Y., McCord, T.B., Mennella, V., Nicholson, P.D., Sicardy, B., Irwin, P.G.J. (2009). Photometric Changes on Saturn's Moon Titan: Evidence for Cryovolcanism. Geophys. Res. Lett., 36, L04202, doi:10.1029/2008GL036206.

Neish, C.D., Barnes, J.W., Sotin, C., MacKenzie, S., Soderblom, J.M., Le Mouélic, S., Kirk, R.L., Stiles, B.W., Malaska, M.J., Le Gall, A., Brown, R.H., Baines, K.H., Buratti, B., Clark, R.N., Nicholson, P.D., (2015). Spectral properties of Titan's impact craters imply chemical weathering of its surface. Geophys. Res. Lett. 42, 3746–3754.

Niemann, H.B., Atreya, S.K., Demick, J., Gautier, D., Haverman, J., Harpold, D., Kasprzak, W., Lunine, J., Owen, T., Raulin, F. (2010). Composition of Titan's lower atmosphere and simple surface volatiles as measured by the Cassini-Huygens probe gas chromatograph mass spectrometer experiment. J. Geophys. Res., 115, E12006.

Nixon, R. Clark, R. Courtin, A. Hayes, R. Lopes, R. Yelle, C. Sotin, A. Rymer, R. Johnson, R. Lorenz, M. Mastrogiuseppe, H. Smith, D. Strobel, R. Achterberg, A. Buch, K. Mandt, D. Mitchell, F. Raulin, E. Turtle, L. Iess, V. Vuitton, A. Solomonidou, R. West, P. Coll, (2018). Titan's cold case files—outstanding questions after Cassini-Huygens. Planet. Space Sci. 155, 50–72.

Quirico, E., Schmitt, B., (1997). Near-Infrared Spectroscopy of Simple Hydrocarbons and Carbon Oxides Diluted in Solid N2 and as Pure Ices: Implications for Triton and Pluto. Icarus, 127, 354-378.

Patterson, G.W. et al., (2010). Global geological mapping of Ganymede. Icarus 207, 845–867. http://dx.doi.org/10.1016/j.icarus.2009.11.035.

Peck, E. R., and Khanna, B. N. (1966) JOSA, 56, 1059.

Poggiali, V., Mastrogiuseppe, M., Hayes, A., Seu, R., Birch, S., Lorenz, R., Grima, C., Hofgartner, J., (2016). Liquid-filled canyons on Titan. Geophysical Research Letter, 43, 7887-7894.

Radebaugh, J., Lorenz, R.D., Kirk, R.L., Lunine, J.I., Stofan, E.R., Lopes, R.M.C., Wall, S.D., 2007. Mountains on Titan as observed by Cassini Radar. Icarus 192, 77-91. doi: 10.1016/j.icarus.2007.026.020.

Radebaugh, J., Lorenz, R.D., Lunine, J.I., Wall, S.D., Boubin, G., Reffet, E., Kirk, R.L., Lopes, R.M., Stofan, E.R., Soderblom, L., Allison, M., Janssen, M., Paillouo, P., Callahan, P., Spencer, C., Cassini RADAR Team, 2008. Dunes on Titan observed by Cassini Radar. Icarus 194, 690-703. doi: 10.1016/j.icarus.2007.10.015.

Radebaugh, J., Ventra, D., Lorenz, R.D., Farr, T.G., Kirk, R.L., Hayes, A., Malaska, M.J., Birch, S., Liu, Z.Y.C., Lunine, J.I., Barnes, J., Le Gall, A., Lopes, R., Stofan, E., Wall, S., Pailloy, P. (2016). Alluvial and fluvial fans on Saturn's moon Titan reveal processes, materials and regional geology. Ventra, D. & Clarke, L. E. (eds) Geology and Geomorphology of Alluvial

and Fluvial Fans: Terrestrial and Planetary Perspectives. Geological Society, London, Special Publications, 440.
Rannou, P., Montmessin, F., Hourdin, F., Lebonnois, S., (2006). The latitudinal distribution of clouds on Titan. Science, 311, 201-205.
Rey, M., Nikitin, V., Bezard, B., Rannou, P., Coustenis, A., & Tyuterev, V. (2018). New accurate theoretical line lists of 12CH4 and 13CH4 in the 0–13400 cm 1 range: Application to the modeling of methane absorption in Titan's atmosphere. Icarus, 303, 114–130.
Rodriguez, S., et al. (2014). Global mapping and characterization of Titan's dune fields with Cassini: Correlation between RADAR and VIMS observations. Icarus 230, 168–179.
Rodriguez, S., et al. (2022). Science goals and new mission concepts for future exploration of Titan's atmosphere, geology and habitability: titan POlar scout/orbitEr and in situ lake lander and DrONe explorer (POSEIDON). Experimental Astronomy, https://doi.org/10.1007/s10686-021-09815-8.
Rothman, L. S., Gordon, I. E., Babikov, Y., Barbe, A., Chris Benner, D., Bernath, P. F., et al. (2013). The HITRAN2012 molecular spectroscopic database. Journal of Quantitative Spectroscopy and Radiation Transfer, 112, 2395–2445.
Schoenfeld, A., Lopes, R., Malaska, M., Solomonidou, A., Williams, D., Birch, S., Hayes, A., Corlies, P., Le Gall, A., Janssen, M., Le Mouelic, S., Turtle, E., Florence, M., Verlander, T., (2021). Geomorphological map of the South Belet Region of Titan. Icarus, 366, 114516.
Schoenfeld, A., Solomonidou, A., Malaska, M., Lopes, R., Birch, S., Mouelic, S., Florence, M., Verlander, T., Wall, S., Elachi, C. (2023). Geomorphological map of the Soi crater region on Titan. Journal of Geophysical Research: Planets, 128, e2022JE007499. https://doi.org/10.1029/2022JE007499.
Schurmeier, L.R., Dombard, A., (2018). Crater relaxation on Titan aided by low thermal conductivity sand infill. Icarus, 305, 314-323.
Seignovert, B., Le Mouelic, S., Brown, R.H., Karkoschka, E., Pasek, V., Sotin, C., Turtle, E.P. (2019). Titan's Global Map Combining Vims and Iss Mosaics. EPSC - European Planetary Science Congress 2019, Geneva, Switzerland, September 15-20, 2019, JPL Open Repository.
Smith, P. H., et al. (2005). Results from the Descent Imager/Spectral Radiometer (DISR) experiment on the Huygens entry probe of Titan. Nature, 438(7069), 779-784.
Soderblom, L.A. et al., (2007). Correlations between Cassini VIMS spectra and RADAR SAR images: Implications for Titan's surface composition and the character of the Huygens Probe Landing Site. Planet. Space Sci. 55, 2025–2036.
Sohl, F. et al., (2014). Tidal stresses on Titan and implications for its geology and habitability. J. Geophys. Res. 119, 1013–1036.
Solomonidou, A., G. Bampasidis, M. Hirtzig, A. Coustenis, K. Kyriakopoulos, K. Seymour, E. Brastolis, and X. Moussas (2013), Morphotectonic features on Titan and their possible origin, Planet. Space Sci., 77, 104–117.
Solomonidou, A., Hirtzig, M., Coustenis, A., Bratsolis, E., Le Mouélic, S., Rodriguez, S., et al. (2014). Surface albedo spectral properties of geologically interesting areas on Titan. Journal of Geophysical Research: Planets, 119, 1729–1747.
Solomonidou, A., Coustenis, A., Hirtzig, M., Rodriguez, S., Stephan, K., Lopes, R. M. C., et al. (2016). Temporal variations of Titan's surface with Cassini/VIMS. Icarus, 270, 85–99.
Solomonidou, A., A. Coustenis, R. Lopes, M. Malaska, S. Rodriguez, P. Drossart, C. Elachi, B. Schmitt, M. Janssen, M. Hirtzig, S. Wall, C. Sotin, K. Lawrence, N. Altobelli, N. Bratsolis, J. Radebaugh, K. Stephan, R. Brown, S. Le Mouélic, A. Le Gall, E.V. Villanueva, J.F. Brossier,

A.A. Bloom, O. Witasse, C. Matsoukas and A., Schoenfeld (2018). The Spectral Nature of Titan's Major Geomorphological Units: Constraints on Surface Composition. J. Geophys. Res, 123, 2, 489-507.

Solomonidou, A., Neish, C., Coustenis, A., Malaska, M., Le Gall, A., Lopes, R., Werynski, A., Markonis, Y., Lawrence, K., Altobelli, N., Witasse, O., Schoenfeld, A., Matsoukas, C., Baziotis, I., Drossart, P., (2020a). The chemical composition of impact craters on Titan I. Implications for exogenic processing. Astronomy & Astrophysics, 641, A16.

Solomonidou, A., Le Gall, A., Malaska, M., Birch, S., Lopes, R., Coustenis, A., Rodriguez, S., et al. (2020b). Spectral and emissivity analysis of the raised ramparts around Titan's northern lakes. Icarus, 344, 113338.

Solomonidou, A., Coustenis, A., Lopes, R., Malaska, M., Le Gall, A., Schmitt, B., Schoenfeld, A., Wall, S., Lawrence, K., Sotin, C., Matsoukas, C., Markonis, I., Drossart, P., Elachi, C., (2022). Chemical composition analysis of Titan's equatorial and midlatitude surface regions. Europlanet Science Congress 2022.

Stofan, E.R., Elachi, C., Lunine, J.I., Lorenz, R.D., Stiles, B., Mitchell, K.L., Ostro, S., Soderblom, L., Wood, C., Zebker, H., Wall, S., Janssen, M., Kirk, R., Lopes, R., Paganelli, F., Radebaugh, J., Wye, L., Anderson, Y., Allison, M., Boehmer, R., Callahan, P., Encrenaz, P., Flamini, E., Francescetti, G., Gim, Y., Hamilton, G., Hensley, S., Johnson, W.T.K., Kelleher, K., Muhlman, D., Paillou, P., Picardi, G., Posa, F., Roth, Seu, R., Shaffer, S., Vetrella, S., West, R., 2007. The lakes of Titan. Nature 445, 61-64. doi: 10.1038/nature05438.

Sulaiman, A., et al. (2021). Enceladus and Titan: emerging wolds of the Solar System. Experimental Astronomy, https://doi.org/10.1007/s10686-021-09810-z.

Tobie, G., et al. (2014). Science goals and mission concept for the future exploration of Titan and Enceladus. Planetary and Space Science. 104, 59–77.

Tokano, T., (2005). Meteorological assessment of the surface temperatures on Titan: constraints on the surface type. Icarus, 173, 222-242.

Tomasko, M. G., Doose, L., Engel, S., Dafoe, L. E., West, R., Lemmon, M., et al. (2008). A model of Titan's aerosols based on measurements made inside the atmosphere. Planetary and Space Science, 56, 669–707.

Wall, S.D., Lopes, R.M., Stofan, E.R., Wood, C.A., Radebaugh, J.L., Hörst, S.M., Stiles, B.W., Nelson, R.M., Kamp, L.W., Janssen, M.A. and Lorenz, R.D., 2009. Cassini RADAR images at Hotei Arcus and western Xanadu, Titan: Evidence for geologically recent cryovolcanic activity. Geophysical Research Letters, 36.

Weber, M.J., (2003). Handbook of Optical Materials. CRC Press, Boca Raton, Florida.

Werynski, A., Neish, C.D., Le Gall, A., Janssen, M.A., The Cassini RADAR Team, (2019). Compositional variations of Titan's impact craters indicates active surface erosion. Icarus, 321, 508-521.

Williams, D.A., Radebaugh, J., Lopes, R.M.C., Stofan, E., 2011. Geomorphologic mapping of the Menrva region of Titan using *Cassini* RADAR data. Icarus 212, 744-750. doi: 10.1016/j.icarus.2011.01.014.

Williams, D.A., Yingst, R.A., Garry, W.B., 2014. Introduction: The geologic mapping of Vesta. Icarus 244, 1–12. http://dx.doi.org/10.1016/j.icarus.2014.03.001.

Wilson, E.H., Atreya, S.K., 2004. Current state of modeling the photochemistry of Titan's mutually dependent atmosphere and ionosphere. Journal of Geophysical Research 109, E06002. doi: 10.1029/2003JE002181.

Wood, C.A., Lorenz, R., Kirk, R., Lopes, R., Mitchell, K., Stofan, E., and the Cassini RADAR Team, (2010). Impact craters on Titan. Icarus, 206 (2010) 334-344.
Wood, C.A. and Radebaugh, J., 2020. Morphologic evidence for volcanic craters near Titan's north polar region. Journal of Geophysical Research: Planets, 125(8), p.e2019JE006036.

Appendix

Table 3. Compositional constraints of the various units (261 locations) within the Soi crater region. The various locations are shown in Figure 4. The mixtures are given by percentages of different constituents (H_2O, CH_4, tholins, and dark organic material). HC_3N, CO_2, NH_3 ices were not detected in these locations. Spectra in full resolution for all presented constituents can be found in Figure 3.

Items	Location	Unit	Dark	H_2O ice	Tholins %	CH_4 %
1.	8	***pul***	40	10	45	5
2.	8b	*pul*	60	-	40	-
3.	14	*pul*	60	-	45	-
4.	24b	*pul*	20	30	40	10
5.	29	*pul*	-	40	40	20
6.	41	*pul*	-	50	25	25
7.	44	*pul*	50	30	10	10
8.	52	*pul*	-	20	80	-
9.	53b	*pul*	-	25	60	15
10.	55b	*pul*	35	15	30	20
11.	56	*pul*	-	25	60	15
12.	58b	*pul*	-	45	35	10
13.	63	*pul*	-	50	40	10
14.	73c	*pul*	20	25	40	15
15.	79	*pul*	-	25	60	15
16.	80b	*pul*	-	40	60	-
17.	98b	*pul*	-	45	35	20
18.	101	*pul*	-	45	50	5
19.	101b	*pul*	-	45	50	5
20.	102b	*pul*	-	50	45	5
21.	105	*pul*	-	40	55	5
22.	106	*pul*	-	30	65	5
23.	108c	*pul*	-	30	50	20
24.	A3	*pul*	50	25	15	10
25.	A4	*pul*	65	20	10	5
26.	A6	*pul*	60	35	-	5
27.	A13	*pul*	60	30	-	10
28.	A13c	*pul*	60	30	-	10
29.	A18b	*pul*	-	35	50	15
30.	A20	*pul*	-	50	30	20
31.	A22	*pul*	-	30	50	20
32.	6b	***pfv***	60	15	25	-
33.	8c	*pfv*	50	-	45	5
34.	9c	*pfv*	40	-	55	5
35.	10	*pfv*	35	10	50	5
36.	10c	*pfv*	60	-	40	-
37.	11b	*pfv*	60	25	15	-
38.	12	*pfv*	60	-	40	-
39.	21	*pfv*	-	25	65	10
40.	22b	*pfv*	35	-	50	10
41.	23	*pfv*	70	20	-	10
42.	27b	*pfv*	40	-	60	-
43.	34	*pfv*	45	30	10	15
44.	35	*pfv*	5	25	55	15
45.	35b	*pfv*	5	25	55	15
46.	44b	*pfv*	15	40	30	15
47.	53c	*pfv*	15	30	40	15
48.	56b	*pfv*	-	45	40	15
49.	58c	*pfv*	-	45	35	10
50.	60	*pfv*	-	55	45	-
51.	60b	*pfv*	-	55	45	-
52.	67	*pfv*	75	-	25	-
53.	70	*pfv*	60	25	10	5
54.	73	*pfv*	-	50	50	-
55.	75	*pfv*	-	40	60	-
56.	75b	*pfv*	-	40	60	-

57.	77b	*pfv*	50	30	20	-
58.	79b	*pfv*	-	25	60	15
59.	97	*pfv*	50	30	-	20
60.	104	*pfv*	-	60	35	5
61.	107	*pfv*	-	40	50	10
62.	108	*pfv*	-	40	40	20
63.	109b	*pfv*	-	40	40	20
64.	110	*pfv*	-	35	60	5
65.	A2b	*pfv*	60	35	-	5
66.	A13b	*pfv*	-	30	60	10
67.	A18	*pfv*	35	-	50	15
68.	A19b	*pfv*	-	55	45	-
69.	A36	*pfv*	-	25	70	5
70.	A41	*pfv*	-	30	65	5
71.	A53	*pfv*	-	30	65	5
72.	43	***psv***	45	30	10	15
73.	43b	*psv*	45	30	10	15
74.	47	*psv*	40	25	15	20
75.	81	*psv*	35	25	20	20
76.	87	*psv*	40	20	20	20
77.	87b	*psv*	40	25	20	15
78.	50	***pil***	-	25	55	20
79.	82	*pil*	45	30	15	10
80.	84b	*pil*	20	25	35	20
81.	94	*pil*	30	25	25	20
82.	94b	*pil*	25	25	30	20
83.	95	*pil*	55	25	-	20
84.	96	*pil*	50	30	5	15
85.	97b	*pil*	50	30	5	15
86.	98	*pil*	-	45	35	20
87.	98c	*pil*	-	45	35	20
88.	55	***psh***	35	15	30	20
89.	61	*psh*	-	50	50	-
90.	80	*psh*	-	40	60	-
91.	100	*psh*	-	35	55	10
92.	77	***pgh***	55	20	25	-
93.	78	*pgh*	55	20	25	-
94.	A10b	*pgh*	55	20	25	-
95.	4	***pu***	40	5	50	5
96.	5	*pu*	30	10	55	5
97.	7	*pu*	45	5	45	5
98.	30b	*pu*	5	30	40	25
99.	31b	*pu*	5	30	40	25
100.	33	*pu*	10	25	40	25
101.	36	*pu*	-	30	45	25
102.	36b	*pu*	-	30	45	25
103.	39b	*pu*	25	65	-	10
104.	40	*pu*	-	40	45	15
105.	40b	*pu*	-	40	45	15
106.	41c	*pu*	-	45	30	25
107.	42	*pu*	35	35	-	30
108.	45	*pu*	10	40	30	20
109.	45b	*pu*	-	20	60	20
110.	46	*pu*	30	25	30	15
111.	46b	*pu*	40	15	30	15
112.	48	*pu*	-	20	60	20
113.	57	*pu*	-	35	60	5

114.	59	*pu*	-	45	40	15
115.	62	*pu*	-	35	40	25
116.	64	*pu*	-	35	40	25
117.	65	*pu*	-	50	35	15
118.	72	*pu*	-	35	55	10
119.	74	*pu*	-	40	55	5
120.	76	*pu*	-	40	35	25
121.	89	*pu*	-	40	55	5
122.	90	*pu*	-	50	50	-
123.	90b	*pu*	-	40	55	5
124.	91	*pu*	-	25	60	15
125.	93	*pu*	-	35	60	5
126.	99b	*pu*	-	60	30	10
127.	106b	*pu*	-	30	65	5
128.	111	*pu*	-	35	60	5
129.	A10	*pu*	40	-	50	10
130.	30	***pdu***	25	40	25	10
131.	31	*pdu*	25	35	30	10
132.	32	*pdu*	15	35	35	15
133.	32b	*pdu*	15	40	30	15
134.	33b	*pdu*	15	40	30	15
135.	37	*pdu*	15	40	40	5
136.	37b	*pdu*	10	45	40	5
137.	38	*pdu*	25	40	20	15
138.	38b	*pdu*	25	40	20	15
139.	39	*pdu*	-	65	25	10
140.	42b	*pdu*	40	25	20	15
141.	48b	*pdu*	40	25	20	15
142.	49	*pdu*	35	25	25	15
143.	49b	*pdu*	30	25	30	15
144.	104b	*pdu*	-	60	35	5
145.	A15	*pdu*	-	50	40	10
146.	A15b	*pdu*	-	50	40	10
147.	A19c	*pdu*	-	55	45	-
148.	9b	***ds***	60	25	-	15
149.	19c	*ds*	60	25	-	15
150.	21b	*ds*	10	20	60	10
151.	22	*ds*	10	20	55	15
152.	24	*ds*	50	30	-	20
153.	25	*ds*	60	25	-	15
154.	27	*ds*	65	35	-	-
155.	51	*ds*	60	-	30	10
156.	54	*ds*	70	-	30	-
157.	A5	*ds*	10	30	60	-
158.	A19	*ds*	-	45	55	-
159.	A31	*ds*	-	25	60	15
160.	A39	*ds*	-	25	65	10
161.	A40	*ds*	10	25	60	5
162.	A47	*ds*	-	35	60	5
163.	A48	*ds*	-	35	65	-
164.	A49	*ds*	-	35	65	-
165.	6	***dl***	65	5	30	-
166.	9	*dl*	75	5	20	-
167.	10b	*dl*	80	-	20	-
168.	11	*dl*	85	5	10	-
169.	13	*dl*	75	-	25	-
170.	15	*dl*	75	-	25	-

171.	23b	*dl*	65	-	35	-
172.	28	*dl*	45	30	15	10
173.	66	*dl*	75	-	25	-
174.	A1	*dl*	85	-	10	5
175.	A2	*dl*	80	15	-	5
176.	A9	*dl*	70	-	25	5
177.	A12	*dl*	60	15	20	5
178.	A21b	*dl*	35	20	25	20
179.	A27	*dl*	40	25	25	10
180.	A28	*dl*	40	20	35	5
181.	A34	*dl*	-	35	60	5
182.	A44	*dl*	-	30	65	5
183.	A46	*dl*	-	30	65	5
184.	A52	*dl*	-	35	65	-
185.	1	***du***	70	5	20	5
186.	23e	*du*	65	-	30	5
187.	26	*du*	60	-	35	5
188.	57b	*du*	60	-	30	10
189.	A7	*du*	70	10	20	-
190.	A13d	*du*	70	15	25	-
191.	9d	***hm***	50	30	20	-
192.	19b	*hm*	40	-	45	15
193.	41b	*hm*	-	50	25	25
194.	58	*hm*	-	35	45	10
195.	77c	*hm*	50	30	20	-
196.	103b	*hm*	-	45	50	5
197.	15c	***hh***	45	-	55	-
198.	16	*hh*	-	40	60	-
199.	17	*hh*	-	25	60	15
200.	17b	*hh*	-	25	60	15
201.	17c	*hh*	-	20	65	15
202.	23d	*hh*	40	-	60	-
203.	53	*hh*	60	-	40	-
204.	68	*hh*	55	20	20	5
205.	71	*hh*	70	30	-	-
206.	73b	*hh*	40	20	25	15
207.	83	*hh*	40	25	20	15
208.	102	*hh*	-	45	50	5
209.	103	*hh*	-	50	45	5
210.	109	*hh*	-	50	20	30
211.	A11	*hh*	20	20	55	5
212.	A14	*hh*	15	40	45	-
213.	A32	*hh*	-	25	65	10
214.	A33	*hh*	-	25	60	15
215.	A20b	*hh*	-	45	35	20
216.	A21	*hh*	25	25	35	15
217.	A24	*hh*	-	25	65	10
218.	A25	*hh*	-	25	60	15
219.	A37	*hh*	-	30	65	5
220.	A38	*hh*	-	30	65	5
221.	A50	*hh*	-	40	60	
222.	A51	*hh*	-	30	60	10
223.	A54	*hh*	-	30	65	5
224.	A55	*hh*	-	35	60	5
225.	2	***hu***	10	25	60	5
226.	3	*hu*	50	15	35	-
227.	18	*hu*	40	-	45	15

228.	18b	*hu*	40	-	45	15
229.	19	*hu*	-	25	65	10
230.	20	*hu*	40	-	45	15
231.	64b	*hu*	-	65	35	-
232.	92	*hu*	-	65	35	-
233.	99	*hu*	-	65	20	15
234.	99c	*hu*	-	65	20	15
235.	108b	*hu*	-	40	40	20
236.	A8	*hu*	55	-	45	-
237.	A16	*hu*	-	40	60	-
238.	A17	*hu*	-	35	65	-
239.	15b	***hph***	45	-	55	-
240.	A23	*hph*	-	25	60	15
241.	A26	*hph*	-	30	65	5
242.	A29	*hph*	-	25	65	10
243.	A30	*hph*	-	30	65	5
244.	A35	*hph*	-	30	65	5
245.	A42	*hph*	-	35	60	5
246.	A43	*hph*	-	35	60	5
247.	A45	*hph*	-	35	65	-
248.	*114*	***lbf***	20	25	40	15
249.	*114b*	*lbf*	20	25	40	15
250.	23c	***ceh***	70	-	30	-
251.	52b	*ceh*		20	80	-
252.	69	*ceh*	70	-	30	-
253.	52c	***crh***		20	80	-
254.	112	*crh*	-	20	80	-
255.	88	***cf3***	70	15	15	-
256.	84	***bse***	45	35	-	20
257.	85	*bse*	35	30	20	15
258.	86	*bse*	35	30	20	15
259.	*113*	*bse*	25	20	35	20
260.	*115*	***brh***	20	25	40	15
261.	*116*	*brh*	40	25	20	15

1244